Calhoun: The NPS Institutional Archive

DSpace Repository

Theses and Dissertations | 1. Thesis and Dissertation Collection, all items

1990-06

Interferometric SAR imaging of ocean surface currents and wavefields

Marom, Moshe

Monterey, California. Naval Postgraduate School

https://hdl.handle.net/10945/35036

This publication is a work of the U.S. Government as defined in Title 17, United States Code, Section 101. Copyright protection is not available for this work in the United States.

Downloaded from NPS Archive: Calhoun

Calhoun is the Naval Postgraduate School's public access digital repository for research materials and institutional publications created by the NPS community. Calhoun is named for Professor of Mathematics Guy K. Calhoun, NPS's first appointed -- and published -- scholarly author.

Dudley Knox Library / Naval Postgraduate School
411 Dyer Road / 1 University Circle
Monterey, California USA 93943

http://www.nps.edu/library

NAVAL POSTGRADUATE SCHOOL

Monterey, California

AD-A239 312

DISSERTATION

INTERFEROMETRIC SYNTHETIC
APERTURE RADAR IMAGING OF OCEAN
SURFACE CURRENTS AND WAVEFIELDS

by

Moshe Marom

June, 1990

Dissertation Supervisor: E. B. Thornton

Approved for public release; distribution is unlimited.

DTIC
ELECTE
AUG 0 8 1991
S B D

91-07161

91 8 07 031

Unclassified

Security Classification of this page

REPORT DOCUMENTATION PAGE

1a Report Security Classification UNCLASSIFIED	1b Restrictive Markings
2a Security Classification Authority	3 Distribution Availability of Report
2b Declassification/Downgrading Schedule	Approved for public release; distribution is unlimited
4 Performing Organization Report Number(s)	5 Monitoring Organization Report Number(s)
6a Name of Performing Organization: Naval Postgraduate School; 6b Office Symbol (*If Applicable*) 68	7a Name of Monitoring Organization: Naval Postgraduate School
6c Address (*city, state, and ZIP code*): Monterey, CA 93943-5000	7b Address (*city, state, and ZIP code*): Monterey, CA 93943-5000
8a Name of Funding/Sponsoring Organization; 8b Office Symbol (*If Applicable*)	9 Procurement Instrument Identification Number
8c Address (*city, state, and ZIP code*)	10 Source of Funding Numbers

Program Element Number	Project No	Task No	Work Unit Accession No

11 Title (*Include Security Classification*) Interferometric Synthetic Aperture Radar in Imaging of Ocean Surface Currents and Wavefields

12 Personal Author(s) Moshe Marom

13a Type of Report	13b Time Covered	14 Date of Report (*year, month,day*)	15 Page Count
Dissertation	From To	1990, June	219

16 Supplementary Notation The views expressed in this paper are those of the author and do not reflect the official policy or position of the Department of Defense or the U.S. Government.

17 Cosati Codes			18 Subject Terms (*continue on reverse if necessary and identify by block number*)
Field	Group	Subgroup	Interferometric SAR, Scene coherence time, 2D wavenumber spectra, Surface Currents

19 Abstract (*continue on reverse if necessary and identify by block number*

The potential of a relatively new method to remotely measure near-surface ocean currents and dominant wave spectra using Interferometric Synthetic Aperture Radar (INSAR) is demonstrated. INSAR consists of a single conventional SAR augmented by an additional receiving antenna. The phase difference between the corresponding SAR image scenes observed by the antennas provides an interferogram that is directly proportional to the ocean surface velocity field. This direct motion detection by INSAR suggests a significant advance compared with conventional SAR where the response to the moving ocean surface is indirectly related to the complex modulation of the surface reflectivity by longer waves and currents.

An experiment using an airborne implementation of INSAR to measure ocean surface currents and wave fields, compared with simultaneous ground truth measurements using Lagrangian drifters and wave array data was conducted in Monterey Bay. Mean current magnitudes measured by INSAR agree to within 10 percent compared with conventional measurements. The INSAR image wavenumber spectrum is consistent with the *in situ* directional spectrum and with predicted numerical refraction model outputs. The wavelength of the dominant observed swells are in better agreement (correlation better than 0.9) than wave direction.

An attempt to estimate the scene coherence time for L-band SAR was made by taking advantage of the almost simultaneously acquired SAR and INSAR images. The obtained mean scene coherence time O (100 msec) is consistent with sparse observed estimates in the literature. This limited radar temporal coherence, caused by the velocity spread of short waves, degrades the azimuthal resolution of SAR and INSAR and depends on the sea state and radar wavelength. The experimental results show that the finite scene coherence time has a dominant role on the distortion of INSAR (and SAR) image spectrum relative to the ocean wave spectrum. The present study introduces limitations of interferometric SAR configuration in imaging nonstationary scenes like the ocean surface.

20 Distribution/Availability of Abstract: [X] unclassified/unlimited [ ] same as report [ ] DTIC users	21 Abstract Security Classification: Unclassified	
22a Name of Responsible Individual: E. B. Thornton	22b Telephone (*Include Area code*): (408) 646-3440	22c Office Symbol: 68Tm

DD FORM 1473, 84 MAR 83 APR edition may be used until exhausted All other editions are obsolete

security classification of this page Unclassified

Approved for public release; distribution is unlimited

Interferometric SAR Imaging of Ocean Surface Currents and Wavefields

by

Moshe Marom
Commander, Israeli Navy
B. S., Israel Technological Institute, Haifa, 1979
M.S., Naval Postgraduate School, 1988

Submitted in partial fulfillment of the
requirements for the degree of

DOCTOR OF PHILOSOPHY
IN PHYSICAL OCEANOGRAPHY

from the

NAVAL POSTGRADUATE SCHOOL

June, 1990

Author: [redacted]

Moshe Marom

Approved by: [redacted]

[redacted]

G. R. Valenzuela
Naval Research Laboratory
Washington, D.C.

Pecheng Chu
Adjunct Professor of Oceanography

[redacted]

Kenneth L. Davidson
Professor of Meteorology

[redacted]

Jeffrey A. Nystuen
Assistant Professor of Oceanography

[redacted]

Hung-Mou Lee
Associate Professor of Electrical
and Computer Engineering

[redacted]

Edward B. Thornton
Professor of Oceanography
(Dissertation Supervisor

[redacted]

Curtis A. Collins
Chairman, Department of Oceanography

[redacted]

Provost/Academic Dean

ABSTRACT

The potential of a relatively new method to remotely measure near-surface currents and dominant wave spectra using Interferometric Synthetic Aperture Radar (INSAR) is demonstrated. INSAR consists of a single conventional SAR augmented by an additional receiving antenna. The phase difference between the corresponding SAR image scenes observed by the antennas provides an interferogram that is directly proportional to the ocean surface velocity field. This direct motion detection by INSAR suggests a significant advance compared with conventional SAR where the response to the moving ocean surface is indirectly related to the complex modulation of the surface reflectivity by longer waves and currents.

An experiment using an airborne implementation of INSAR to measure ocean surface currents and wave fields, compared with simultaneous ground truth measurements using Lagrangian drifters and wave array data was conducted in Monterey Bay. INSAR measured mean current magnitude estimates agree to within 10 percent compared with conventional measurements. The INSAR image wavenumber spectrum is consistent with the *in situ* directional spectrum and with predicted numerical refraction model outputs. The wavelength of the observed swells are in better agreement (correlation better than 0.9) than wave direction.

An attempt to estimate the scene coherence time for L-band SAR was made by taking advantage of the almost simultaneously acquired SAR and INSAR images. The obtained mean scene coherence time O (100 msec) is consistent with sparse observed estimates in the literature. This limited radar temporal coherence, caused by the velocity spread of short waves, degrades the azimuthal resolution of SAR and INSAR and depends on the sea state and radar wavelength. The experimental results show that the finite scene coherence time has a dominant role on the distortion of the INSAR (and SAR) image spectrum relative to the ocean wave spectrum. The present study introduces limitations of interferometric SAR configuration in imaging nonstationary scenes like the ocean surface.

DTIC COPY INSPECTED 6

Accession For
NTIS GRA&I ☑
DTIC TAB ☐
Unannounced ☐
Justification
By
Distribution/
Availability Codes
Dist | Avail and/or Special
A-1

TABLE OF CONTENTS

I. INTRODUCTION 1

A. INTERFEROMETRIC RADAR REMOTE SENSING OF OCEAN SURFACE VELOCITY FIELDS 1

B. STATEMENT OF OBJECTIVES AND PROBLEMS 2

C. SUMMARY 3

II. LITERATURE REVIEW 5

A. INTRODUCTION 5

B. ELECTROMAGNETIC FIELD SCATTERED FROM THE OCEAN SURFACE 6

1. Specular Point/Physical Optics Model 8

2. The Bragg-Rice/Perturbation Model 10

3. Composite/Two-Scale Surface Model 14

4. Application of Composite Model to SAR 15

III. PRINCIPAL MECHANISMS OF SAR AND INSAR IMAGERY RELEVANT TO THE OCEAN SURFACE 17

A. INTRODUCTION 17

B. FUNDAMENTAL PARAMETERS 18

1. Azimuthal Resolution 18

2. Phase History (stationary point target) 19

3. Coherent Integration Time 20

4. Doppler Bandwidth 20

5. Time Bandwidth Product 21

C. EFFECT OF POINT TARGET MOTION 22

D. APPLICATIONS TO IMAGING OF MOVING OCEAN SURFACE 23

1. Velocity Bunching Imaging Mechanism 24

2. Noncoherent Motion Effects 26

3. SAR Two-Scale Backscattering Model 27

4. SAR Mapping Transfer Function 28

E. INTERFEROMETRIC SAR (INSAR) 29

1. Principle of Imaging Ocean Surface Velocity Fields 29

2. INSAR Limitations 30

a. Platform Stability 30

b. Backscattering Surface Roughness Coherence 31

IV. THEORETICAL ANALYSIS OF INSAR IN IMAGING OCEAN SURFACE DYNAMICS 33

A. INTRODUCTION 33

B. INSAR IMAGING OF THE OCEAN 34

C. DERIVATION OF THE CROSS-COVARIANCE OF THE COMPLEX RADAR REFLECTIVITY FOR INSAR 38

D. ESTIMATION OF SCENE COHERENCE TIME 47

1. Estimation of Scene Coherence Based on Pierson-Moskowitz Spectra 47

2. Estimation of Radar Scene Coherence Time Based on SAR and INSAR Simultaneous Images 54

V. REFRACTION SHOALING AND DIRECTIONAL SPECTRA OF NEARSHORE OCEAN WAVES 58

A. INTRODUCTION 58

B. TRANSFORMATION OF NEARSHORE OCEAN WAVES 58

1. Wave Refraction and Shoaling 59

2. Refraction 59

3. The Ray Tracing Model 62

C. OBSERVATION METHODS FOR OCEAN WAVE SPECTRA . . 64

1. Ocean Surface Wave Field Spectra 65

2. Relation to Measurement Methods 67

3. Wave Directional Spectrum 68

VI. THE MONTEREY BAY WAVE FIELD AND CURRENTS '89 REMOTE SENSING EXPERIMENT 75

A. INTRODUCTION 75

B. THE EXPERIMENTAL SITE 77

C. THE MARINA EXPERIMENT 80

D. ENVIRONMENTAL CONDITIONS 88

1. Introduction 88

2. Evolution of Environmental Conditions 91

3. Surface Winds and Pressure Fields 91

4. Satellite Data 97

E. INSTRUMENTATION CHARACTERISTICS AND PERFORMANCES 97

1. Platforms 98

2. *In Situ* Assets 98

3. Platform Characteristics 99

a. NASA/JPL DC-8 99

b. R/V Ricketts 100

4. *In Situ* Assets Characteristics 100

a. Shallow Water Wave Array 100

b. Wind Speed and Direction from Skyvane Wind Sensor . . 100

c. Lagrangian Drifters 104

d. Mini-Ranger Navigation System 105

F. DATA ACQUISITION AND INITIAL DIGITAL PROCESSING . 109

1. Airborne Radar Data 109

a. Range Compression 109

b. Azimuth Transform 110

c. Range Cell Migration (RCM) Correction 110

d. Azimuth Compression 110

2. Pressure Array Data 111

3. Lagrangian Drifter Data 112

4. Global Positioning System (GPS) Data 113

5. Summary 114

VII. DATA ANALYSIS METHODS AND RESULTS 115

A. INTRODUCTION 115

B. SAR AND INSAR IMAGE PROCESSING 115

1. Geometric Correction 116

2. Radiometric Correction 116

3. Computation of Image Coordinates 117

4. Interferometric Phase Images 118

C. MEAN SURFACE WIND DIRECTION ESTIMATION 121

D. CORRELATION OF OCEAN SURFACE REFLECTIVITY WITH WIND DIRECTION 126

E. ESTIMATION OF SCENE COHERENCE TIME 127

F. AMBIENT SURFACE CURRENT ESTIMATES FOLLOWING DRIFTING BUOYS 128

1. Positional Accuracy 128

2. Accuracy of Velocity Estimates 131

G. INSAR MEASUREMENT AND GROUND TRUTH OF NEAR-SHORE OCEAN SURFACE CURRENTS 132

1. Additional Considerations and Processing 133

2. Comparison of INSAR Current Estimates with Lagrangian Drifter Measurements 134

H. OBSERVATION OF SPATIAL AND TEMPORAL NEARSHORE OCEAN WAVE SPECTRA 138

1. INSAR Two-Dimensional Wavenumber Spectra 138

2. Shallow Water Array Directional Spectra 139

3. Comparison of INSAR 2D Wavenumber Spectra with Temporal Wave Array Spectra 140

VIII. RESULTS AND DISCUSSION 151

A. INTRODUCTION 151

B. TEMPORAL RADAR COHERENCE OF THE OCEAN SURFACE 151

C. INTERFEROMETRIC SAR REMOTE SENSING OF OCEAN SURFACE CURRENTS 156

1. Limitations of Measurement Methods 157

2. Current Measurement Conclusions 158

D. OCEAN WAVE SPECTRA 159

1. Results Comparison 160

2. Effects of Airborne SAR System on the Study of Ocean Surface Waves 165

a. Scanning Distortion 165

b. Velocity Bunching 166

c. Coherent Motion Effect 170

3. INSAR Derived Spectra Conclusions 170

E. SOURCE OF SWELLS 171

IX. CONCLUSIONS 174

APPENDIX A 176

APPENDIX B 178

APPENDIX C 182

LIST OF REFERENCES 192

INITIAL DISTRIBUTION LIST 199

LIST OF FIGURES

2.1 Illustration of EM scattering from ocean surface 7

2.2 Specular point backscatter (from Stewart, 1985) 8

2.3 Bragg phenomena in Doppler frequency domain (from Valenzuela, 1978) 13

2.4 Illustration of composite surface approximation (from Stewart, 1985) 15

2.5 Cross-section ratio due to polarization (from Valenzuela, 1978) 16

3.1 SAR geometry 18

3.2 Top view of range to a point target as a function of aircraft velocity (from Hovanessian, 1979) 20

3.3 SAR geometry with respect to azimuth resolution element (after Hovanessian, 1979) 21

3.4 Azimuth image shift 22

3.5 Radar hydrodynamic and straining modulation transfer function and SAR velocity bunching azimuthal transfer function as a function of azimuth angle (from Alpers et al., 1981) 23

4.1 An artistic illustration of SAR geometry in imaging the ocean 35

4.2 Geometry of INSAR: a) top view, b) perspective view 38

4.3 The effect of spreading function $f(\gamma)$ on the scene coherence time τ_c, showing the increase of the scene coherence time with incidence angle 53

4.4 Dependence of scene coherence time on K/K_0 57

5.1 Wave refraction and shoaling 60

5.2 Refraction geometry and notation for Dobson's model 63

6.1 An artistic illustration experiment scenario conducted on July 24 and September 8, 1989 78

6.2 Bathymetric field and ground truth assets in Monterey Bay 79

6.3 Detailed bathymetry of the nearshore region of Marina Beach 81

6.4 Refraction wave ray traces off Marina Beach at different frequencies . 82

6.5 Flight pattern and scene locations for radar data collection on September 8, 1989 off Marina Beach 83

6.6 Buoy deployment positions and Mini-Ranger reference stations during the Marina experiment, September 8, 1989 87

6.7 Monterey Harbor and Moss Landing predicted tides, September 7–9, 1989 90

6.8 Mean sea level pressure contours and wind vectors at 1700 Pacific Day Time on August 31, 1989 92

6.9 Mean sea level pressure contours and wind vectors at 1700 PDT on September 8, 1989 93

6.10 GESOWN wave group velocity vectors and significant wave height contours at 1700 PDT on August 31, 1989 94

6.11 GESOWN wave group velocity vectors and significant wave height contours at 1700 PDT on September 8, 1989 95

6.12 GOES visible imagery at 1331 PDT on September 8, 1989 96

6.13 NASA/JPL DC-8 research aircraft. *Top*: overall view; *Bottom*: SAR antennas 101

6.14 NASA/JPL airborne radar and recording block diagram. The L-band interferometric mode was used for the acquisition of data in this study (from Held et al., 1988) 103

6.15 Light aircraft Piper Cherokee Arrow participated in the Marina experiment, September 8, 1989 103

6.16 R/V Ricketts participated on the final experiment on September 8, 1989 104

6.17 Marina shallow water wave array. *Top*: hardware configuration; *Bottom*: geometric orientation 106

6.18 Wind anemometer at Marina Beach 106

6.19 Plywood drifters used to follow Lagrangianly surface currents in Marina experiment, September 8, 1989. *Top*: perspective view; *Bottom*: apparent drifter 107

7.1 Conventional synthetic aperture radar image of the Marina Beach region in Monterey Bay; *Right*: before radiometric rectification; *Left*: after radiometer rectification. The aircraft attitude was Eastward (90°) 119

7.2 Conventional SAR image of similar area as Figure 7.1 with aircraft attitude in: *Top*: Northward (360°) and *Bottom*: Westward (270°) . . 120

7.3 Radar interferograms off Marina Beach in Monterey Bay, September 8, 1989. Brightness represents surface motions. The aircraft flight path is from right to left along the top of the image (Northward (360°) attitude). A narrow band long crested swell from south-southwest together with a wider band wave field from north-northwest are clearly observed as the propagate ashore. *Top*: before filtering; *Bottom*: after Gaussian filtering 122

7.4 Radar interferograms of the similar area as in Figure 7.3 but for flight paths: *Top*: 90° and *Bottom*: 270° 123

7.5 Salinas River interferograms: *Top*: for flight path 360°; *Bottom*: for flight path 270° 124

7.6 Direct observation of surface currents following Lagrangian drifters near Marina Beach in Monterey Bay, California. The arrows point in the direction of the current and the length of each arrow is proportional to the observed speed 135

7.7 Detailed presentation of Figure 7.6 together with INSAR current estimates (dashed arrows) 137

7.8 Radar interferogram of Marina Beach area, September 8, 1989. The indicated sub-areas were subjected to spectral analysis with results appearing in Figures 7.12–7.15 140

7.9 Observed ray traces — from INSAR spectral analysis versus predicted wave orthogonal orginated for the two swells measured by the shallow water array of Marina Beach. The numbers are the centers (stations) of the 2D FFT sub-areas 141

7.10 *In situ* surface elevation power spectrum measured by the Marina shallow water array on September 8, 1989, 1200–1308 PDT, at a depth of 16 m 144

7.11 *In situ* directional wave spectrum taken at Marina Beach for the same time interval as Figure 7.8; *Top*: 3D representation; *Bottom*: contour presentation 146

7.12 *Top*: Shallow and *Bottom*: deeper water INSAR image spectra of sub-area A1, A2 indicated in Figure 7.8. The circles represent wavelengths as depicted in Figure 7.11 147

7.13 Same as Figure 7.12, but for sub-area B1, B2 148

7.14 Same as Figure 7.13, but for sub-area C1, C2. The top image spectra are obtained from a sub-area close to the Marina shallow water array 149

7.15 INSAR image spectra of sub-area D indicated in Figure 7.8. The strong refraction of the long crested swell in this region smears the spectra 150

8.1 Degradation in azimuth resolution for the NASA/JPL DC-8 L-band SAR for the three flight path images in the Marina experiment, September 8, 1989 153

8.2 Lagrangian drifter versus INSAR surface currents estimates 157

8.3 Relationship between water depth h and predicted wavelength in Monterey Bay; *Top*: for the shorter observed swell $L_0 = 129$ m; *Bottom*: for the long crested swell $L_0 = 395$ m 161

8.4 Relationship between water depth h and predicted direction of wave arrival α in Monterey Bay based on Dobson's refraction model: *Top*: for the shorter swell $L_0 = 129$ m; *Bottom*: for the longer swell $L_0 = 365$ m 162

8.5 Predicted refraction versus INSAR 2D wavenumber spectra angles for the two observed swells (9.1 sec., 15.9 sec.) 164

8.6 Predicted shoaling versus INSAR 2D wavenumber spectra angles for the two wave array *in situ* observed swells (9.1 sec., 15.9 sec.) 164

8.7 INSAR Eastern 90° flight path image spectra computed from: *Top*: Shallow water sub-area close to the Marina wave array; *Bottom*: Deeper sub-area centered 2000 m west from the shallow sub-area. . . 167

8.8 GSOWM directional frequency spectrum obtained from a grid point at 35° N Lat and 122.5° W Long on September 8, 1989. A southerly 16 sec. swell and a 9.5 sec. northwest wave system are observed . . . 172

LIST OF TABLES

4.1 Estimates for Scene Coherence Time as a Function of Wind Speed and Cutoff Wavelength for NASA/JPL DC-8 L-Band Radar with $f(\gamma) = 1$ 52

6.1 System and Flight Data for the Different Aerial DC-8 Aircraft Coverage During Marina Experiment, September 8, 1989 85

6.2 Environmental Conditions During the WAFICIN Marina Experiment 89

6.3 NASA/JPL DC-8 Airborne Imaging Radar Parameters Employed During Marina Experiment, September 8, 1989 102

6.4 Station and Equipment Data 108

7.1 Surface Bragg Wave Phase Velocity Estimated from INSAR Interferogram and linear Theory Phase Velocity 126

7.2 Estimates of Scene Coherence Time as a Function of Incidence Angle Obtained from Three Flight Paths in the Marina Experiment, September 8, 1989 129

7.3 Standard Deviation of Velocity Components (cm/sec) 132

7.4 INSAR Estimates and *In Situ* Observation of Ocean Surface Currents (in cm/sec). Subscript d Denotes Drifter and s for INSAR 136

7.5 Actual INSAR 2D Wavenumber Wave Array Spectra Results and Predicted Refraction and Shoaling Data 142

8.1 Deviation of INSAR Image Spectra Wavelength and Direction from Wave Array and Model Prediction Output 163

8.2 Actual Velocity Bunching Parameters (C, C_{cr}) Estimates Obtained from INSAR Imagery (Northern Flight Path 360°) 169

C.1 Ground and Image Coordinate Data 183

C.2 Image Adjustment Results 189

ACKNOWLEDGEMENT

I wish to express my sincere appreciation to my advisor, Professor Edward Thornton, who guided and supported me in spite of the risk involved in dealing with a new method. Without his inspiration this work could not possibly have been done. I also wish to express appreciation to my entire doctoral committee for their support of my work.

This study about the theory and experimental results of interferometric SAR imagery from the ocean surface was inspired by and has evolved from many earlier contributions to the problem of the imaging response of SAR to the surface of the ocean. Particular works which I wish to acknowledge are: Raney (1971, 1980), Elachi and Brown (1977), Alpers and Rufenach (1979, 1980), Valenzuela (1980), Schuchman and Kasischke (1981), Lyzenga and Shuchman (1983), Plant and Keller (1983), Hasselmann et al. (1985), Alpers et al. (1986), Kasilingam and Shemdin (1988), and Vachon et al. (1988).

I wish to thank many individuals whose various contributions throughout the development of this dissertation helped to shape the final product. Dr. Richard Goldstein from JPL provided the digitized remote sensing data and supported me through many helpful discussions; Dr. Gaspar Valenzuela who agreed to devote his time and serve actively onboard my doctoral committee; Dr. Lev Shemer for his unwavering support; Mr. Robert Wyland for his support on the processing of the wave array data; Mr. Floyd York for building the Lagrangian drifters; and Dr. Kasilingam who provided fruitful ideas and also became my friend. I appreciated the effort and excitement of CDR Kurt Schnebele in assisting me with the image coordinate ground truthing and Mini-Ranger data. I wish to thank also Miss Donna Burych from the IDEA Lab for her instrumental support.

I am very thankful to Mr. Jim Allen for typesetting this document. His dedication and proficiency produced this fine looking document.

Lastly, I wish to express my gratitude to my entire family; my daughter Michal, my son Ohad and especially to my wife Ronit for supporting me over the years with an inexhaustible supply of love, encouragement, and understanding.

I. INTRODUCTION

A. INTERFEROMETRIC RADAR REMOTE SENSING OF OCEAN SURFACE VELOCITY FIELDS

Historically, oceanography has depended on sparse observations made from ships. Now, orbiting platforms offer global coverage of the world's oceans using various types of sensors in a broad spectrum (visible, IR, microwave). "How relevant are these surface observations in understanding today's oceanographic problems? How well matched to the oceanic time and space scales are the satellite samples? What oceanic processes can be observed, and in what way? And, finally, what instruments and systems exist to provide oceanic data from space?" (Stewart, 1985).

Some of the answers to these questions are addressed in this study by applying a new method of remotely measuring ocean surface velocity fields, using a conventional Synthetic Aperture Radar (SAR) augmented with two spatially separated antennas (Goldstein and Zebker, 1987). By incorporating the physics of interferometry, this unique remote sensing method offers an opportunity for estimating *synoptic spatial structures of ocean near surface currents and wavefields with high grid nominal resolution (12 m in this work) and large coverage, never before obtained.*

The objectives of this research are to develop a theoretical foundation for Interferometric SAR (INSAR) in imaging the free surface, distributed moving ocean surface, to verify its feasibility with simultaneous ground truth experiments, and to develop interferometric SAR image processing techniques to estimate spatial synoptic currents and wave spectra. An experiment was conducted to ground truth the

velocity field imagery of INSAR using surface Lagrangian drifters, wind measurements, and a shallow water wave array.

B. STATEMENT OF OBJECTIVES AND PROBLEMS

Three specific objectives are outlined for this dissertation:

1. To develop a theoretical basis for the capability of SAR in an interferometric mode to measure the ocean surface velocity field. The basic limitations in correlating the backscatter radar echo with ocean phenomena is that the ocean surface combines random fluctuating, non-stationary and non-homogeneous scattering elements. In this study, a preliminary theoretical model is developed which represents the major physical parameters involved in remotely measuring near surface currents and wavefields using synthetic aperture radar in an interferometric mode.

The decorrelation of the ocean surface scene (finite scene coherence time) as a function of INSAR parameters is quantified. This allows to characterize the sensitivity and capability of INSAR in terms of imaging near surface ocean currents and wave fields. Noncoherent motion effects on airborne SAR (and hence, INSAR) imagery, which is an area of controversy, is also addressed in the present study.

2. To develop analysis techniques to obtain quantitative spatial information of near ocean surface currents and wave fields from INSAR imagery. Unlike SAR, which has serious shortcomings in obtaining directional wave spectra, INSAR has an inherent improved potential of measuring 2D wavenumber spectrum of the ocean surface dominant wave field. This improvement is related to the direct motion detection mechanism of INSAR when sufficient Bragg scatterers are present. In this study, appropriate theoretical tools are developed to separate wave field velocities from ocean currents. This separation allows accurate and unique information concerning spatial structures of dominant ocean wavefields, currents, and other features.

3. To ground truth the currents and wave fields measured by INSAR. A simultaneous *in situ* and radar remote sensing experiment was conducted to determine the feasibility of INSAR to image near surface ocean dynamics compared with more conventional measurements. The analyzed data also provide a unique study of wave refraction and shoaling and currents in the complex nearshore region of Marina in Monterey Bay.

C. SUMMARY

The present study demonstrates the feasibility of this unique technique to provide reliable quantitative spatial information about dynamic processes at the ocean surface. Realization of the potential of INSAR with spacecraft might make it possible to routinely monitor global ocean wave spectra and surface currents. A review of electromagnetic interaction with oceanic backscattering waves is presented in Chapter II along with backscattering models which supports the interpretation of the results. The principal mechanisms of SAR and INSAR and relevant theory in imaging ocean surface dynamics are presented in Chapter III. In Chapter IV, a preliminary theoretical analysis for INSAR in imaging ocean surface velocity fields is presented for the first time. Based on the SAR two-scale model, a theoretical model for estimating the temporal decorrelation of the ocean surface using simultaneous SAR and INSAR observations is also developed. Chapter V describes oceanographic relevant theory which is essential for the interpretation of the results. A numerical refraction model (Dobson, 1967) is used to predict wave length and direction in shallow water. These outputs are compared with INSAR spectral analysis estimates (Chapter VII). Two-dimensional wavenumber spectra for *in situ* and interferometric SAR are successively described. A description of the experiment, environmental conditions, and data processing follows in Chapter VI. Data analysis methods and

experimental results are presented in Chapter VII. Results, analysis, and discussions are given in Chapter VIII. These findings are summerized and the major conclusions and suggestions for further study are stated in Chapter IX.

II. LITERATURE REVIEW

A. INTRODUCTION

Due to rapid advances in microwave remote sensing of ocean surface during the last decade, much progress has been made in understanding the physics of scattering of microwave radiation from the ocean surface (Hasselmann et al., 1985; Thompson, 1989). The result of this progress yields a capability to observe in more detail near-surface ocean features such as: wave height, wind speed, spatial wave field data, tides, eddies and currents (Valenzuela, 1989).

The interpretation of microwave remote sensing data is done through the physics of microwave scattering theories. Therefore, the discussion in this chapter begins with the mechanisms of electromagnetic scattering from ocean surface for real aperture radars, which is the basis of radar scattering theory. Next, the discussion extends to coherent synthetic aperture imaging radars, which in turn adds the comple motion effects when sensing the ocean. The complexity is mainly a result of the random uncorrelated motion of individual scatterers, smaller than the spatial resolution cell of SAR and of the order of the radar wavelength. The interaction between different scales of waves and currents smear and defocus the SAR image, resulting in difficulties in correlating the image with the sensed phenomena (see Chapter IV). In spite of the difficulties, considerable progress has been made in understanding SAR imagery of ocean surface features. (Raney, 1971; Elachi, 1977; Alpers and Rufenach, 1979; Valenzuela, 1980; Plant and Keller, 1983; Tucker, 1984; Hasselmann et al., 1985; Kasilingham and Shemdin, 1988).

B. ELECTROMAGNETIC FIELDS SCATTERED FROM THE OCEAN SURFACE

The interaction of electromagnetic waves with ocean surface is a complex boundary value problem, for which exact solutions are not available to the present time (Barrick, 1968; Valenzuela, 1971). This is because the ocean surface is a complex distributed scatterer, varying in time and space, and also weakly nonlinear behaving as a random rough surface. In the linear approximation, the statistics of the ocean surface are homogeneous, stationary, and Gaussian. With these assumptions, several fundamental electromagnetic backscatter models, in good agreement with observations, have been derived (Barrick and Peake, 1968; Barrick, 1968, 1972; Hasselmann, 1971; Kirshen, 1971; Daley, 1973; Valenzuela, 1974, 1978; among others). These models are based upon:

- The high frequency methods, including geometric and physical optics which yield specular point models for smooth and undulating surface (Kerr, 1951).
- The low frequency method, using the perturbation method for a slightly rough surface yields the Bragg scattering model (Rice, 1951).
- Combination of high and low frequency methods renders the two-scale composite model for rough surfaces.

The purpose of these fundamental models of microwave scattering from the ocean surface is to convert the received electric signal at the sensor into a meaningful geophysical signal. These models (specular, Bragg-Rice, and composite) are described extensively in a review paper by Valenzuela (1978), which remain the basis for studies of ocean surface dynamics sensed by microwave sensors even in the present time (see Figure 2.1). Recently, the composite model has been extended to

incorporate a third intermediate scale utilized specifically for SAR imagery applications. This theory is summarized in great detail in a consensus paper by Hasselmann, Raney, Plant, Alpers, Shuchmann, Lyzenga, Rufenach, and Tucker, 1985. The scattering of electromagnetic fields from random rough surface differs from deterministic surfaces scattering by being statistical in nature. Mean values of the fields and power may be determined by ensemble averaging these quantities over the assumed or known statistics of the rough surface (Beckmann and Spizzichino, 1963).

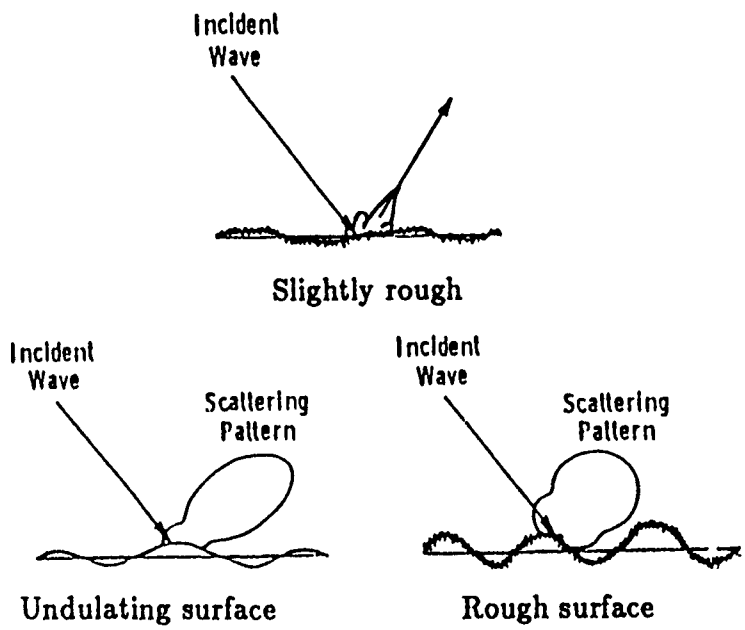

Figure 2.1: Illustration of EM scattering from ocean surface.

Following Valenzuela (1978), the scattered power density is given by the mean magnitude of the Poynting vector, which is a cross product of the electric and

magnetic fields

$$P_s = \frac{1}{2} R_e \langle \mathbf{E}_s \times \mathbf{H}_s^* \rangle \tag{2.1}$$

where $\mathbf{H}_s^*$ is the complex conjugate of the scattered magnetic field of the EM wave, and $\mathbf{E}_s$ is the scattered electric field of the EM wave. The brackets denote ensemble average.

A measure of scattering power from a rough surface can be related to the radar cross-section, which is proportional to the ratio of the scattered power from the surface to the incident power. For the far field:

$$\sigma = \lim_{R \to \infty} (4\pi R^2 \langle |E_s|^2 \rangle / |Ei|^2) \tag{2.2}$$

where $|Ei|^2$ and $\langle |E_s|^2 \rangle$ are the incident and mean scattered power respectively. R is the distance of the observation point from the scattering rough surface.

In the following sections the specular, Bragg-Rice, and the composite scattering models are presented.

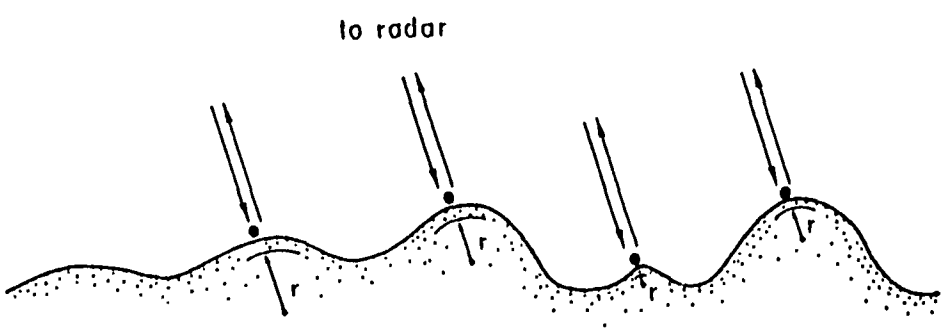

Figure 2.2: Specular point backscatter (from Stewart, 1985).

1. Specular Point/Physical Optics Model

In this model, the reflections are from surface slopes which are oriented normal to the line of sight of the radar (Hagfors, 1964). The principal assumptions

of this model are that the surface radius of curvature is almost everywhere much larger than the radar wavelength (physical optics or Kirchhoff method), and that multiscattering and/or shadowing are negligible (see Figure 2.2). The range of validity of physical optics, or the tangent plan approximation, was shown by Shmelev (1972) as:

$$2rk_R \cos\gamma \gg 1 \quad \text{and} \quad \frac{1}{2} rk_R \cos^3\gamma \gg 1 \tag{2.3}$$

where r is the local radius of curvature of the surface, γ and k_R are the incidence angle and the wavenumber of the electromagnetic wave in free space respectively.

The backscatter power from a single facet (local tangent plan) is a function of the probability that the tangent plane/facet will be oriented perpendicularly to the incidence direction of the electromagnetic wave. Summing up the contributions from all properly oriented facets within the resolution cell of the radar results in the total backscatter specular power.

Applying the physical optics approximation, Barrick (1968) derived a specular model to predict the normalized radar cross section for backscatter from a finitely conductive rough surface:

$$\sigma_0 = (\pi/\cos^4\gamma) p(\eta_x, \eta_y) |\rho(0)|^2 \tag{2.4}$$

where $p(\eta_x, \eta_y)$ is the joint-probability density of orthogonal slopes η_x and η_y of the sea surface η with respect to the incident EM wave and $\rho(0)$ is the Fresnel reflection coefficient for normal incidence. The slopes are the horizontal derivatives of the local vertical displacements of water surface from mean level.

A simplified form of Equation (2.4) is achieved by assuming that the ocean surface roughness has a Gaussian random distribution. Thus, for an upwind looking radar, Equation (2.4) becomes:

$$\sigma_0 = \frac{|\rho(0)|^2}{2S_u S_c} \sec^4(\theta) \exp\left[-\tan^2\theta/2S_u^2\right] \tag{2.5}$$

where S_u^2 and S_c^2 are the mean square slopes of upwind and crosswind respectively. Verified by observations, Equation (2.5) seems to be a good approximation for near normal backscatter from an undulating surface.

Radar observations for the ocean indicate that the specular backscatter is 2 to 3 times larger from a trough than from a crest (Yaplee, 1971; Valenzuela, 1978). This could be due to "compressibility" of the short gravity-capillary waves at the crests of the long waves, resulting in a diffuse scatter which reduces the specular backscatter. The reflection properties of a surface are known to be reduced by increase in roughness. Away from normal incidence, the backscatter is no longer specular, but diffuse, being produced by shorter waves which have steeper slopes (roughness).

2. The Bragg-Rice Model

For a slightly rough surface, to first order, the backscatter energy, in directions of at least 20 degrees from normal incidence, is proportional to the ripple variance spectrum evaluated at the Bragg resonant wave number (Hasselmann et al., 1985)

$$k = 2k_R \sin\gamma \tag{2.6}$$

where k is the ocean wavenumber, and $k_R \sin\gamma$ is the projection of the incident radar wave number onto the ocean surface. This diffraction grating (resonant) backscattering theory for e.m. waves, was first developed by Rice (1951) and demonstrated experimentally by Crombie (1954) with an HF Doppler radar. The Doppler spectrum showed two peaks shifted from the EM frequency by the positive and negative Bragg waves frequency, for waves propagating towards and away from the sensor.

Since the resonant (Bragg-Rice) backscattering mechanism has been shown to be the dominant backscatter for the ocean surface for incidence angles

ranging from 20 to 70 degrees, typical for SAR remote sensing, this backscattering mechanism is reviewed in more detail, together with the composite surface model introduced in the next section.

The main assumptions in deriving the first order Bragg-Rice model are:

- Local matching of the fields at the surface with linearized boundary conditions. Hence, the surface vertical perturbations, h, of the Bragg ripples are small with respect to the radar wavelength (Rayleigh condition).
- The number of resonant scatterers is large enough to allow a proper statistical description of the backscattered reflectivity.
- The slopes of the Bragg waves are assumed small. Jordan and Lang (1972) argue that this condition represents the real ocean because water waves break long before they become large enough to violate the linear boundary condition.

Based on these assumptions, the resonant scatter theory yields a normalized radar cross section (Wright, 1966; Barrick, 1972; Jordan and Lang, 1979):

$$\sigma_0 = 8\pi k_R^4 |g_{ij}(\gamma)|^2 \psi(2k_R \sin\gamma, 0) \tag{2.7}$$

where $g_{ij}(\gamma)$ are the first order scattering coefficients and $\psi(k_x, k_y)$ is the two dimensional ocean wave number spectrum properly normalized. The indices, (i, j) denote transmitted and received polarizations respectively:

$$g_{ij}(\gamma) = \begin{bmatrix} g_{HH}(\gamma) & g_{HV}(\gamma) \\ g_{VH}(\gamma) & g_{VV}(\gamma) \end{bmatrix} \tag{2.8}$$

Depolarization effects for the ocean surface are generally smaller (of higher order) than the copolarized contribution, therefore only scattering coefficients with unchanged polarization with respect to the transmitted polarization are considered

here:

$$g_{HH}(\gamma) = \frac{(\varepsilon_r - 1)\cos^2\gamma}{\left[\cos\gamma + (\varepsilon_r - \sin^2\gamma)^{\frac{1}{2}}\right]^2} \tag{2.9}$$

$$g_{VV}(\gamma) = \frac{(\varepsilon_r - 1)[\varepsilon_r(1 + \sin^2\gamma) - \sin^2\gamma]\cos^2\gamma}{\left[\varepsilon_r\cos\gamma + (\varepsilon_r - \sin^2\gamma)^{\frac{1}{2}}\right]^2} \tag{2.10}$$

where ε_r is the relative complex dielectric constant.

Away from normal incidence, Bragg resonant scattering yields an increasing polarization ratio with increasing incidence angle, with a larger vertical polarization scattering coefficient. For a surface with perfect conductivity, $\varepsilon_r = -i\infty$, which is a reasonable assumption for the ocean surface for lower radar frequencies (i.e., HF), Equations (2.9) and (2.10) simplify (Stewart, 1985):

$$g_{HH}(\theta) \sim \cos^2\theta \tag{2.11}$$

$$g_{VV}(\theta) \sim 1 + \sin^2\theta \tag{2.12}$$

Therefore, for increasing incidence angles, the horizontal polarization Bragg scattering coefficient decreases in magnitude, and is more sensitive to incidence angles relative to vertical polarization scattering coefficient except for near grazing incidence where the trapped waves and shadowing become dominant.

The backscatter resonant cross-section is directly proportional to the two-dimensional ocean wave number spectrum satisfying the Bragg resonant condition (Equation 2.7), which in turn suggests the usefulness of microwave backscatter for probing ocean waves. If the Bragg water waves are not the dominant waves of the ocean, higher order Doppler shifted backscatter will occur whenever the summation of wavenumber pairs of long waves meet the Bragg resonant condition (Hasselmann, 1966):

$$2k_R\sin\theta = \pm k_1 + (\pm k_2) \tag{2.13}$$

$$\omega_D = \pm\omega_1 + (\pm\omega_2) \tag{2.14}$$

where k_1 and k_2 are the wave numbers of the waves. According to perturbation mathematical constraints, the second order contribution should be smaller compared with the first order Bragg contribution. In practice, some of these higher order contributions representing initial manifestation of tilting and multiple scattering can become comparable to the first order contribution or larger. Typical relative amplitude Doppler spectra were observed by Barrick et al. (1974) using a HF frequency Doppler radar (see Figure 2.3). The Doppler spectrum in Figure 2.3 also shows a frequency shift of the first order Bragg lines due to advection of the waves by currents.

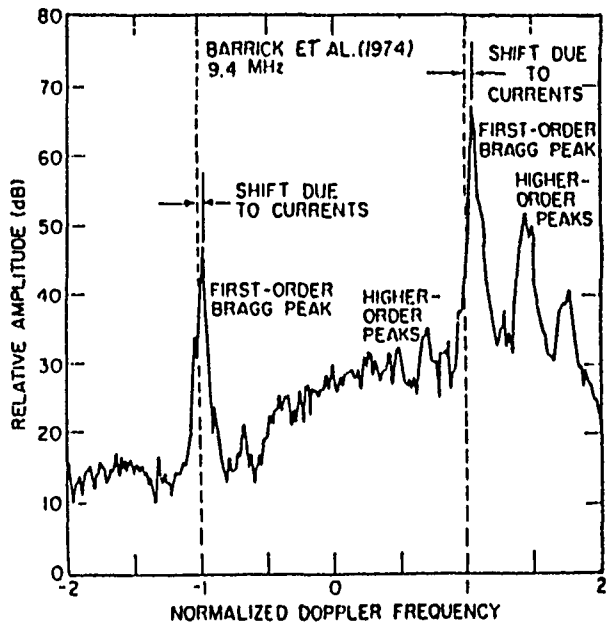

Figure 2.3: Bragg phenomena in Doppler frequency domain (from Valenzuela, 1978).

Wind may induce surface advection drift, which will add to the Doppler shift of the phase speed. Also, rotational (finite amplitude) effects may modify the phase speed of short waves. At high winds as the ocean becomes rougher, the

higher order contributions become significant, and the Doppler spectra becomes broader. The broader Doppler spectra occur when the wind dominant waves are longer than the Bragg waves on the ocean. When the Bragg resonant waves are generated on longer dominant ocean waves, the mean surface for the Bragg waves is no longer flat but undulating. For this typical ocean surface, a composite, or two-scale hydrodynamic model is suggested in the literature.

3. Composite Surface Model

The observation that Bragg resonant theory by itself does not predict increased radar backscatter in the presence of longer waves led Bass et al. (1968) and Wright (1976) to suggest a more tractable two scale-composite surface backscatter model. This model represents short Bragg waves riding on longer waves by approximating the ocean surface as a sum of infinite number of slightly rough patches (Figure 2.4). The composite model predicts, therefore, the radar cross-section for a single patch as given by (Wright, 1968; Valenzuela, 1978; Brown, 1978):

$$\sigma_{HH}(\theta_i) = 8\pi k_R^4 \left| \left(\frac{\alpha \cos\delta}{\alpha_i}\right)^2 g_{hh}(\theta_i) + \left(\frac{\sin\delta}{\alpha_i}\right)^2 g_{vv}(\theta_i) \right|^2 \psi(2k\alpha, 2k\gamma \sin\delta) \quad (2.15)$$

where $\alpha_i = \sin\gamma_i$, $\gamma_i = \cos(\gamma + \Psi)\cos\delta$, $\alpha = \sin(\gamma + \Psi)$ and $\gamma_i = \cos\theta_i$, and Ψ, δ are the local sea surface slopes (small angles), $g_{hh}(\theta_i)$ and $g_{vv}(\theta_i)$ are the first order scattering coefficients of a local patch. σ_{VV} is computed with a similar formula, but it is much less sensitive to variations in local facet tilts. Thus, the contribution from all slightly rough patches over the distribution of slopes $p(\eta_x, \eta_y)$ of the dominant waves within the radar resolution cell, is given by:

$$\sigma_{HH}(\theta) = \int_{-\infty}^{\infty}\int_{-\infty}^{\infty} \sigma_{HH}(\theta_i) p(\tan\Psi, \tan\delta) d(\tan\Psi) d(\tan\delta) \quad (2.16)$$

Normally, the backscatter from a slightly rough surface modulated by long waves is approximated including both the contribution from a specular point

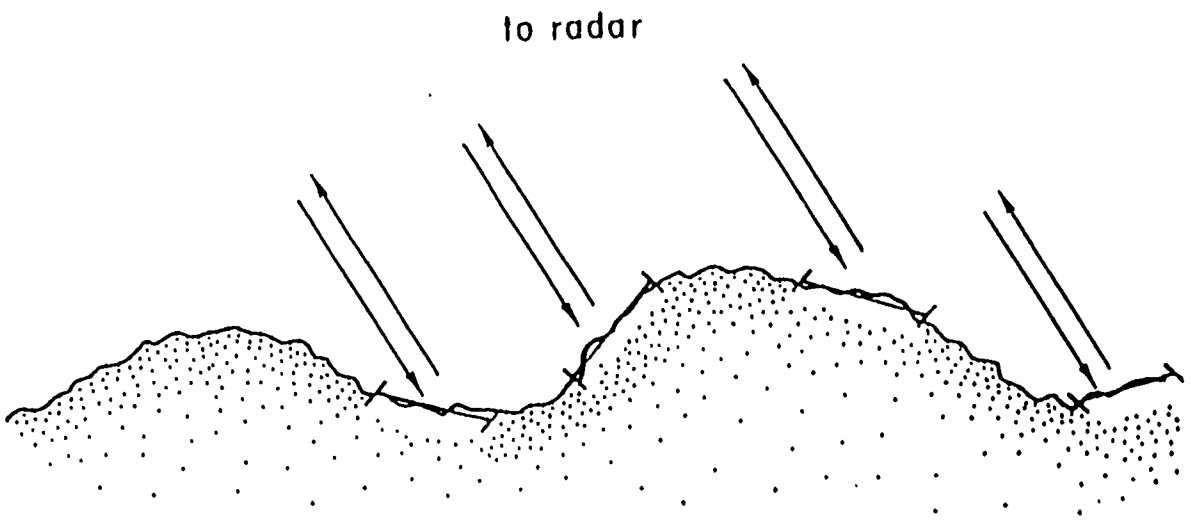

Figure 2.4: Illustration of composite surface approximation (from Stewart, 1985).

model and that predicted by the composite surface model (Hasselmann et al, 1985). The tilted facets significantly modify the radar cross-section, especially for the horizontally polarized radiation with a depolarized contribution (Stewart, 1985).

Towards grazing incidence the polarization ratio decreases as the sea appears rougher, a phenomenon which illuminated Wright to develop the composite model. The cross-section polarization ratio as a function of incidence angle and roughness parameter is illustrated in Figure 2.5. At grazing incidence a modified model including a combination of composite surface and wedge scattering was suggested by Kalmykov and Pustovoytenko (1976) to explain Doppler spectra from the ocean. This combined backscatter model predicts larger backscatter and greater Doppler shift for horizontal polarization (at grazing incidence), rather than for vertical polarization.

4. Application of Composite Model to SAR

For purposes of interpreting coherent imaging observations, the actual scattering from a moving surface like the ocean can be represented by a superposi-

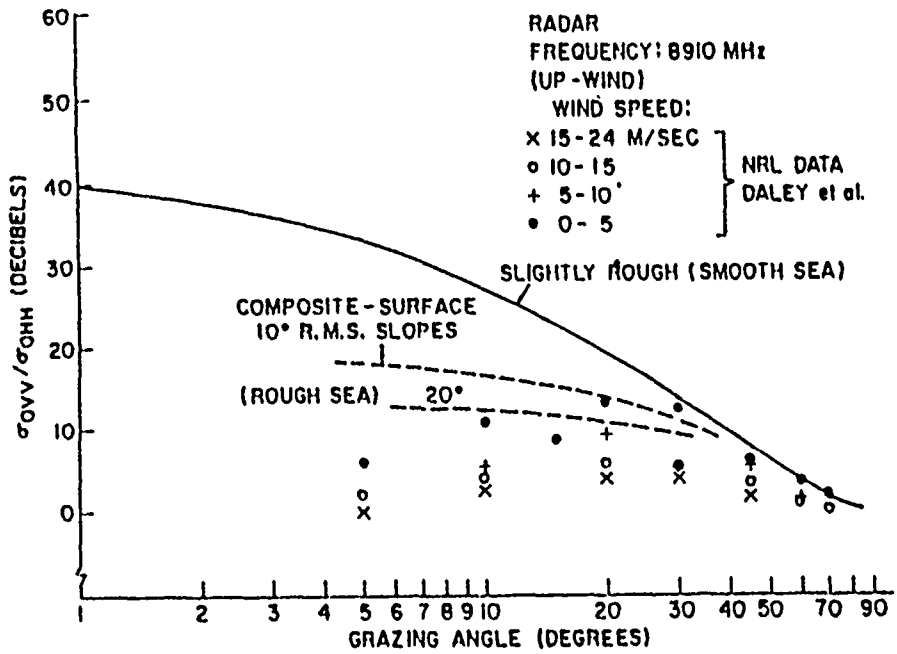

Figure 2.5: Cross-section ratio due to polarization (from Valenzuela, 1978).

tion of the specular and composite theories as described above (however, it is not uncommon to include specular scattering in the definition of composite theories), plus complex motion effects from a non-rigid distributed surface. The interpretation of images from the ocean surface, is still an area of active research. Elachi (1977); Hasselmann et al. (1985), and Alpers and Bruening (1986) have given some insight to SAR imaging models of the ocean surface. Some of their considerations will be described in Chapter III. D.

III. PRINCIPAL MECHANISMS OF SAR AND INSAR IMAGERY RELEVANT TO THE OCEAN SURFACE

A. INTRODUCTION

In this chapter the fundamental principles of SAR imaging are briefly described first, since the suggested interferometric technique is based on conventional SAR. A synthetic aperture radar is an imaging sensor, with a high (two dimensional) spatial resolution in azimuth (along track) and in range (across track) directions (Harger, 1970; Hovanessian, 1979). High azimuthal resolution is achieved by translating a coherent radar on-board a moving platform, storing the amplitude and phase histories returned from the target, and subsequently processing the stored data to remove known quadratic phase errors across the antenna beam. Improved range resolution is achieved by using spread spectra techniques, such as pulse compression or bi-phase modulation of the radar carrier frequency (Skolnik, 1980).

The range scanning is at the speed of light in air, but the azimuthal scanning is at the speed of the carrier platform (Hasselmann et al., 1985). For processing purposes this fact leads to substantial decoupling of the range and azimuth processing. The azimuth channel is related directly to the dynamic distortions associated with imaging of ocean surface features, because the time scales of the system and the imaged wave fields are of the same order. Inherently, the range channel does not have such problems. In this chapter, some fundamental parameters characterizing SAR and INSAR operation are described.

B. FUNDAMENTAL PARAMETERS

1. Azimuth Resolution

At any given time and range, the contributions to the radar image from each stationary scattering point at that range can be identified uniquely by its Doppler shift, caused by the sensor motion. This allows the summation of different contributions from different scattering points to produce a phase history in the aperture synthesis.

An antenna with a real aperture D has an azimuthal coverage of (see Figure 3.1)

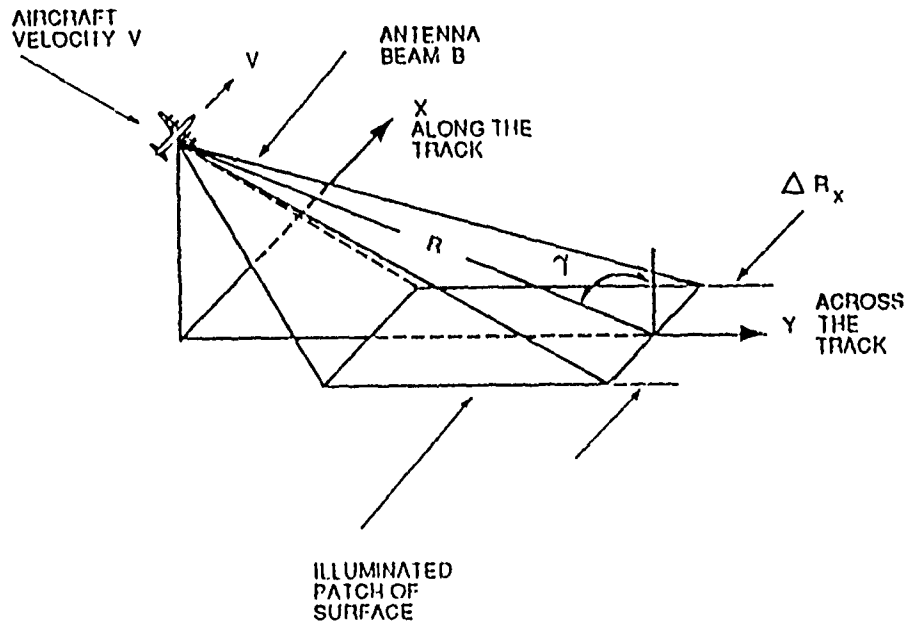

Figure 3.1: SAR geometry.

$$\Delta R_x = \frac{\lambda}{D} R \tag{3.1}$$

where R is the radar target slant range, and λ is the radar wavelength. ΔR_x is the real azimuth resolution with antenna of size D. The length of aperture which can be synthesized depends on the distance the platform travels while a point scatterer is still illuminated. The synthetic aperture for the geometry in Figure 3.1 is ΔR_x,

and its maximum azimuth resolution for a stationary rigid point target is:

$$\rho_{az0} = \frac{\lambda R}{2\Delta R_x} = \frac{D}{2} \tag{3.2}$$

the factor of 2 enters because the effective synthetic aperture "beam-width" is half of a real aperture. From Equation (3.2), the synthetic aperture resolution is independent of the wavelength and range of the radar, and increases with a decrease in the physical size of the antenna (Hovanessian, 1979; Robinson, 1984; Stewart, 1985).

2. Phase History (of stationary point target)

Since the resolution in azimuth direction is based on the local Doppler shift due to aircraft motion, which in turn is the rate of change of phase, the phase history is defined, which is the principle of synthetic aperture imaging radar. Consider a moving SAR with velocity V as illustrated in Figure 3.2. By the time t, the radar moved a distance $L = Vt$, and the range to a stationary point target changed from R_1' to R_0 to R_1. Since the phase of the received signal is proportional to the distance traveled, the phase of this signal will vary with time. The range R can be written as:

$$R = [R_0^2 + (Vt)^2]^{1/2} \tag{3.3}$$

where R_0 is target range of closest approach. By a Maclaurin series expansion around $t = 0$ Equation (3.3) can be rewritten as:

$$R = R_0 + \frac{1}{2R_0}(Vt)^2 - \frac{1}{8R_0^3}(Vt)^4 + \ldots \tag{3.4}$$

Neglecting higher order terms, the phase shift of a stationary point target is (Hovanessian, 1979):

$$\Delta\Phi(t) = \frac{2\pi}{\lambda}\frac{(Vt)^2}{R_0} \tag{3.5}$$

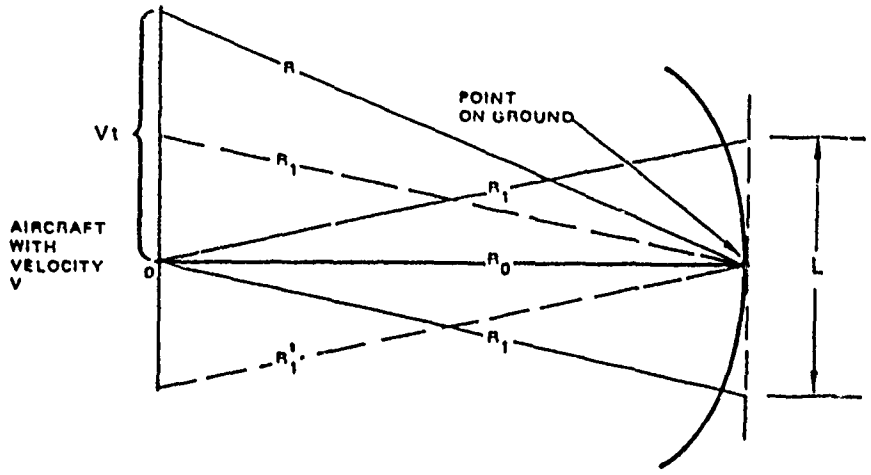

Figure 3.2: Top view of range to a point target as a function of aircraft velocity (from Hovanessian, 1979).

Equation (3.5) states that the Doppler shift from a stationary target is a linear function of time (chirp). Two additional fundamental parameters which determine SAR performance are the processor coherent integration time T and the Doppler bandwidth B.

3. Coherent Integration Time

The upper limit of the theoretical coherent integration time is determined by the real aperture azimuth resolution or more precisely, by the real antenna beamwidth:

$$T = \frac{\Delta R_x}{V} = \frac{\beta R}{V} \tag{3.6}$$

where β is the real aperture beamwidth.

4. Doppler Bandwidth

Consider the scenario depicted in Figure (3.3). The Doppler shift of a stationary point target B is:

$$f_B = \frac{2V\cos\theta}{\lambda} \tag{3.7}$$

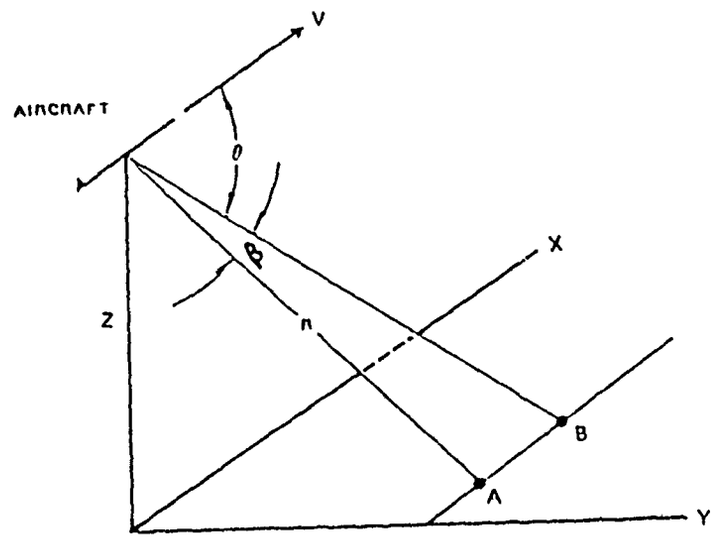

Figure 3.3: SAR geometry with respect to azimuth resolution element (after Hovanessian, 1979).

and the Doppler shift for stationary point target A is:

$$f_A = \frac{2V\cos(\theta+\beta)}{\lambda}$$

Using small angle approximations for the beamwidth β, the available Doppler bandwidth is:

$$B = f_B - f_A = \frac{2V}{\lambda}\beta\sin\theta \tag{3.8}$$

5. **Time Bandwidth Product**

Combining Equations (3.6) and (3.8) the time bandwidth product is:

$$TB = \frac{2R\beta^2}{\lambda} \tag{3.9}$$

Equation (3.9) implies that $TB \gg 1$, a property which allows significant simplifications in analysis where the assumption of stationary phase is allowed (Kerr, 1951).

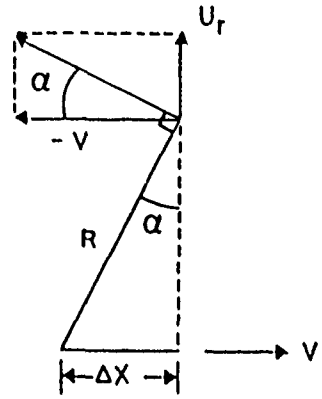

Figure 3.4: Azimuth image shift.

C. EFFECT OF POINT TARGET MOTION

Raney (1971) and Alpers and Bruening (1986), among others, give a clear description of the effect of point target motion on SAR image. Following Alpers and Bruening (1986), consider a point target with radial velocity U_r in the cross track (range) direction as depicted in Figure 3.5. The SAR carrier is moving at V velocity and R is the distance between the SAR antenna and the point target.

A SAR which is tuned for stationary targets, locates targets in azimuth at zero Doppler frequency. Hence, a stationary reasonable target will be located at right angles to the carrier path. However, for the moving target (Figure 3.4), the zero Doppler frequency position, will be shifted in azimuth at an angle $\alpha = \left|\frac{U_r}{V}\right|$ relative to a position of a stationary target. Thus the azimuth image shift of a target with radial velocity is:

$$\Delta x = -\frac{R}{V} U_r \tag{3.10}$$

Evidence of this shift is found in SAR imagery for moving rigid targets with velocity component in the range direction, like ships or trains. Their images are shifted in azimuth direction compared to their wakes or tracks. Keeping in mind fundamental principles of SAR, the imaging of the moving ocean surface is discussed next.

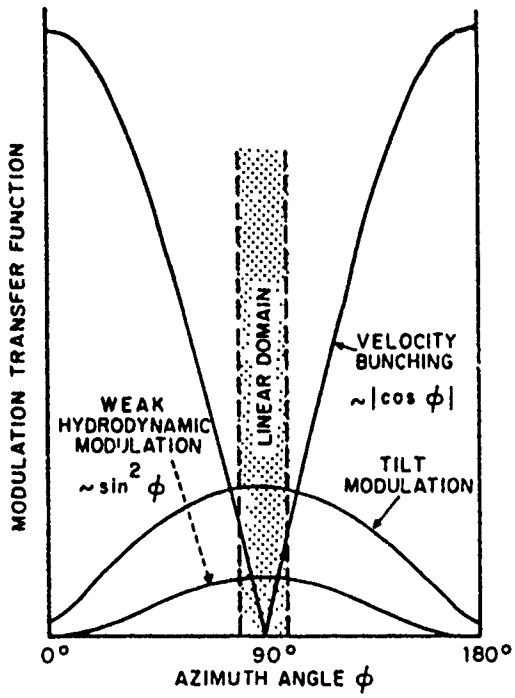

Figure 3.5: Radar hydrodynamic and straining modulation transfer function and SAR velocity bunching azimuthal transfer function as a function of azimuth angle (from Alpers et al., 1981).

D. APPLICATIONS TO IMAGING OF MOVING OCEAN SURFACE

As described in section B of this chapter, microwave scattering from the ocean surface for conventional radars is modeled to an acceptable extent. However, when dealing with imaging radars, two new parameters improving the radar performance and in a way complicating the backscattering process are introduced:

- High spatial resolution (order of tens of meters).
- Doppler information for image generation.

The full implication of these two additional factors on the generation of ocean surface imagery is still in active research (Elachi and Brown, 1977; Kasilingham and Shemdin, 1988).

For a stationary surface, a SAR image is a spatial two-dimensional presentation of the variability of the local coherent backscatter cross section of the surface (Elachi and Brown, 1977). For the ocean surface which is nonstationary, SAR image is a map of the covariance of complex reflectivity (Hasselmann et al., 1985; Kasilingham and Shemdin, 1988). Due to the difficulties in interpreting SAR imagery from the ocean surface, two major resolvable long wave imaging mechanism are still recognized, though they represent conflicting view points. One theory is the *velocity bunching* approach, which is based on the coherent particle orbital velocity of the dominant wavefield (Elachi and Brown, 1977; Alpers and Rufenach, 1979; Swift and Wilson, 1979; Keller and Wright, 1983; Hasselmann et al., 1985; Alpers and Bruening, 1986). The other theory is the *distributed surface* theory which predicts that the SAR image is composed of amplitude modulation due to straining of short backscattering waves and a phase modulation due to tilting by long waves. It assumes that the ocean surface is correlated over distances larger than the SAR intrinsic resolution. (Jain, 1978; Harger, 1986).

1. Velocity Bunching Imaging Mechanism

The *velocity bunching* theory is based on the fundamental assumption that the scattering surface can be divided into individual and uncorrelated scattering elements whose dimensions are small compared to the SAR resolution cell ($\sim 10-20$ m) and large compared to the radar wavelength (5–7 times). Each scattering element (facet) is associated with the local orbital velocity and acceleration of the long underlying waves. This facet motion gives rise to alternating concentrating and spreading of the position of the scattering facets causing amplitude modulation

phase locked to the dominant waves. Following Vachon et al. (1988), the radial line of sight velocities of a monochromatic long wave associated with a scattering element is given by

$$\mathbf{U}(\mathbf{x},t) = \omega A(\sin^2\gamma\sin^2\phi + \cos^2\gamma)^{1/2}\sin(\mathbf{k}\cdot\mathbf{x} - \omega t + tg^{-1}(tg\gamma\cos\phi)) \qquad (3.11)$$

where ϕ is the angle between the aircraft velocity vector and the wavenumber vector $\mathbf{k}$ on the ocean surface plane, and A is the wave amplitude. For swell with a period much longer than the SAR integration time, a scattering element originally at azimuthal coordinate x will be shifted to (Raney, 1988)

$$x' = x + c'\sin(k\cos\phi x) \qquad (3.12)$$

A constant phase term was not included in Equation (3.12). c' is the fractional amplitude of the azimuthal image shift of a scattering element and governs the mapping character. c' is defined as (Alpers, 1983)

$$c' = \left(\frac{2\pi g}{L}\right)^{1/2}\frac{R}{V}A(\sin^2\gamma\sin^2\phi + \cos^2\gamma)^{1/2} \qquad (3.13)$$

Under certain situations the processed SAR image can appear with bright intensity patterns which have twice the spatial period of the actual long wave on the ocean, which can confuse the interpretation of ocean wave analysis. This critical situation is quantified by the parameter c and becomes critical for

$$c'_r = L/2\pi\cos\phi \qquad (3.14)$$

for $c' > L/2\pi\cos\phi$ the scattering element redistribution becomes many-to-one and results in two bright high reflectivity bands associated with one spatial period of the actual ocean wave. For $c' < L/2\pi\cos\phi$, the scattering element redistribution is one to one and results in a single unambiguous high reflectivity band related to

each spatial period of the actual ocean wave. The parameter c_r' is defined by Alpers and Rufenach (1979) as a measure of transition between linear and nonlinear SAR imaging (see Figure 3.4). In terms of the significant ocean wave height, the critical imaging occurs when

$$H_{sc} = \left(\frac{L}{\pi}\right)^{3/2} \frac{V}{g^{1/2} R \cos\phi (\sin^2\gamma \sin^2\phi + \cos^2\gamma)^{1/2}} \tag{3.15}$$

In the above velocity bunching model the ocean surface was assumed commonly (Vachon et al., 1988) to be invariant in its structure and scatter dynamics during the SAR image formation period (coherent integration time). The integration time is considered to be much less than the dominant imaged, wave period. This might not be completely true, especially for airborne SAR. Kasilingam and Shemdin (1988) and others suggest that the noncoherent scene motion (phase velocity) over the image formation period should be explicitly considered in the velocity bunching model.

Additional motion effects of the scattering elements that are sensed coherently by the SAR radar is the dominant wave acceleration that corresponds to the orbital motion and the scattering element decorrelation time scale. Together with the translation of wave patterns during the integration time which enters the image noncoherently, these additional ocean surface dynamics blurs the image. The scene coherence time effect is discussed in detail in Chapter IV. The acceleration defocus is discussed in Chapter VIII.

2. Noncoherent Motion Effects

The translation of mean wave patterns of reflectivity during the course of integration time enters noncoherently into the image in two ways: through distortion in wave length and direction known as scanning distortion and through image

smearing (defocus), also known as look misregistration for a multilook imaging system.

For an monochromatic imaged swell, the noncoherent smearing can be corrected by adjusting the processor focus perturbation to one half the projected wave phase velocity. This operation will enhance the SAR ocean wave image (Jain and Shemdin, 1983).

Scanning distortion is associated with imaging a moving scene from a moving sensor. The along track motion of the scattering cross-section pattern moving at the long wave phase velocity distorts the azimuthal imaged wavenumber. This noncoherent distortion is not related to the coherent phase history of individual scattering elements. If the dominant imaged wave is propagating only in the cross-track direction, only a distortion in wave direction will be practically manifested. The degree of distortion in either wave orientation is proportional to the ratio between the wave phase velocity and platform velocity C/V. The distorted azimuthal wavenumber is taken to be

$$k'_{az} = k_{az} \pm k\frac{C}{V} \tag{3.16}$$

The estimation of scanning distortion from two opposite flights provides an opportunity to resolve the ambiguity of 180° in propagation direction that is inherent to remote sensors.

3. SAR Two-Scale Backscattering Model

Hasselmann et al. (1985) gives a rather complete theory for Bragg scattering using the two scale approach in a review paper. They distinguish between two types of two-scale models:

- The electromagnetic-hydrodynamic two-scale model.

- SAR two-scale model.

The basic difference between these models is the scale of separation between the two wave regimes. In both models, the wave field is treated statistically for wave numbers larger than the scale of separation and deterministically for lower wave numbers. In the electromagnetic-hydrodynamic two-scale model, the scale of separation, k_{emh}, is defined by the expansion requirements of electromagnetic hydrodynamic theory. The scale of separation has to be chosen one order of magnitude smaller than the Bragg backscattering wavenumber, k_b. On the other hand in the SAR two-scale model, the scale of separation, k_{sar}, is determined by the inverse of SAR resolution scale. The SAR two-scale imaging model is based on the physics of the more fundamental two-scale electromagnetic-hydrodynamic model. Typically the k_{emh} is one order of magnitude larger than k_{sar} (see Chapter IV).

4. SAR Mapping Transfer Function

In addition to the Doppler induced modulations (velocity bunching) typical for coherent imaging radars, real radar cross-section modulation tilt and hydrodynamic modulation are commonly used to describe ocean surface imaging. These imaging mechanisms govern the imaging process for waves propagating close to range (cross-track) direction. In this orientation the velocity bunching is nil (see Figure 3.4). For moderate sea states the mapping of the wavefield might be described by a linear transfer function

$$R^{\mathrm{SAR}} = R^{\mathrm{tilt}} + R^{\mathrm{hydr}} + R^{\mathrm{bunching}} \tag{3.17}$$

Usually this situation does not occur, since the mapping is non-linear and the superposition principle does not hold, i.e., the image spectrum is distorted from the actual wavefield. *Electromagnetic interaction*, or tilt modulation of backscatter radar cross section, is caused by the actual variation of local incidence angle. *Hydrodynamic*

modulation of backscatter radar cross section is caused by the interaction of the Bragg waves with the long waves on which they are superimposed. The long wave orbital velocity strains the surface producing areas of current convergence and divergence, resulting in hydrodynamic modulation of the amplitude and wavenumber of the Bragg waves. The surface displacement distorts the air flow over the surface, causing short waves to grow at varying rates (modulated wind stress) for a given wind speed, depending on their relative position on the long wave (private communication, Valenzuela, 1989).

E. INTERFEROMETRIC SAR (INSAR)

1. Principle of Imaging of Ocean Surface Velocity Fields

Interferometric synthetic aperture radar (INSAR) is a relatively new method for measuring ocean surface wave fields, spectra, and currents. Unlike conventional SAR, INSAR has the potential for measuring unambiguously virtual surface velocity fields. INSAR combines large coverage with high nominal spatial resolution ($\sim$ 12 m in this work), good sensitivity and appears suitable for both airborne and probably satellite implementation. The airborne INSAR technique has been developed at Jet Propulsion Laboratories (JPL) by Goldstein and Zebker (1987), and was installed first on a NASA CV990 aircraft and recently on a DC-8 for evaluation experiments.

Following Goldstein and Zebker (1987), the basic technique consists of aligning two antennas along the radar flight path. Pulses are transmitted from the rear antenna and are received simultaneously by both antennas. The resulting signals are converted, separately, into two complex images in the conventional manner for SAR. Any line of sight motion of the identical imaged surface (resolution cell) observed by both antennas is translated into phase difference when these resolution

cells are combined interferometrically. This phase difference, α, is proportional to the virtual measured radian Doppler shift, $\Delta\omega_D$, that occurs in the time it takes for the rear antenna to move to a place of symmetry with respect to the front antenna (see Figure 4.2), where

$$\omega_D = 2\mathbf{k} \cdot \mathbf{U} \tag{3.18}$$

and

$$\alpha = \omega_D \, \Delta t = \frac{2\pi}{\lambda} \frac{B}{V} U_r \tag{3.19}$$

where B is the baseline separation between antennas, V is the aircraft velocity, U_r is the radial component of ocean surface motion and λ is the radar wavelength. Equation (3.19) does not consider speckle contribution from the random ocean surface and/or from the measurement and/or processing system errors. These limitations are reviewed briefly in the next section and further discussed in the next chapter.

The resulting interferogram is a complex image with phase which is the difference of the two original SAR image phases and magnitude which is the product of the two original magnitudes. Practically, the phase and amplitude images are processed into two separate images. For more details see Chapter IV. B.

2. INSAR Limitations

The limitations of INSAR for spatial imaging of ocean surface velocity structure may be categorized into two types: 1) system dependent 2) the degree of coherency of the imaged ocean scene within the inherent time measurement of INSAR.

a. Platform Stability

In order to compare the phases of a rezel (resolution cell) which is observed at two different times, the viewing aspects must be nearly the same. This might not be fulfilled due to lack of accurate knowledge of relative antenna location,

which in turn will result in non-zero velocities and acceleration in the radial direction (antenna pattern disimilarity). For Equation (3.19) to extract accurately the radial component of ocean surface motion, it is assumed that the two antennas are collinear with the radar motion. Aircraft pitch and yaw will add phase difference between corresponding pixels, since one antenna will be closer in range to the observed resolution cell. The radar cannot distinguish between a slight sideways drift of its carrier and the radial motion of the ocean surface. This contamination can be compensated using readouts of aircraft inertial navigation system (INS), or to a reasonable degree, by inclusion of land in the scene to give absolute reference, or a combination of the two. The INS provides aircraft pitch, yaw, pitch and yaw rates, horizontal and vertical velocity, and other flight parameters. With these data, the expected error phase shifts from a stationary scene can be computed and compensated accordingly. A yaw error of 0.01 degrees will yield an error in current estimates of 4 cm s^{-1} (Goldstein and Zebker, 1987).

b. Backscattering Surface Roughness Coherence

The interferometric technique requires comparison of two samples of a moving surface element (resolution cell) in a time interval $\Delta t = B/2V$ required for the rear antenna to move (the mean aircraft speed is 220 m/s) half the distance between the antennas $B/2 = 9.9$ m. It is assumed that in this time increment, $\Delta t = 0.041$ s, the surface wave field as a whole in the resolution cell ($\sim 6 \div 8\times$ 12 m) does not decay or grow, i.e., the scattering patch is nearly stationary. A number of hydrodynamic processes affect the lifetime of Bragg resonant waves. Among these are viscous dissipation and their response (relaxation) to external forcing, such as wind, currents, resonant nonlinear interactions, straining by orbital velocity of long waves, and turbulence. The viscous half life time decay of a 10 cm wave is 63 s. But the lifetime of wind waves are controlled by relaxation processes, which are inversely

proportional to the wind growth rate. Therefore, as the wind speed increases, the relaxation time decreases. For 10 cm waves, the relaxation time is about two seconds for 6 m/s winds (Valenzuela and Wright, 1976). Hence, for moderate sea conditions the ripples should remain nearly constant within the time interval used to measure the phase difference. However, the spread of orbital velocities in the radial direction within the resolution cell will also decorrelate the backscatter complex signal causing an ambiguity of the phase as the ocean wave height changes. An initial attempt to study the limitations of the INSAR technique due to finite scene coherence time is made in the next chapter.

IV. THEORETICAL ANALYSIS OF INSAR IN IMAGING OCEAN SURFACE DYNAMICS

A. INTRODUCTION

In Chapter III. D, the known physical causes for the ocean surface decorrelation were described. The chapter ended with a recommendation that the velocity spread of the scattering elements due to local orbital velocity of the subresolution scale waves should be further analyzed. In this section for the first time, a preliminary theoretical model for an airborne INSAR imaging the ocean surface is given. This model is based on the accepted SAR theory of imaging the moving, nonrigid, distributed ocean surface (e.g., Alpers and Rufenach, 1979; Swift and Wilson, 1979; Valenzuela, 1980; Raney, 1981; Jain, 1981; Rotheram, 1983; Plant and Keller, 1983; Tucker, 1985; Hasselmann et al., 1985; Monaldo and Lyzenga, 1986). It is shown that the limited ocean surface temporal coherency due to the velocity spread of SAR subresolution waves might limit the capability of INSAR in providing virtually instantaneous high resolution snapshots of near ocean surface velocity patterns.

In the analysis given below the SAR two-scale model is assumed implicitly. This model was introduced first by Tucker (1985) who modified the earlier two-scale hydrodynamic model (Wright, 1968, Valenzuela, 1978). The model divides the ocean surface waves into two scales, a subresolution short scale with wave numbers greater than the SAR azimuthal cutoff wavenumber which are treated statistically, and a long scale with wave numbers shorter than this wavenumber which are treated deterministically (see Chapter III. D). It is found that the motions due to subresolution waves produce an azimuthal smearing which can be represented by a Gaussian low pass filter acting on the azimuthal component of wavenumber in the image (Tucker,

1985). This degradation in azimuth resolution (smearing) is inversely proportional to the scene coherence time and determines the nominal azimuth resolution for SAR and INSAR. The scene coherence time for L-band radar will be estimated based on the Pierson-Moskowitz ocean spectrum (350–600 msec) and the backscatter reflectivity of simultaneous SAR and INSAR observations from the Marina experiment on September 8, 1989 ($\sim$ 110 msec).

A major accepted simplification of SAR imaging theory, both for mean image and speckle statistics, follows from the hypothesis that the complex reflectivities at different points on the sea surface are uncorrelated. The spatial separation of the different scattering elements (facets) should be large in comparison with the Bragg wavelength, but still small in comparison with the SAR resolution scale. The surface reflectivity may therefore be regarded as spatially white (after Hasselmann et al., 1985). This assumption will be used in the dirivation of the preliminary model of the ocean surface cross-covariance of complex reflectivity for INSAR.

B. INSAR IMAGING OF THE OCEAN

The complex radar return signal at time t is given by (Kasilingam and Shemdin, 1988):

$$S(t) = \int_{-\infty}^{+\infty} \int_{-\infty}^{+\infty} r(\mathbf{x}, t) f(t - 2R_0/c) A(x - Vt, y) dx dy \tag{4.1}$$

with $\mathbf{x} = \mathbf{x}(x, y)$, see Figure 4.1.

where $r(\mathbf{x}, t)$ is the time variant ocean surface Bragg and specular reflectivity, $f(t - 2R_0/c)$ is the radar pulse function and $A(x - Vt, y)$ is the antenna pattern. We shall ignore the compression effect in the pulse function since the time variation of the returned signal within the pulse duration (few microseconds) is negligible. The range dependence of the pulse function introduces a quadratic phase term. For simplicity assume that the pulse rate is high enough to fulfill the sampling criteria in azimuth

and a continuous signal is transmitted. Therefore, only a quadratic phase term will be introduced by the pulse function. An illustration of an airborne SAR imaging the ocean surface is depicted in Figure 4.1 where k is the radar wave number in the viewing direction, V is the platform velocity and R_0 is the initial aircraft target slant range (see Figure 4.1).

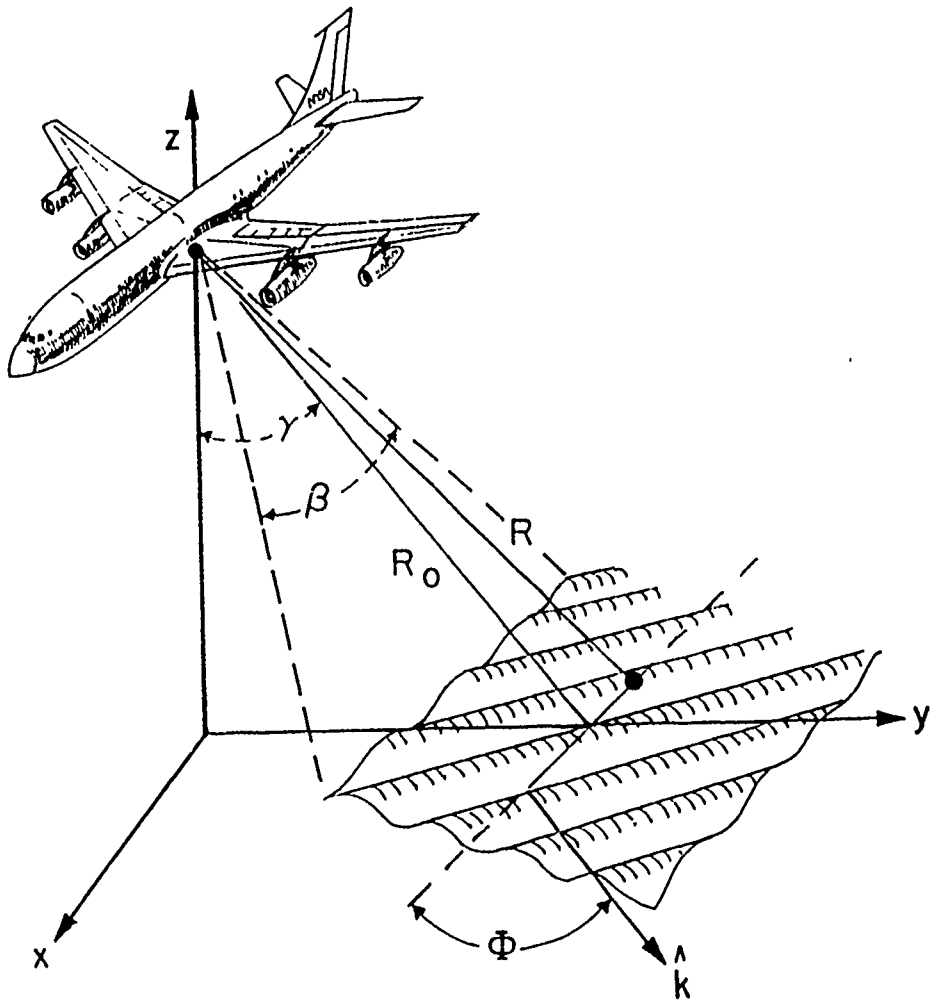

Figure 4.1: An artistic illustration of SAR geometry in imaging the ocean.

The recorded received signals are processed by convolving the records with a matched filter, resulting in the SAR image. For a focused system (see Chapter III)

with no focusing adjustments for wave pattern motions, the matched filter impulse response is taken to be

$$h(x - Vt) = \exp\left[ik(x - Vt)^2/R_0\right] \tag{4.2}$$

The complex conventional SAR image of a pixel from a single antenna is therefore obtained by convolving $S(t)$ given by Equation (4.1) with the matched filter (Equation (4.2)):

$$\begin{aligned} i_1(t = x/V) &= \int_{-\infty}^{+\infty} S(t-\tau)\, h(\tau)\, d\tau = \int_{-\infty}^{+\infty}\int_{-\infty}^{+\infty} r(\mathbf{x}, t-\tau) \\ &\cdot \exp\left[-ik(x - V(t-\tau))^2/R_0\right] A(x - V(t-\tau)) \\ &\cdot \exp\left[ik(x - V\tau)^2/R_0\right] d\mathbf{x}\, d\tau \end{aligned} \tag{4.3}$$

where the first exponential term on the right hand side of Equation (4.3) is the quadratic phase history for a stationary target. Similarly, the corresponding complex pixel image for the second antenna taken at a slightly different time $\Delta t = B/2V$, which is the time required for the rear antenna to move to a place of symmetry with respect to the forward antenna, is given by:

$$\begin{aligned} i_2(t + B/2V) &= \int_{-\infty}^{+\infty} S(t + B/2V - \tau')h(\tau')d\tau' \\ &= \int_{-\infty}^{+\infty}\int_{-\infty}^{+\infty} r(\mathbf{x}', t + B/2V - \tau') \\ &\cdot \exp\left[ik(x - V(t + B/2V - \tau'))^2/R\right] A(x - V(t + B/2V - \tau')) \\ &\cdot \exp\left[ik(x - V\tau')^2/R\right] d\mathbf{x}'\, d\tau' \end{aligned} \tag{4.4}$$

Equations (4.3), and (4.4) represent complex SAR images of the ocean surface reflectivity of the same pixel. The goal is to extract reliably the mean Doppler shift caused by the first order ocean surface motion. This phase information is included entirely in the cross-covariance of the complex surface radar reflectivity $\langle r_1 r_2^* \rangle$ (see Equation (4.6) below). From a statistical analysis point of view, the averages of

$r_1 r_2$ (denoted by brackets) are defined for an infinite ensemble of different surfaces. Practically, the averages are estimated over a finite surface region for a finite time. By taking the cross-covariance of the corresponding complex images from the two antennas, the phase difference, which is proportional to the virtual surface velocities, is obtained. The interferometric operation is therefore given by:

$$Q(x) = \langle i_1(t = x/V)\, i_2^*(t + B/2V)\rangle \tag{4.5}$$

Substituting Equations (4.3), (4.4) into (4.5) yields:

$$\begin{aligned} Q(x) \;=\; & \int_{-\infty}^{+\infty}\int_{-\infty}^{+\infty}\int_{-\infty}^{+\infty}\int_{-\infty}^{+\infty} \langle r_1(\mathbf{x}, t-\tau) r_2^*(\mathbf{x}', t + B/2V - \tau')\rangle \\ & \cdot \exp\left[-ik(x - V(t-\tau))^2/R_0\right] A(x - V(t-\tau)) \exp\left[ik(x - V\tau)^2/R_0\right] \\ & \cdot \exp\left[ik(x' - V(t + B/2V - \tau'))^2/R_0\right] A(x' - V(t + B/2V - \tau')) \\ & \cdot \exp\left[ik(x' - V\tau')^2/R_0\right] d\mathbf{x}\, d\mathbf{x}'\, d\tau\, d\tau' \end{aligned} \tag{4.6}$$

The first term on the right hand side of Equation (4.6) is the covariance of complex reflectivity of the ocean surface, which is defined by the second moment statistics of the ocean surface backscattered signal. As noted in the introduction to this section, the averaged SAR mean image is directly related to these statistics, namely, the covariance of complex reflectivity of the ocean surface. Figure 4.2 illustrates the geometry of INSAR.

The extraction of the phase information from the backscattered moving surface by using Equation (4.5) is the essence of INSAR in imaging the ocean. This is fundamentally different from the SAR image intensity, given by:

$$\langle |i_1|^2\rangle = \langle i_1 i_1^*\rangle \tag{4.7}$$

Equation (4.7) clearly illustrates the loss of the phase information in the SAR image, which is retained in Equations (4.5), (4.6) for INSAR.

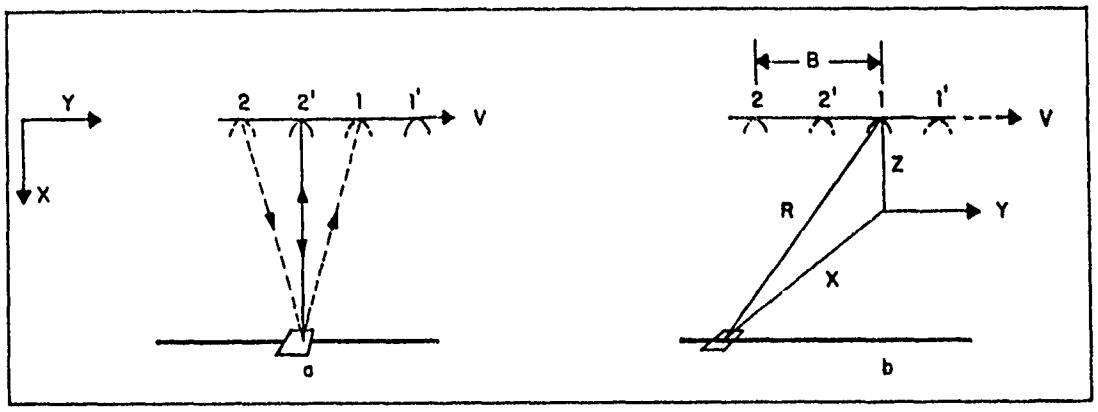

Figure 4.2: Geometry of INSAR: a) top view, b) perspective view shows the change in distance of the resolution element due to wave motion in the time it takes for the rear antenna to more to a symmetric position with respect to the front antenna.

The SAR System Transfer Function (STF) is not considered at the present stage. It is assumed that the SAR is a perfect instrument that maps the covariance of complex reflectivity into a two-dimensional complex image. The interest here is to investigate the feasibility of INSAR in imaging the moving ocean surface. Therefore, the interferometric operation described by Equation (4.5) can be replaced by the cross-covariance of complex reflectivity of an imaged ocean scene sensed by the two INSAR antennas with a time difference $\Delta t = B/2V$.

C. DERIVATION OF THE CROSS COVARIANCE OF THE COMPLEX RADAR REFLECTIVITY FOR INSAR

The complex radar reflectivity for an individual scattering element moving with velocity $\mathbf{U}(\mathbf{x}, t)$ is given by:

$$r(\mathbf{x}, t) = r_0(\mathbf{x}, t)\ \exp\left[2i\mathbf{k} \cdot \mathbf{U}(\mathbf{x}, t)\ t\right] \tag{4.8}$$

where $r_0(\mathbf{x}, t)$ is the instantaneous complex reflectivity of an ocean surface scattering element within the SAR resolution cell. As noted earlier, these scattering elements (facets) are assumed to be large relatively to the resonant backscattering Bragg waves (5–10 times), but much smaller than the SAR resolution cell (rezel).

The cross-covariance of complex reflectivity of a time dependent backscattering surface from corresponding rezels as imaged by the two antennas is given by:

$$\begin{aligned}\langle r_1(\mathbf{x}, t)\, r_2^*(\mathbf{x}', t')\rangle &= \langle r_{01}(\mathbf{x}, t) \exp\left[2i\mathbf{k}\cdot\mathbf{U}(\mathbf{x}, t)\, t\right] r_{02}^*(\mathbf{x}', t') \\ &\quad \cdot \exp\left[-2i\mathbf{k}\cdot\mathbf{U}(\mathbf{x}', t')\, t'\right]\rangle \delta(\mathbf{x}-\mathbf{x}')\, \sigma_0(\mathbf{x}, t) \qquad (4.9)\end{aligned}$$

where $t' = t + \Delta t = t + B/2V$ and $\delta(\mathbf{x}-\mathbf{x}')$ represents the white spatial distribution of the scattering elements within the SAR resolution cell (Hasselmann et al., 1985). $\sigma_0(\mathbf{x}, t)$ is the variance of r and represents the modulation of the covariance of short wave reflectivity by the slow time varying long wave tilt and hydrodynamic modulation. $\sigma_0(\mathbf{x}, t)$ represents the radar cross-section as imaged by conventional SAR and real aperture radars.

In Equation (4.9), the time lag Δt represents only the constant time interval required for INSAR measurement. The additional time difference of $\tau - \tau'$ (see Equation (4.6)), which is of the order of the SAR integration time, is not considered here explicitly (except when determining the effective azimuth resolution). This time difference is not relevant for INSAR operation once the two corresponding complex SAR images are formed. For more detail on the covariance function for SAR, see for instance Hasselmann et al. (1985). The discussion here (Equation (4.9)) is based on analyzing the second order statistics of the fluctuating reflectivity represented by the ensemble term in Equation (4.9) on the time scale relevant for INSAR ($\Delta t = B/2V$).

The SAR two-scale model is invoked resulting in the ocean surface velocities decomposed as

$$\mathbf{U}(\mathbf{x},t) = \mathbf{U}_0(\mathbf{x},t) + \mathbf{U}'(\mathbf{x},t) \tag{4.10}$$

where $\mathbf{U}_0(\mathbf{x},t)$ is the *long scale* velocity and $\mathbf{U}'(\mathbf{x},t)$ is the subresolution *short scale* velocity. $\mathbf{U}_0(\mathbf{x},t)$ can be extracted by INSAR if the temporal variability of the backscattering surface, defined by the radar scene coherence time, is small relative to the time difference $\Delta t = B/2V$ required to obtain the phase image of INSAR which is directly proportional to the mean radial surface velocity.

The limits of the temporal decorrelation of the ocean surface on INSAR in obtaining the surface velocity $\mathbf{U}_0(\mathbf{x},t)$, are now addressed. The variation of the ocean surface velocity $\mathbf{U}(\mathbf{x},t)$ in the time $\Delta t = B/2V$ can be described by using the Taylor expansion

$$\mathbf{U}(\mathbf{x},t+B/2V) = \mathbf{U}(\mathbf{x},t) + \frac{\partial \mathbf{U}(\mathbf{x},t)}{\partial t}\, B/2V \tag{4.11}$$

Substituting Equations (4.10) and (4.11) into Equation (4.9) and factoring out the deterministic *long scale* contributions yields

$$\begin{aligned}
\langle r_1(\mathbf{x},t)\, r_2^*(\mathbf{x},t+B/2V)\rangle \;=\; & \exp\Big[-2i\mathbf{k}\cdot\mathbf{U}_0(\mathbf{x},t)\, B/2V\Big] \\
& \cdot\exp\Big[-2i\mathbf{k}\cdot\frac{\partial \mathbf{U}_0}{\partial t}(\mathbf{x},t)\,\frac{B}{2V}\,\Big(\frac{B}{2V}+t\Big)\Big]\sigma_0(\mathbf{x},t) \\
& \cdot\Big\langle r_{01}(\mathbf{x},t)\, r_{02}^*(\mathbf{x},t+B/2V) \\
& \cdot\exp\Big[-2i\frac{B}{2V}\mathbf{k}\cdot\Big(\mathbf{U}'(\mathbf{x},t)+\frac{\partial \mathbf{U}'(\mathbf{x},t)}{\partial t}\,\Big(t+\frac{B}{2V}\Big)\Big)\Big]\Big\rangle
\end{aligned} \tag{4.12}$$

Equation (4.12) represents the fundamental basis of the present study in evaluating the feasibility of INSAR in imaging the ocean surface. It combines the relevant physics of the backscattering surface as a function of INSAR physical configuration.

The second exponential term on the right hand side of Equation (4.12) can be neglected if

$$\frac{1}{U_0}\frac{\partial U_0}{\partial t}(t + B/2V) \ll 1 \tag{4.13}$$

where t is of the order of the SAR integration time. Since $t \gg B/2V$ and the absolute value of the acceleration of the dominant wave is given by $\partial \mathbf{U}_0/\partial t = \omega \mathbf{U}_0$, inequality (4.13) can be rewritten as:

$$\omega t \ll 1 \tag{4.14}$$

or

$$T \gg 2\pi t \tag{4.15}$$

where T is the period of the imaged dominant wave. Equation (4.15) specifies the limiting condition for the integration time when imaging dominant waves by SAR and INSAR. The effective processing integration time for mean incidence angles (30°) is almost 1.7 sec. In practice, the scene coherence for a given radar wavelength dictates the effective integration time, which is substantially less than 1 sec (e.g., Tucker, 1985). This crucial issue is discussed in the next two sections.

The first term on the right hand side of Equation (4.12) is the required phase shift to be determined by INSAR. It represents the first order ocean surface radial velocities. $\mathbf{U}_0$ is a vector sum of

$$\mathbf{U}_0 = \mathbf{U}_{CP} + \mathbf{U}_{OB} + \mathbf{U}_{CR} + \mathbf{U}_{AR} \tag{4.16}$$

The individual contributions are identified as:

- $\mathbf{U}_{CP}$ phase velocity of the backscattering resonant Bragg waves;
- $\mathbf{U}_{OB}$ mean orbital velocities of waves substantially longer than the characteristic dimension of the resolution cell.

- $\mathbf{U}_{CR}$ material velocity of any near surface currents underlying the backscattering Bragg waves.

- $\mathbf{U}_{AR}$ aircraft attitude error velocity due to yaw and pitch bias of the INSAR antennas (see Chapter III. B).

Practically, the ensemble average factor in Equation (4.12) expresses the additional fading in the cross covariance of complex reflectivity due to the slight time difference Δt when the same scene is imaged separately with a small time delay by the two INSAR antennas. This phenomena is defined here as $c(\mathbf{x}, t, \Delta t)$. These modifications in Equations (4.13), (4.15) substituted into Equation (4.12) yield:

$$\langle r_1(\mathbf{x},t)\ r_2^*(\mathbf{x},t+B/2V)\rangle = \exp\Big[-2i\mathbf{k}\cdot\mathbf{U}_0(\mathbf{x},t)\ B/2V\Big]c(\mathbf{x},t,B/2V)\sigma_0(\mathbf{x},t) \quad (4.17)$$

Both are shown to be quantified as a function of the finite scene coherence time. $c(\mathbf{x}, t, \Delta t)$ can be rewritten as (see Equation (4.12) (4.17)):

$$c(\mathbf{x},t,B/2V) = \exp\left[-2i\frac{B}{2V}\mathbf{k}\cdot\left(\mathbf{U}'(\mathbf{x},t) + \frac{\partial\mathbf{U}'(\mathbf{x},t)}{\partial t}\ \left(t+\frac{B}{2V}\right)\right)\right]\ c'(\mathbf{x},t,B/2V) \quad (4.18)$$

with

$$c'(\mathbf{x},t,B/2V) = \langle r_{01}(\mathbf{x},t)\ r_{02}^*(\mathbf{x},t+B/2V)\rangle \quad (4.19)$$

where $c'(\mathbf{x}, t, B/2V)$ is the temporal cross-correlation function value for the INSAR time difference $\Delta t = B/2V$. The phase term in Equation (4.17) can be rewritten in terms of radian Doppler frequency

$$\omega_{ss} = 2\mathbf{k}\cdot\mathbf{U}'(\mathbf{x},t) \quad (4.20)$$

where ω_{ss} is the perturbation in radian Doppler shift associated with the velocity spread of modulating the subresolution scale wave scattering elements. Substituting

Equation (4.20) into Equation (4.18) yields:

$$c(\mathbf{x}, t, B/2V) = \exp\left[-i\frac{B}{2V}\left(\omega_{ss}(t) + \frac{\partial\omega_{ss}(t)}{\partial t}\, t\right)\right] c'(\mathbf{x}, t, B/2V) \tag{4.21}$$

where $\partial\omega_{ss}/\partial t\ (B/2V)^2$, which is $O(10^{-2})$, is neglected.

In contrast with SAR image intensity which ignores phase information (Equation (4.7)), INSAR imagery represents the virtual phase difference between the two corresponding SAR images. Therefore, the present model (Equations (4.14–4.21)) takes into account additional complex terms which were not considered explicitly in SAR models. We shall further concentrate in evaluating the complex disturbance to INSAR in sensing ocean surface velocities introduced by $c(\mathbf{x}, t, \Delta t)$. This disturbance includes cross section attenuation and additive phase noise, both caused by the subresolution intermediate waves modulating randomly the backscattering elements (facets). The finite temporal coherence of the ocean scene is of special importance since it defines the maximum coherent radar integration time for a given radar wavelength, and therefore the maximum azimuth resolution achievable. In the p. esent study, the effect of the finite scene coherence in the time interval $(B/2V)$ required to obtain the interferometric information based on the corresponding integrated SAR images from the two antennas is discussed.

When considering the radar scene coherence time, two time scales should be looked at:

- *The decorrelation time* of an individual facet within the SAR resolution cell. This fading in the mean complex reflectivity can be described by a temporal decorrelation function.

- *Intrinsic coherence time* in which the Bragg waves of a single scattering element (facet) preserve their structure. It is assumed that this time scale is

long compared with the coherent integration time (Hass., 1985, Vachon et al., 1988).

The temporal correlation function is the inverse Fourier transform of the reflectivity variance Doppler spectrum. Based on theory (e.g., Tucker, 1985) and the TOWARD experiment (1984), it can be assumed that this Doppler broadening of short wave reflectivity has a Gaussian shape. After removing the mean Doppler shift due to long wave and current velocities, the velocity power spectrum of the short wave reflectivity from a given pixel is

$$P(\omega) = \int_{-\infty}^{+\infty} \langle r_{01}(t)\ r_{02}^{*}(t+\tau)\rangle \exp[-i\omega\tau] d\tau = P_0 \exp\left[-\omega_{ss}^2/2\sigma_\omega^2\right], \tag{4.22}$$

where σ_ω is half Doppler bandwidth of $P(\omega)$.

The inverse Fourier transform of Equation (4.22) yields the temporal cross-correlation function of short wave reflectivity at a given point.

$$c'(\tau) = \frac{1}{2\pi} \int_{-\infty}^{+\infty} P(\omega) \exp\left[i\omega\tau\right] d\omega \tag{4.23}$$

Substituting Equation (4.22) into Equation (4.23) yields

$$c'(\tau) = \frac{P_0}{2\pi} \int_{-\infty}^{+\infty} \exp\left[-\omega^2/2\sigma_\omega^2\right] \exp\left[i\omega\tau\right] d\omega, \tag{4.24}$$

where $\omega = \omega_{ss}$.

Performing the integration in Equation (4.24) renders

$$c'(\tau) = \frac{\sqrt{\pi}\sqrt{2\sigma_\omega}\, P_0}{2\pi} \exp\left[-\sigma_\omega^2\tau^2/2\right] = \frac{\sigma_\omega P_0}{\sqrt{2\pi}} \exp\left[-\sigma_\omega^2\tau^2/2\right] \tag{4.25}$$

The standard deviation σ_ω of the Doppler broadening of short wave reflectivity represents the inverse of the correlation time of the subresolution scattering elements (facets), namely, the finite scene coherence time.

$$\tau_c = \frac{1}{\sigma_\omega} \tag{4.26}$$

Substituting Equations (4.25) and (4.26) into Equation (4.21) yields

$$c(\mathbf{x}, t, \tau) = P_0' \exp\left[-\frac{\tau^2}{2\tau_c^2}\right] \exp\left[i\tau\left(\omega_{ss} + \frac{\partial \omega_{ss}}{\partial t} t\right)\right], \tag{4.27}$$

where $P_0' = \sigma_\omega P_0 (2\pi)^{-1/2}$ and $\tau = B/2V$.

The phase term in Equation (4.27) expresses the Doppler spread of the scattering element (facet) bandwidth, which is assumed to be the same for all facets. Thus

$$\left|\omega_{ss} + \frac{\partial \omega_{ss}\, t}{\partial t}\right| \approx O(\Delta\omega) = \frac{2\pi}{\tau_c} \tag{4.28}$$

Substituting Equation (4.28) into Equation (4.27) yields

$$c(\mathbf{x}, t, \tau) \approx P_0' \exp\left[-\frac{\tau^2}{2\tau_c}\right] \exp\left[\frac{i2\pi\tau}{\tau_c}\right] \tag{4.29}$$

Equation (4.29) represents explicitly the previously mentioned complex disturbance to INSAR remotely sensing the ocean surface. Substituting Equation (4.29) into Equation (4.17) yields the explicit expression of the cross-covariance of complex reflectivity for SAR interferometry.

$$\begin{aligned} \langle r_1(\mathbf{x}, t)\, r_2^*(\mathbf{x}, t, \Delta t)\rangle &= \sigma(\mathbf{x}, t) \exp\left[\frac{i2\pi\Delta t}{\tau_c}\right] \\ &\quad \cdot \exp\left[-\frac{\Delta t^2}{2\tau_c^2}\right] \exp\left[-2i\mathbf{k}\cdot\mathbf{U}_0(\mathbf{x}, t)\, \Delta t\right] \end{aligned} \tag{4.30}$$

where $\Delta t = B/2V$. Equation (4.30) illustrates the sensitivity in measuring the line of sight velocity component $\mathbf{U}_0$ of an unsteady rough ocean surface. It is shown that the key limiting parameter is the ratio between the inherent interferometric time delay ($\Delta t = B/2V$) and the scene coherence time τ_c which is analyzed next.

The first phase term in Equation (4.30) represents the additive phase noise to the mean surface velocity $\mathbf{U}_0$, which is attempted to be measured by INSAR. This noise term is required to be small relative to the mean phase term. This implies

$$|2\mathbf{k}\cdot\mathbf{U}_0\Delta t| \gg \left|\frac{2\pi\Delta t}{\tau_c}\right|, \tag{4.31}$$

which results in

$$\tau_c \gg \frac{\lambda}{2|\mathbf{U}_0|}. \tag{4.32}$$

For the NASA/JPL DC-8 airborne configuration, the range of measurable velocities $\mathbf{U}_0$ is ± 1.25 m/s and for the L-band radar wavelength of $\lambda = 24$ cm, Equation (4.32) indicates that the scene coherence time τ_c should be at least 0.1 sec for the additive phase noise term to be neglected. The known observed estimates of the scene coherence time for L-band radar are equal and smaller than the order of 10^2 msec (Lyzenga and Shuchman, 1983, Kasilingam and Shemdin, 1988).

Next to be examined is the attenuation of the radar cross-section caused by the slightly different time in imaging a given scene by the two physically separated INSAR antennas. This attenuation is represented by the second exponential in Equation (4.30). The radar cross-section for INSAR can be expressed as:

$$\sigma'(\mathbf{x}, t, \Delta t) = \sigma_0(\mathbf{x}, t) \exp(-\Delta t^2 / 2\tau_c^2) \tag{4.33}$$

In order to extract the phase information representing the surface velocity (last term on RHS of Equation (4.30)), one needs a sufficient signal $\sigma'(\mathbf{x}, t, \Delta t)$ above the noise level. A 3 dB attenuation of the cross-covariance 'signal' is allowed, ensuring accurate measurements of the backscattering surface velocity. The required scene coherence time τ_c in Equation (4.30) is taken to be

$$\tau_c \geq \frac{B}{2V} \frac{1}{(2 \ln 2)^{1/2}} \tag{4.34}$$

Once τ_c is known, the upper limit on $\Delta t = B/2V$ is defined, which in turn prescribes the necessary INSAR set up. Conversely, for a given INSAR set up the minimum allowable scene coherence time is determined. For the DC-8 INSAR configuration ($B = 19.8$ m, platform velocity $V \approx 200$ m/s), using criterion (4.34) yields the minimum required scene coherence time $\tau_c = 20$ msec. Combining the phase and

amplitude constraints on the radar scene coherence time, the temporal correlation of the short wave reflectivity should be substantially greater than 100 msec for the given INSAR system.

Finally, the model can estimate the range of variability of the complex reflectivity within the inherent INSAR measurement time, which will still allow the extraction of ocean surface resolvable motion with minimum contamination.

D. ESTIMATION OF SCENE COHERENCE TIME

The next step in the study is to estimate the actual scene coherence time for an L-band imaging radar using two different approaches:

- Theoretically, assuming the Pierson Moskowitz ocean spectrum.
- Experimentally, using for the first time simultaneously SAR and INSAR imaging records.

1. Estimation of Scene Coherence Time Based on Pierson-Moskowitz Spectrum

The finite scene coherence time may be one of the most important factors in constraining SAR's ability to image azimuthally traveling waves (see Section IV. B). In this section, the analysis will follow recent attempts to quantify this parameter (see e.g., Tucker, 1985b, Alpers and Bruening, 1986, Vachon et al., 1988) using the Pierson-Moskowitz ocean spectrum for fully arisen sea. Kasilingam and Shemdin (1988) point out the uncertainty in the validity of this approach, which might lead to differences by order of magnitudes in estimating the scene coherence time τ_c. Due to the complexity of the temporal ocean surface decorrelation τ_c, the theory associated with the ocean scattering motion effects is still under extensive research. Owing to the lack of experimental evidence and more profound theoretical understanding of the small scale roughness of the sea surface, this approach still remains acceptable.

The classical approach is to relate the azimuth image smear $\langle\delta(x)^2\rangle^{1/2}$ (which is inversely proportional to the scene coherence time), to the rms facet surface velocities $\langle \mathbf{U}'^2\rangle^{1/2}$ caused by the random material velocities of subresolution scale waves (see Equation 4.20).

$$\langle\delta(x)^2\rangle^{1/2} = \langle \mathbf{U}_r'^2\rangle^{1/2} R/V \tag{4.35}$$

where $\langle U_r'^2\rangle^{1/2}$ is the radial component of $\langle \mathbf{U}'^2\rangle^{1/2}$.

The shape of the Doppler broadening spectrum associated with the random facet velocities $\mathbf{U}_r'$ is assumed to be Gaussian (see Equation (4.22)), resulting in a SAR azimuthal imaging transfer function with a low-pass filter character. The bandwidth of this filter is inversely proportional to the decorrelation time scale, which is interpreted as the scene coherence time. In the wave number domain, the width of this filter (transfer function) is inversely proportional to the azimuthal image smear. It is important to note that the loss of resolution due to finite scene coherence time is not a defocusing effect, and is therefore not recoverable by focus adjustment in the processing or integration time setting (see Chapter III).

Based on the relation between the scene coherence time and rms surface velocity $\langle \mathbf{U}'^2\rangle^{1/2}$ spread, the subresolution velocity spread is first estimated. $\langle \mathbf{U}'^2\rangle^{1/2}$ may be computed by integrating the orbital velocity power spectrum between the appropriate wave frequencies

$$\langle \mathbf{U}_r'^2\rangle = \int_{\omega_1}^{\omega_2} \omega^2 \, S_\eta(\omega) \, f^2(\gamma) \, d\omega, \tag{4.36}$$

where $S_\eta(\omega)$ is the omnidirectional surface elevation frequency power spectrum and $f(\gamma)$ is the geometric function

$$f(\gamma) = \frac{1}{\pi}\int_{-\pi/2}^{\pi/2} (\sin^2\gamma \sin^2\phi + \cos^2\gamma)^{1/2} d\phi \tag{4.37}$$

where ϕ is the angle between the wave train and the aircraft attitude and γ is the incidence viewing angle (Figure 4.1). The geometric function $f(\gamma)$ represents the projection of the moving scene in the radial viewing direction. $f(\gamma)$ is always smaller than 1.

A rather crude assumption is next made about the ocean wave spectrum in calculating $\langle \mathbf{U}'^2 \rangle^{1/2}$, which is in fact sensitive to local sea conditions. In the absence of relevant experimental data, it is assumed that the ocean wave spectrum for a fully arisen sea can be described by a Pierson-Moskowitz spectrum (e.g., Alpers and Bruening, 1986, Tucker, 1985b). Substituting the Pierson-Moskowitz spectrum into Equation (4.36) yields:

$$\langle \mathbf{U}_r'^2 \rangle = \int_{\omega_1}^{\omega_2} w^2 \alpha g^2 \omega^{-5} \exp\left[-\beta (g/\mathbf{U}_\mathrm{w})^4\right] f^2(\gamma) d\omega \tag{4.38}$$

where $\alpha = 8.1 \times 10^{-3}$ is the Phillips constant, $\beta = 0.74$, and $\mathbf{U}_\mathrm{w}$ is the wind speed at a height of 19.5 m.

After integration,

$$\langle \mathbf{U}_r'^2 \rangle = \frac{\alpha}{4} \left(\frac{\pi}{\beta}\right)^{1/2} \mathbf{U}_\mathrm{w}^2 \operatorname{erf}\left[\mu\ (\mathbf{U}_\mathrm{w})^{-2}\right] f^2(\gamma)\Big|_{\omega_1}^{\omega_2} \tag{4.39}$$

with $\mu = (\beta)^{1/2} g^2 = 82.78\ \mathrm{m}^2\ \mathrm{sec}^{-2}$.

The lower limit of integration is associated with the shortest resolvable ocean wavelength $\mathcal{O}$ (10 m) and is determined by the Nyquist criterion. The upper limit is determined by the fundamental subresolution scattering elements (facet) with size of the order of Bragg wavelength ($\sim$ 0.2 m) which can be replaced for computational convenience by $\omega_2 \longrightarrow \infty$ with a small error.

The lower limit is controversial since the actual SAR (and INSAR) azimuth resolution is not known *a priori*, being a function of the scene coherence time. A few choices based on different physical considerations will be discussed

below. The lower integration limit ω_1 in Equation (4.39) is replaced by a cutoff resolvable wavelength L_1 using the dispersion relation for water waves,

$$\omega_1 = (2\pi g/L_1)^{1/2} \tag{4.40}$$

Since the shortest resolvable wavelength is O (10 m), the surface tension effects are neglected and only gravity waves are considered. By inserting the integration limits into Equation (4.39), it is found

$$\langle \mathbf{U}_r'^2 \rangle = \left(\frac{\alpha}{4}\right) \left(\frac{\pi}{\beta}\right)^{1/2} \mathbf{U}_w^2 \text{ erf } \left[\mu' \left(\frac{L_1}{\mathbf{U}_w^2}\right)\right] f^2(\gamma) \tag{4.41}$$

with $\mu' = \mu/g2\pi = 1.35$ m sec^{-2}. For strong winds $\mu' L_1/\mathbf{U}_w^2 \ll 1$, the radial velocity spread from Equation (4.41) simplifies to:

$$\langle \mathbf{U}_r'^2 \rangle^{1/2} = \left[\frac{\alpha}{4} \left(\frac{\pi}{\beta}\right)^{1/2} \mu' \, L_1\right] f(\gamma) \tag{4.42}$$

which is independent of the sea-state. For weak wind speeds $\mu' L_1/\mathbf{U}_w^2 \gg 1$ and Equation (4.41) simplifies to:

$$\langle \mathbf{U}_r'^2 \rangle^{1/2} = \left[\frac{\alpha}{4} \left(\frac{\pi}{\beta}\right)^{1/2}\right] \mathbf{U}_w \, f(\gamma) \tag{4.43}$$

Surprisingly, the rms velocity spread for weak winds, Equation (4.43), is independent of the cutoff wavelength L_1, which is determined in this case mainly by the SAR system. This wavelength represents the scale limit of waves which are treated deterministically ($L > L_1$) and waves which are treated statistically ($L < L_1$). This statistical region is of interest since the unresolved wave ($L < L_1$) modulate randomly the fundamental scattering elements. The temporal variability in the surface reflectivity is determined by the scene coherence time.

Two related choices for the cutoff wavelength L_1 have been considered. The first choice is based upon the processor coherent integration time for a wave

with a period equal to T. This wave and shorter waves will propagate at least one cycle over the time of image formation contributing only to the rms velocity. Using again the deep water dispersion relation for gravity waves, this cutoff scale is (Vachon et al., 1988):

$$L_1 = \frac{g}{2\pi} T^2 \tag{4.44}$$

The second choice used by some investigators (e.g., Alpers and Bruening, 1986, Tucker, 1985a) is $L_1 = 2\rho$, twice the matched filter processor resolution. For a moving ocean surface, the azimuth resolution is degraded and is practically unknown. It could be much larger than 2ρ, which is the nominal azimuth resolution for an unmoving scene. Noting that the mean Doppler broadening due to the velocity of the intermediate unresolvable waves is given by:

$$f_{dc} = \frac{2\langle \mathbf{U}_r'^2 \rangle^{1/2}}{\lambda} \tag{4.45}$$

leads to the finite radar scene coherence time

$$\tau_c = \frac{1}{f_{dc}}. \tag{4.46}$$

For strong wind ($\mathbf{U}_w \geq 10$ m/s) substituting Equation (4.44) into Equation (4.39) and the result into (4.45) and (4.46), yields the scene coherence time.

$$\tau_c = 5.04 \, \frac{\lambda}{T f(\gamma)} \tag{4.47}$$

and for $L_1 = 2\rho$

$$\tau_c = 4.45 \, \frac{\lambda}{(\rho)^{1/2} f(\gamma)} \tag{4.48}$$

For weak winds ($\mathbf{U}_w \leq 5$ m/s) substituting Equation (4.43) into Equation (4.45), (4.46) gives:

$$\tau_c = 7.74 \frac{\lambda}{\mathbf{U}_w \, f(\gamma)} \tag{4.49}$$

TABLE 4.1: Estimates for Scene Coherence Time as a Function of Wind Speed and Cutoff Wavelength for NASA/JPL DC-8 L-Band Radar with $f(\gamma) = 1$

Equation	L_1	$\mathbf{U_w}$ (m/sec)	τ_c (msec)
(4.47)[1]	$\frac{g}{2\pi}T^2$	≥ 10	600
(4.48)[2]	2ρ	≥ 10	610
(4.51)[3]			350

[1] $T = 2$ sec [2] $\rho = 3.03$ m [3] $H_s = 0.6$ m.

Since for fully developed wind seas, the wind speed $\mathbf{U_w}$ at the height of 19.5 m is related to the significant waveheight (mks units) by

$$\mathbf{U_w^2} = 47.4 H_s, \tag{4.50}$$

Equation (4.49) can be rewritten as

$$\tau_c = 1.12 \frac{\lambda}{\sqrt{H_s}\, f(\gamma)}. \tag{4.51}$$

The estimated values of the scene coherence time in Table 4.1 using Equations (4.47), (4.48), (4.51) and $f(\gamma) = 1$ are rather long compared to the sparse estimates based on observations in the literature (30–100 msec for L-band radar). The decrease in $f(\gamma)$ with increasing incidence angle will increase even more the scene coherence time τ_c as computed by the equations used in Table 4.1. The dependence of τ_c on the spreading function $f(\gamma)$ is illustrated in Figure 4.3. This dependence was not considered explicitly in other works and its importance rises from analysis of observed data (see Chapter VII).

Variability of several hundred msec in the estimates of coherence time scales is noted in Table 4.1. The first two estimates are computed using the DC-8

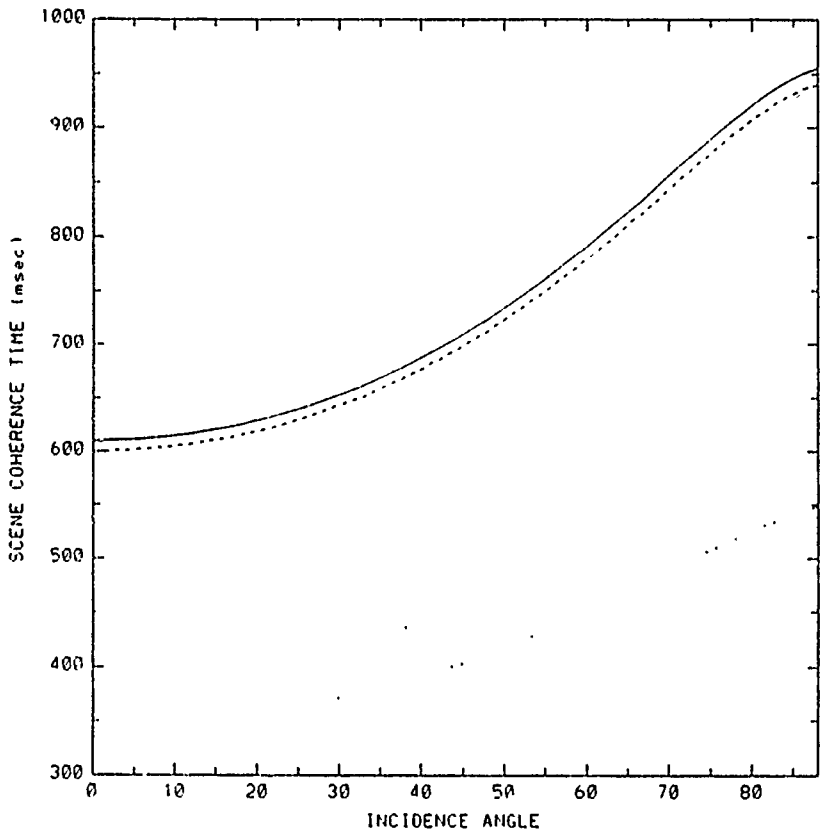

Figure 4.3: The effect of spreading function $f(\gamma)$ on the scene coherence time τ_c, showing the increase of the scene coherence time with incidence angle.

SAR parameters and are independent of sea state, a situation which seems to be unlikely. The third estimate seems to be more sensitive to the real ocean situation, namely, dependence of scene coherence time on sea state and hence wind speed. It will be shown through the experimental approach adopted in the next section that the shortest coherence time estimate of the present method is rather longer than that which is observed. This might indicate the inadequacy of the present approach to estimate the scene coherence time, mainly because of a lack of comprehensive understanding of short wave radar reflectivity (Hasselmann et al., 1985). To have a more reliable estimate of this parameter, it is crucial to obtain more direct measure-

ments of the coherence time which determines the effective azimuthal resolution of the SAR and hence INSAR imagery.

2. Estimation of Radar Scene Coherence Time Based on SAR and INSAR Simultaneous Images

The temporal coherence of the ocean scene can be investigated by using simultaneous SAR and INSAR records. As described in section B of this chapter, the image intensity of SAR is a map of the covariance of the complex reflectivity. The mean image intensity obtained by a single antenna is computed by ensemble averaging neighboring pixels, and is directly related to the covariance of complex reflectivity:

$$\langle r_1(\mathbf{x},t) r_1^*(\mathbf{x},t+\tau)\rangle = \sigma_1(\mathbf{x},t)\exp\left[-\tau^2/2\tau_c^2\right] \tag{4.52}$$

Similarly, for the second antenna separated physically by a distance B from the first antenna, the covariance of complex reflectivity is taken to be:

$$\langle r_2(\mathbf{x},t+\Delta t) r_2^*(\mathbf{x},t+\Delta t+\tau)\rangle = \sigma_2(\mathbf{x},t,\Delta t)\exp\left[-\tau^2/2\tau_c^2\right] \tag{4.53}$$

where $\Delta t = B/2V$ and σ is the radar cross section which represent the covariance of short wave reflectivity modulated mainly by long wave tilt. Since the temporal variations of these waves are slow compared to the interferometric time interval Δt, it is reasonable to assume that the radar cross-section does not vary during the time Δt. Therefore

$$\sigma_1(\mathbf{x},t) \simeq \sigma_2(\mathbf{x},t+\Delta t) \simeq \sigma(\mathbf{x},t) \tag{4.54}$$

When corresponding pixels from the two images are combined to extract the interference phase, the temporal cross-correlation between the corresponding pixel scattering elements introduces an additional cross-section modulation due to the random velocity spread of subresolution intermediate waves modulating the short wave reflectivity. This relatively fast time decorrelation of the scene in a given

time interval $\Delta t = B/2V$ attenuates the INSAR signal (see Equation (4.33)). The magnitude of the cross-product of the complex images is directly related to the cross-covariance of complex reflectivity, and is given by:

$$\langle r_1(\mathbf{x},t) r_2^*(\mathbf{x},t+\Delta t+\tau)\rangle = \sigma_{1,2}(\mathbf{x},t+\Delta t)\exp\left[-\tau^2/2\tau_c^2\right] \tag{4.55}$$

where

$$\sigma_{1,2}(\mathbf{x},t,\Delta t) = \sigma(\mathbf{x},t)\exp\left[-\Delta t^2/2\tau_c^2\right] \tag{4.56}$$

Substituting Equation (4.56) into Equation (4.55) yields:

$$\langle r_1(\mathbf{x},t) r_2^*(\mathbf{x},t+\Delta t+\tau)\rangle = \sigma(\mathbf{x},t)\exp\left[-\Delta t^2/2\tau_c^2\right]\exp\left[-\tau^2/2\tau_c^2\right] \tag{4.57}$$

Neglecting for a moment the additive noise effects, the effective radar cross-section obtained by INSAR (Equation 4.56) normalized to the product of the square root of both corresponding SAR radar cross-section by invoking Equation (4.54) yields

$$\begin{aligned} K &= \frac{\langle r_1(\mathbf{x},t) r_2^*(\mathbf{x},t+\Delta t)\rangle}{\langle r_1(\mathbf{x},t) r_1^*(\mathbf{x},t)\rangle^{1/2}\,\langle r_2(\mathbf{x},t) r_2^*(\mathbf{x},t)\rangle^{1/2}} \\ &= \exp\left[-\Delta t^2/2\tau_c^2\right] \end{aligned} \tag{4.58}$$

with

$$\Delta t = B/2V$$

Equation (4.58) expresses the ratio between the INSAR ocean surface cross-covariance of complex reflectivity and the two individual SAR covariance of complex reflectivities.

Coherent radars such as SAR are inherently subject to speckle or fading noise. By averaging neighboring pixels the speckle noise is reduced at the expense of nominal resolution. This operation is similar to the multiple look-operation, in

which the processor optimal (maximum) integration time is divided into shorter integration periods, and by averaging similar images with a time shift, the fading noise is reduced at the expense of resolution.

In the data analysis, relatively large identical areas ($> 10^3$ pixels) for the two SAR and INSAR intensity images were chosen for averaging. The noise power is reduced by:

$$S_n = \frac{\langle n^2 \rangle}{\sqrt{N}} \tag{4.59}$$

where N is the number of averaged pixels. The speckle and system noise are further reduced by normalizing the ratio K in Equation (4.58) by a similar ratio K_0 obtained from a stationary scene, like land, which fortunately was in the images. The scene coherency of land varies between fields with objects like plants and trees moving with the wind, and urban regions, which should be absolutely stationary and hence should ideally have infinite scene coherence time. Due to speckle noise and system errors the apparent coherency of urban regions is not infinite; thus normalizing K from Equation (4.58) with K_0 obtained from the urban regions of Marina, will further reduce the noise resulting in a better estimation of τ_c using this method. Based on this assumption, Equation (4.58) is modified to be:

$$K/K_0 = \exp[-\Delta t^2/2\tau_c^2] \tag{4.60}$$

and the scene coherence is taken to be

$$\tau_c = \frac{\Delta t}{\sqrt{-2\ln(K/K_0)}} \tag{4.61}$$

Equation (4.61) demonstrates the sensitivity of the scene coherence time estimation. A change in the ratio K/K_0 of 2% will change the estimation in the scene coherence time by almost 20% (see Figure 4.4). The estimates of τ_c using the above experimental method yields a more credible L-band scene coherence time O (100 msec),

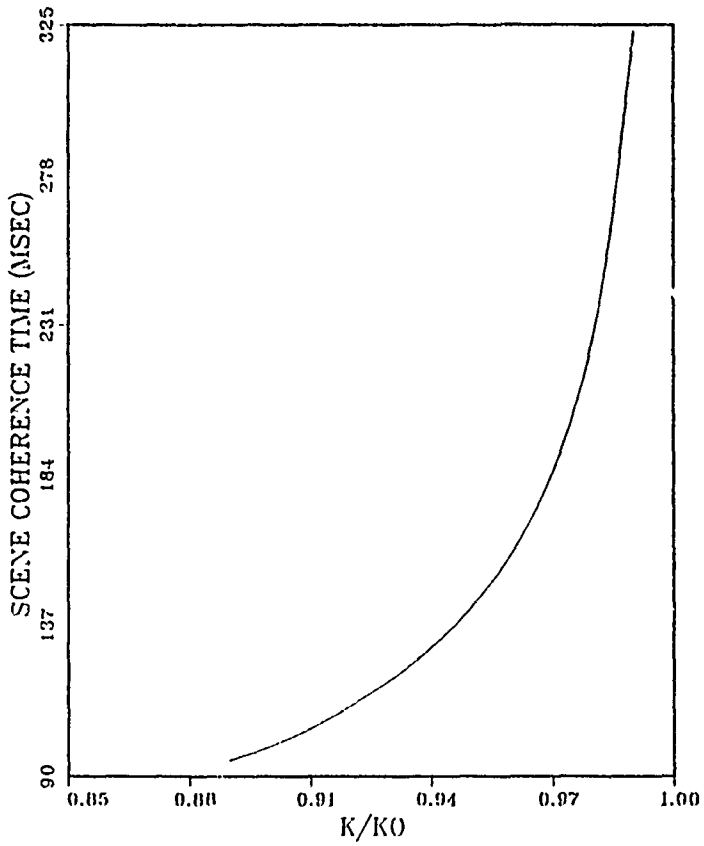

Figure 4.4: Dependence of scene coherence time on K/K_0.

which is consistent with the few earlier known estimates based on observations (e.g., Plant and Keller, 1983).

V. REFRACTION SHOALING AND DIRECTIONAL SPECTRA OF NEARSHORE OCEAN WAVES

A. INTRODUCTION

This chapter presents a brief review of linear ocean surface waves theory in shallow waters. A numerical refraction model (Dobson, 1967), followed by wave spectral analysis and measurement methods, are described. The behavior, analysis, and *in situ* observation of ocean surface waves are well developed subjects. However, many of the concepts presented are difficult to interpret in terms of coherent and noncoherent radar ocean surface imagery. The content of the present chapter is essential for interpretation of the experimental results and interdisciplinary understanding of the issues involved.

B. TRANSFORMATION OF NEARSHORE OCEAN WAVES

When waves propagate from deep to shallow water they are transformed as they begin to 'feel' the bottom. The transformation includes shoaling, refraction, diffraction, reflection, and dissipation. In the present analysis only shoaling and refraction phenomena are considered, since we ignore reflection (beach slope less than 1/20) and assume energy is conserved at steady state and is not translated lateraly along the wave crest (ignoring dissipation and difraction). The experimental site at Marina provides an opportunity to study wave refraction and shoaling as imaged by INSAR and ground truthed by a shallow water array off Marina.

1. Wave Refraction and Shoaling

Starting with the wave energy flux balance assuming an idealized situation in which wave energy is conserved at steady state and not transferred lateraly, yields the simplified energy flux equation:

$$\frac{\partial F_x}{\partial x} + \frac{\partial F_y}{\partial y} = 0 \tag{5.1}$$

where $\mathbf{F}(x, y)$ is the wave energy flux and is constant. Given a monochromatic deep water gravity wave field propagating shoreward as depicted in Figure 5.1, the following energy flux balance applies

$$E_0 Cg_0 b_0 = E_1 Cg_1 b_1 \tag{5.2}$$

where E_0, E_1 are wave energy Cg_0, Cg_1 are group velocities and b_0, b_1 are distances between wave rays in deep and shallow water respectively. We further discuss the derivation of a wave height relationship for shoaling waves from Equation (5.2) based on linear wave theory.

2. Refraction

Assuming the gravity waves are linear and dispersive yields the relationship.

$$\omega^2 = gk \tanh\ kh \tag{5.3}$$

where ω is the wave frequency, g is the acceleration of gravity, $k = 2\pi/L$ is the wavenumber magnitude (L is the wavelength) and h is the water depth. The group velocity for a surface gravity wave train is defined as

$$C_g = \frac{\partial \omega}{\partial k} \tag{5.4}$$

Substituting Equation (5.4) into Equation (5.3) yields the group wave velocity for gravity waves

$$C_g = \frac{C}{2}\left(1 + \frac{2kh}{\sinh\ 2kh}\right) \tag{5.5}$$

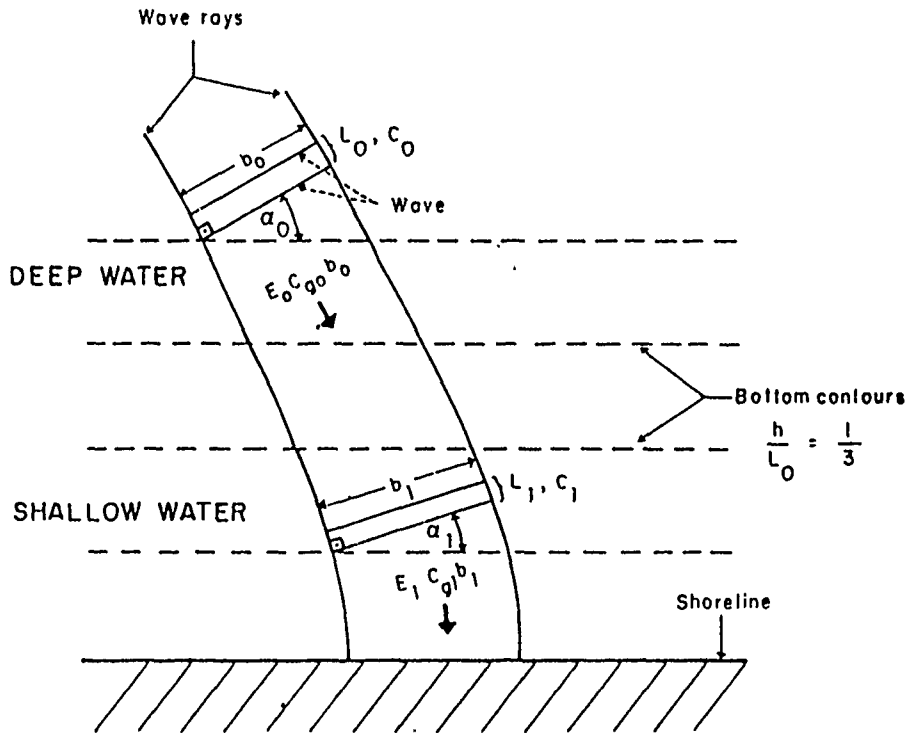

Figure 5.1: Wave refraction and shoaling.

where C is the wave phase velocity.

The instantaneous surface elevation of a monochromatic wave is given by:

$$\eta(x,t) = a\sin(\mathbf{k}\cdot\mathbf{x} - \omega t) \tag{5.6}$$

where a is the wave amplitude and $\mathbf{x} = (x, y)$ is the position vector. The variance of this wave is

$$\sigma_\eta^2 = \frac{1}{L}\int_0^L \left(\eta(\mathbf{x},t) - \overline{\eta(\mathbf{x},t)}\right)^2 d\mathbf{x} = \frac{a^2}{2} \tag{5.7}$$

where L is the ocean wavelength. Therefore the energy of a monochromatic wave in an irrotational and incompressible fluid given by:

$$E = \frac{1}{2}\,\rho g a^2 = \frac{1}{8}\,\rho g H^2 \tag{5.8}$$

where $H = 2a$ is the wave height.

Substituting Equation (5.8) into Equation (5.2) yields the wave height variation equation for shoaling waves (Mei, 1980)

$$H = H_0 \left[\frac{Cg_0}{Cg}\right]^{1/2} \left[\frac{b_0}{b}\right]^{1/2} = H_0\ k_s\ k_R \tag{5.9}$$

where k_s is the shoaling coefficient

$$k_s = \left[\frac{Cg_0}{Cg}\right]^{1/2} \tag{5.10}$$

and k_R is the refraction coefficient

$$k_R = \left[\frac{b_0}{b}\right]^{1/2}. \tag{5.11}$$

Within the limits of linear wave theory, the wave frequency ω must remain constant as waves propagate from deep water ashore. Using this approximation in the dispersion relationship rewritten in a wavelength form results in

$$L_1\ tgh\left(\frac{2\pi h_0}{l_0}\right) = L_0\ tgh\left(\frac{2\pi h_1}{L_1}\right) \tag{5.12}$$

Equation (5.12) illustrates the variation in wave length with depth for shoaling waves to preserve the invariant wave frequency. For deep water waves

$$\frac{2\pi h_0}{L_0} \longrightarrow \infty \tag{5.13}$$

and Equation (5.13) can be rewritten as (Shuchman and Kasischke, 1981)

$$L_1 = L_0\ tgh\ \left(\frac{2\pi h_1}{L_1}\right) \tag{5.14}$$

For straight and parallel of bathymetric contours, a simplified refraction formula based on Snell's low can be stated as:

$$C_1 = C_0\ \frac{\sin\alpha_1}{\sin\alpha_0} \tag{5.15}$$

where $C = \omega/k$ is the wave phase speed. Using Equation (5.3) to compute the phase speed and substituting the result in Equation (5.15) results in the refraction angle α between the wave rays and bottom contours for waves propagating from deep to shallow water

$$\alpha_1 = \sin^{-1}\left[\sin\alpha_0 \tan h\left(\frac{2\pi h_1}{L_1}\right)\right] \tag{5.16}$$

In the data analysis described in Chapter VII, the shoaling effect is estimated by using Equations (5.12) and (5.14), and the refraction effect is estimated using Equation (5.16) for straight and parallel contours only. An attempt to estimate refraction and shoaling of coastal gravity waves using SEASAT SAR data was done by Shuchman and Kasischke (1975). The method presented in this study is seen to be more accurate.

3. The Ray Trace Model

For complex bathymetric contours which are not straight and parallel to the shoreline, a linear numerical refraction and shoaling model by Dobson (1967) is used in our analysis. Following the approach established by Munk (1952) on wave refraction, Dobson developed a linear refraction model using the characteristics of the propagation of curving wave rays. Considering the geometry illustrated in Figure 5.2 the ray curvature equation in Cartesian coordinates is given by:

$$R(x,y,t) = \frac{1}{C(x,y)}\left[\sin\alpha(t)\,\frac{\partial C(x,y)}{\partial x} - \cos\alpha(t)\,\frac{\partial C(x,y)}{\partial y}\right] \tag{5.17}$$

and the ray separation factor β is stated by Dobson to be:

$$\frac{d^2\beta}{dt^2} + p(t)\,\frac{d\beta}{dt} + q(t)\beta = 0 \tag{5.18}$$

with

$$p(x,y,t) = 2\left[\cos\alpha\,\frac{\partial C(x,y)}{\partial x} + \sin\alpha\,\frac{\partial C(x,y)}{\partial y}\right] \tag{5.19}$$

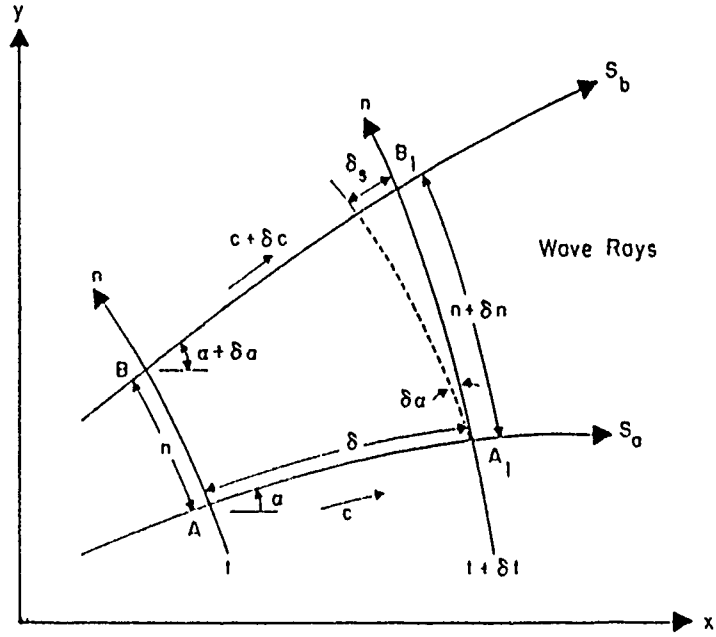

Figure 5.2: Refraction geometry and notation for Dobson's model.

$$q(x,y,t) = C(x,y)\left[\sin^2\alpha\,\frac{\partial^2 C(x,y)}{\partial x^2} - 2\sin\alpha\cos\alpha\,\frac{\partial^2 C(x,y)}{\partial x dy} + \cos^2\alpha\,\frac{\partial^2 C(x,y)}{\partial y^2}\right] \tag{5.20}$$

The wave ray path defined by R and α is computed with Equations (17)–(20), provided the wave phase speed $C(x,y)$ is known. $C(x,y)$ is constructed grid to grid over the ocean bathymetry as propagating to the required position. For more details of this method see reference (Dobson, 1967).

In this study, the bathymetry used in Dobson's refraction model is based on data collected originally by NOAA and projected onto a six second (lat, long) Modified Universal Transverse Mercator (UTM) grid. The data was screened and interpolated using linear triangulation to fill missing points onto a 200 meter rectangular grid (Kalid, 1989).

C. OBSERVATION METHODS OF OCEAN WAVE SPECTRA

The relation between the distribution of energy in sea surface waves and the direction of propagation is of great interest from the forecasting point of view and the understanding the generation processes. For the case presented in this study, shoaling wave transformations such as diffraction , refraction and reflection (see next section) are greatly influenced by the directional spectral characteristics of the waves. However, measurements of directional wave spectra requires greater effort than that of frequency power spectra. While the latter can be obtained from a wave record at a single point, the former requires simultaneous recording of several wave components.

The measuring techniques which are known to be applied can be classified into two categories (Goda, 1985)

1) *In situ* measurement method

- Wave gauge array
- Directional buoy
- Two axis current meter

2) Remote sensing method

- Optical technique (sterophotogrametry, holography)
- Microwave technique

In Chapter VII, frequency and directional spectra obtained from a wave gauge array are compared with two-dimensional wavenumber spectra obtained by a remote sensing interferometric SAR. Therefore, in the present section a synopsis of the basic

theoretical and observational background of direct and remote sensing methods are described.

1. Ocean Surface Wave Field Spectra

The characteristics of wave field properties can be determined from the observed sea surface elevation and the irrotational surface velocity. From linear wave theory there is a direct relationship between the sea surface elevation, velocity and pressure spectrum. The horizontal component of the wave orbital velocity can be described by a product of the ocean surface elevation $\eta(\mathbf{x}, t)$ and a transfer function $H_u(\omega)$:

$$u(t) = H_u(\omega)\ \eta(\mathbf{x}, t) \tag{5.21}$$

where

$$\eta(\mathbf{x}, t) = a\ \cos(\mathbf{k} \cdot \mathbf{x} - \omega t) \tag{5.22}$$

and

$$H_u(\omega) = \omega\ \frac{\cosh\ k(h+z)}{\sinh\ kh}, \tag{5.23}$$

where z is the depth of observation. The wave amplitude a is assumed to be small compared with wavelength and depth of water as required by linear theory. Similarly, the vertical velocity component is given by

$$\mathrm{w}(t) = H_{\mathrm{w}}(\omega)\ \eta(\mathbf{x}, t) \tag{5.24}$$

where

$$H_{\mathrm{w}}(\omega) = -i\omega\ \frac{\sinh\ k(h+z)}{\sinh\ kh} \tag{5.25}$$

The pressure wave form at depth z is taken to be

$$P(t) = H_P(\omega)\ \eta(\mathbf{x}, t) \tag{5.26}$$

where

$$H_P(\omega) = \rho g\ \frac{\cosh\ k(h+z)}{\cosh\ kh} \tag{5.27}$$

In the direct method, time series records are acquired from the random ocean processes. Assuming a stationary ocean surface, the classical analysis approach is the spectral technique, i.e., linear superposition of an infinite number of sinusoidal components with small amplitude and slope. Considering the water column as a constant parameter linear system, the input-output frequency is invariant. For input surface elevation spectra, Equations (5.21), (5.24), and (5.26) can be expressed in terms of input output power spectra related by the corresponding linear frequency invariant transfer function $H(\omega)$:

$$S_{out}(\omega) = |H(\omega)|^2 S_\eta(\omega) \tag{5.28}$$

Equation (5.28) reflects the fundamental idea of measuring the ocean wave frequency power spectra. The random sea surface elevation is considered as the input and the pressure or velocities as output. Next we discuss relevant statistical characteristics of the sea surface elevation related to the ocean wave spectra.

The random ocean surface is characterized by the autocovariance, $\rho(\mathbf{r}, \tau)$, of the surface displacement, η as:

$$\rho(\mathbf{r}, \tau) = \langle \eta(\mathbf{x}, t)\ \eta(\mathbf{x}, \tau + \mathbf{r}, t + \tau) \rangle \tag{5.29}$$

where $\mathbf{r}$ is the displacement vector.

The ensemble average of the autocovariance surface elevation in Equation (5.29) defines the decorrelation time and space scales of the sea surface. The Wiener-Khinchin theorem states that for any ergodic stationary random process (e.g., $\eta(\mathbf{x}, \tau)$) with zero mean, the wavenumber-frequency spectrum is given by the Fourier transform of the autocovariance function $\rho(\mathbf{r}, \tau)$ of the random process $\eta(\mathbf{x}, \tau)$.

$$S(\mathbf{k}, \omega) = \frac{1}{(2\pi)^3} \int\int \rho(\mathbf{r}, \tau)\ \exp\left[-i(\mathbf{k} \cdot \mathbf{r} - \omega\tau)\right] d\mathbf{r}\ d\tau \tag{5.30}$$

with the inverse Fourier transform

$$\rho(\mathrm{r},\tau) = \int\int S(\mathrm{k},\omega)\ \exp\Big[i(\mathrm{k}\cdot\mathrm{r} - \omega\tau)\Big] d\mathrm{k}\ d\omega \tag{5.31}$$

The mean square of surface elevation $\langle\eta^2(\mathrm{r},\tau)\rangle$ is obtained from Equation (5.30) for $\tau = 0$ and $\mathrm{r} = 0$. This variance term is proportional to the wave energy.

Under the above approximations the Fourier transform of the autocovariance of the surface elevation is computed as a function of wavenumber and frequency, with position and time as parameters.

2. Relation to Measurement Methods

The computation of the frequency wavenumber spectra requires simultaneous measurements of surface displacement in space and time. This requires an array of wave sensors and an enormous data processing effort. The omni-directional frequency spectrum is obtained with less effort and therefore more common, since it requires only a single wave sensor at a point, collecting temporal data with no spatial information about the wave field. At a given position $\mathrm{r} = 0$, the frequency spectra is given by

$$S(\omega) = \int S(\mathrm{k},\omega)\ d\mathrm{k} = \frac{1}{2\pi}\int \rho(0,\tau)\ \exp[i\omega\tau]d\tau \tag{5.32}$$

Since only positive circular frequencies have physical meaning and $S(\omega)$ is symmetric about $\omega = 0$, Equation (5.32) can be rewritten as:

$$S(\omega) = \frac{1}{\pi}\int_0^{+\infty} \rho(\tau)\ \cos\omega\tau\ d\tau \tag{5.33}$$

Since the total energy for a given sea state is unique, the integration areas of the frequency and wavenumber spectra are related by the Jacobian, yielding the unidirectional wavenumber spectrum

$$S(k) = \frac{\partial\omega}{\partial k}\ S(\omega) \tag{5.34}$$

where $k = |\mathbf{k}|$ and $d\omega/dk = C_g$ the group wave velocity. Using the linear dispersion relation $\omega = \omega(k)$ in computing $C_g, S(k)$ is obtained. This transformation can not be used in the high wavenumber, short waves part of the spectrum, since the intrinsic frequency of the shortest waves $\omega_0(k)$ are Doppler shifted due to modulation by the underlying dominant waves and/or currents on which the short waves are borne. Therefore the circular frequency of the short waves is given by

$$\omega(k) = \omega_0(k) + \mathbf{k} \cdot (\mathbf{U}_{OB}(x,t) + \mathbf{U}_{CR}(x,t)) \tag{5.35}$$

where $\mathbf{U}_{OB}(x,t)$ is the slowly varying orbital velocity and $\mathbf{U}_{CR}(x,t)$ could be any underlying varying currents. Equation (5.35) illustrates the nonuniqueness of the relationship between frequency and wavenumber.

For high resolution microwave radar sensors the backscattering energy is determined by the short scale (cm) surface roughness which is borne on an advecting surface. Equation (5.35) replaces the linear dispersion relationship between frequency and wavenumber (Equation (5.3)).

3. Wave Directional Spectrum

As noted in the literature review (Equation (2.7)) the normalized radar cross-section σ_0 is directly proportional to the two dimensional wavenumber spectrum.

$$\psi(\mathbf{k}) = \int S(\mathbf{k},\omega) d\omega \tag{5.36}$$

The instantaneous autocovariance can be expressed as:

$$\rho(\mathbf{r},0) = \int\int \psi(\mathbf{k} \ \exp\left[-i(\mathbf{k}\cdot\mathbf{r})\right] d\mathbf{k} \tag{5.37}$$

and inversely

$$\psi(\mathbf{k}) = \frac{1}{(2\pi)^2} \int \rho(\mathbf{r}) \ \exp\left[i(\mathbf{k}\cdot r)\right] d\mathbf{r} \tag{5.38}$$

To obtain $\psi(\mathbf{k})$, one needs spatial observations of the surface elevation autocovariance (Equation (5.38)). Attempts to measure this phenomena are still under extensive research using remote sensing techniques such as sterophotogrametry (Shemdin, et al., 1988) laser optics (Keller and Gotwols, 1983) or Doppler radars (Plant and Keller, 1983).

The two-dimensional wavenumber spectrum is also claimed to be computed from SAR images. However, there is still doubt about the precise mechanisms whereby waves are imaged by SAR. Therefore, the question remains whether the SAR image intensity spectrum bears much resemblance to the directional wave spectrum. In this study, a new approach is suggested for obtaining a two-dimensional wavenumber spectrum using interferometric SAR imagery. This method has a clearly observed imaging mechanism based on the measurement of the varying orbital velocity $U_{OB}(x,t)$ of the dominant surface ocean waves. The two-dimensional wave number spectrum of INSAR's phase image represents the spatial distribution of the surface velocity power in the viewing direction. In describing this spectrum, assume for the moment a monochromatic dominant wave oriented at an arbitrary angle ϕ relative to the flight direction (see Figure 4.1) and an incidence viewing angle γ. The surface elevation of this wave as seen by the imaging platform is given by:

$$\eta(\mathbf{x},t) = a\ g(\gamma,\phi)\ \cos(\mathbf{k}\cdot\mathbf{x} - \omega t) \tag{5.39}$$

where a is the wave amplitude and

$$g(\gamma,\phi) = (\cos^2\gamma + \sin^2\gamma\sin^2\phi)^{1/2} \tag{5.40}$$

After removing the current and phase velocities, the residual imaged radial velocity component U_{OB_r} can be computed. Using deep water linear wave

theory

$$U_{OBr}(\mathbf{x}) = \frac{\partial \eta(\mathbf{x})}{\partial t} = a\ \omega\ g(r,\phi)\ \sin(\mathbf{k}\cdot\mathbf{x} - \omega t) \tag{5.41}$$

Then the two-dimensional wavenumber spectra for the orbital velocity is

$$\psi_{U_{OBr}}(k_x, k_y) = \frac{1}{L^2}\int_{-L/2}^{+L/2}\int_{-L/2}^{+L/2} U_{OBr}(x,y)\ \exp[-i(k_x x + k_y y)]\ dxdy \tag{5.42}$$

The spectrum described in Equation (5.42) is tested against directional spectra obtained from a wave pressure array. A synopsis review on the theory of *in situ* measurement of directional spectra is described next.

Longuet-Higgins, Cartwright and Smith (1963) developed a directional wave bouy based on measuring the angles of pitch and roll and the heaving acceleration of the ocean surface. The heave is directly related to the surface elevation, while the pitch and roll are related to the two horizontal orthogonal components of wave surface slope namely, $\partial\eta/\partial x$, $\partial\eta/\partial y$. The directional spectrum $S(f,\theta)$ can be expressed as a product of the one-dimensional frequency power spectrum $S(f)$ and an angular spreading function $D(f,\alpha)$

$$S(f,\alpha) = S(f)\ D(f,\alpha) \tag{5.43}$$

where α is the wave direction. $D(f,\alpha)$ is associated with the distribution of energy in the frequency power spectrum, over direction and has a unit area over direction,

$$\int_0^{2\pi} D(f,\alpha)\ d\alpha = 1 \tag{5.44}$$

An objective of measurements is to determine the characteristics and criteria in selecting $D(f,\alpha)$ which most closely match the observed angular distribution of wave energy density. Using the most common *in situ* measurement technique - a floating buoy or slope array of four sensors in a square, one has to address their limited spatial capabilities in defining directionality, namely $D(f,\alpha)$.

Following Longuet-Higgins et al. (1963), the directional spreading function $D(f,\alpha)$ can be expanded as a Fourier series:

$$D(f,\alpha) = \frac{1}{\pi}\left(\frac{1}{2} + \sum_{n=1}^{\infty}[a_n \cos(n\alpha_n) + b_n \sin(n\alpha_n)]\right) \tag{5.45}$$

For the previously discussed bouys or slope arrays which measure only the surface slope and displacement, only the first two harmonics can be estimated. The horizontal sea surface slopes are obtained by taking the corresponding spatial derivative of the sea surface elevation (Equation 5.6)

$$\eta_x(t) = \frac{\partial \eta(t)}{\partial x} = (-ik\cos\alpha)\ \eta(t) = H_x(f)\ \eta(t) \tag{5.46}$$

$$\eta_y(t) = \frac{\partial \eta(t)}{\partial y} = (-ik\cos\alpha) = H_y(f)\ \eta(t) \tag{5.47}$$

Five Fourier coefficients can be determined from the $co(C)$ and quad (Q) spectra of the surface elevation and surface slope. The spectrum of $\eta_x(t)$ is given as

$$C_{\eta_x\eta_x}(f) = \int_0^{2\pi} |H_x(f)|^2 S(f,\alpha) d\alpha \tag{5.48}$$

Substituting Equations (5.43), (5.46) into Equation (5.48) yields

$$S_{\eta_x\eta_x}(f) = \int_0^{2\pi} k^2\cos^2\alpha S(f) D(f,\alpha)\ d\alpha = k^2 S(f)\int_0^{2\pi}\cos^2\alpha D(f,\alpha)\ d\alpha \tag{5.49}$$

Similarly the rest of cross-spectral quantities are obtained

$$C_{\eta_y\eta_y}(f) = k^2 S(f)\int_0^{2\pi}\sin^2\alpha\ D(f,\alpha)\ d\alpha \tag{5.50}$$

$$C_{\eta\eta}(f) = S(f)\int_0^{2\pi} D(f,\alpha)\ d\alpha = S(f) \tag{5.51}$$

$$C_{\eta_x\eta_y}(f) = k^2 S(f)\int_0^{2\pi}\cos\alpha\ \sin\alpha D(f,\alpha)\ d\alpha \tag{5.52}$$

$$Q_{\eta\eta_x}(f) = kS(f)\int_0^{2\pi}\cos\alpha\ D(f,\alpha)\ d\alpha \tag{5.53}$$

$$Q_{\eta\eta_y}(f) = kS(f)\int_0^{2\pi}\sin\alpha\ D(f,\alpha)\ d\alpha \tag{5.54}$$

From Equations (5.49)-(5.54) Longuet-Higgins et al. (1963) computed the Fourier coefficients of $D(f,\alpha)$ as follows:

$$a_0 = \frac{1}{\pi}\int_0^{2\pi} D(f,\alpha)\, d\alpha = \frac{1}{\pi} \tag{5.55}$$

$$a_1 = \frac{1}{\pi}\int_0^{2\pi} D(f,\alpha)\, \cos\alpha\, d\alpha = \frac{1}{\pi k}\, Q_{\eta\eta_x}(f) \tag{5.56}$$

$$b_1 = \frac{1}{\pi}\int_0^{2\pi} D(f,\alpha)\, \sin\alpha\, d\alpha = \frac{1}{\pi k}\, Q_{\eta\eta_y}(f) \tag{5.57}$$

$$a_2 = \frac{1}{\pi}\int_0^{2\pi} D(f,\alpha)\, \cos 2\alpha\, d\alpha = \frac{1}{\pi k^2}\, (C_{\eta_x\eta_x}(f) - C_{\eta_y\eta_y}(f)) \tag{5.58}$$

$$b_2 = \frac{1}{\pi}\int_0^{2\pi} D(f,\alpha)\, \sin 2\alpha\, d\alpha = \frac{2}{\pi k^2}\, C_{\eta_x\eta_y}(f) \tag{5.59}$$

Longuet-Higgins et al. (1963) used these five Fourier coefficients to describe an assumed cosine bell angular energy distribution function. This method can only describe a unimodal energy distribution with limited resolution, which is frequently not realistic. These coefficients can be represented by an infinite number of angular spreading functions. It is therefore desirable to seek a technique (if possible) to match the coefficients obtained from the data to a more realistic angular distribution function.

Grauzinis (1990) improved the Longuet-Higgins et al. (1963) method in matching analytically a more realistic angular distribution function $D(\alpha)$ to the obtained Fourier coefficients. The technique is based on representing the Fourier coefficients of $D(\alpha)$ as the superposition of a weighted sum of symmetric unit area density functions oriented at different direction

$$a_k + ib_k = \sum_j \mathrm{w}_j\, m_k(j)\, \exp(jk\beta_j) \tag{5.60}$$

where w_j is the weighting parameter, m_k is the canonical coefficient of the even unity spreading function and β_j is the angular orientation of component j. For a typical pressure array (four sensors) or pitch and roll buoy, the obtained cross spectral wave

quantities result in the Fourier coefficients of Equation (5.60) through the second order and are taken to be

$$a_1 + ib_1 = m_1\left[\mathrm{w}_1 \exp(i\beta_1) + \mathrm{w}_2 \exp(i\beta_2)\right] \tag{5.61}$$

$$a_2 + ib_2 = m_2\left[\mathrm{w}_1 \exp(i2\beta_1) + \mathrm{w}_2 \exp(i2\beta_2)\right] \tag{5.62}$$

To solve the system represented by Equations (5.61), (5.62), further assumptions have to be made. The most sufficient assumption made by Grauzinis (1990) is that the two canonical coefficients are related by a power law r

$$m_2 = m_1^r \tag{5.63}$$

where r defines the broadening (r increase) or the sharpness (r decrease) of the distribution function defined initially by the canonical coefficients. For a unimodal wave field and $m = 0.9$ and $r = 4$, the half power distribution is 12 degrees, which is about one third of the Longuet-Higgins et al. (1963) cosine bell resolution. The improvement of this technique relative to the Longuet-Higgins et al. (1963) method is the variability in the sharpness of the model distribution function, which enables it to be matched with better directionality to the observed energy distribution function. Also, Equations (5.61), (5.62) introduce two distributions of wave energy with different orientations and weights. This allows the model to represent a bimodal wave system which is not possible by the Longuet-Higgins et al. (1963) method.

This exact method of matching the Fourier coefficients to a wave spreading function is not unique. The question that remains is how to optimize the selection of the distribution that best matches the real data. Cartwright (1963) suggests that a criteria to improve the selection of the distribution function can be obtained from the ratio of the magnitude of the Fourier coeffients. Grauzinis (1990) further suggests a beam separation index criteria to indicate the best distribution function

fitting. This criteria aids the selection of the canonical coefficients which fulfills the analytic solution to give zero beam separation from the required distribution. For different r's, the bimodal distribution with the minimum peak separation is selected as the best fit. Despite the analytical efforts to improve the directional resolving wave power obtained from pitch and roll buoys or pressure/current limited arrays, an rms resolution of 4–6 degrees appears to be the best that can be achieved using this method.

VI. THE MONTEREY BAY WAVE FIELD AND CURRENTS '89 REMOTE SENSING EXPERIMENT

A. INTRODUCTION

The primary objective of the experimental part of this study is to verify the feasibility of an airborne INSAR method to reliably spatially sense ocean surface wave and current fields. The verification is done by comparing the results of this unique technique with simultaneous *in situ* conventional temporal and local spatial measurements including directional wave spectra from an array, local wind and surface drifters measurements. To simplify the interpretations, the time of the year and the site of the experiment were selected so as to provide near linear conditions of wave imaging (narrow band wave spectrum of low to moderate variance) and a moderate sloping beach (approximately 20 m/km) allowing sufficient locally homogeneous conditions for linear spectral analysis.

The relatively shallow water provides an opportunity to study for the first time wave refraction and shoaling using INSAR. Four partially overlaped areas ($\sim$ 12 km $\times$ 6 km) were imaged by INSAR from four different directions centered on the shallow water wave array off Marina. Results from three legs are reported in this study.

Overall, three field tests were performed in the vicinity of Monterey Bay:

- On June 1, 1989, several prototypes of passive radar drifters were tested at sea to measure ocean surface currents using Lagrangian bouys. The drifters were designed and built at the Naval PostGraduate School and were tested

from the Research Vessel (R/V) Ricketts in the vicinity of Moss Landing (see Appendix C).

- On July 23–24, 1989, a preliminary coordinated simultaneous airborne and ground truthing experiment was performed. The experimental scene was centered on the wave and wind stress NDBC pitch and roll buoy off Monterey Bay (see Figure 6.2). NASA/JPL DC-8 radar overflights were conducted on July 24, 1989 between 1000 and 1040 Pacific Day Time (PDT). The R/V Point Sur on a cruise from 232200 to 242400 July 1989 acquired ground truthing data for comparison with the following near ocean surface phenomena:

  - Vertical profile of current vectors within the mixed layer measured by Acoustic Doppler Current Profile (ADCP).
  - Surface currents sensed by Lagrangian floating buoys which were positioned by Loran-C and Mini-Ranger navigation systems (see Section E4).
  - Wind speed and direction which generates the short ocean surface wave field patterns responsible for the resonant radar backscatter (Bragg waves).
  - Vertical density gradients at the depth between 10 and 250 m measured by Conductivity Temperature Depth (CTD), which might affect surface dynamical processes.

Wind stress and dominant wave time series records were acquired from the NOAA pitch and roll buoy. Unfortunately, the Interferromatric SAR images could not be obtained from this experiment. An error in setting up the fore and aft radar antennas with different polarizations (vertical and horizontal), instead of being identical (both vertical or horizontal), prevented fringes formation essential for creating an interferogram.

Based on these preliminary experiments, the experimental plan was modified for a following experiment. The field test site was moved to an area close to the shore to include stationary land in the INSAR imaging scene to assist aircraft attitude corrections in addition to the aircraft Inertial Navigation System (INS) (see Chapter III). A second modification was to replace the passive radar drifters with thin floating plywood sheets (see section F3) to minimize windage effects. The following and final experiment for this study was carried out on September 8, 1989 in Monterey Bay centered on the shallow water wave array off Marina Beach. An illustration of the July and September experimental scenarios is depicted in Figure 6.1. A detailed description of the Marina experimental site is given in section B, followed by a description of the Marina experiment in section C. The environmental conditions for the experiment are given in section D.

B. THE EXPERIMENTAL SITE

The Monterey Bay is characterized by variable bathymetric features including the largest submarine canyon in the western hemisphere bisecting the Bay (Figure 6.2). These bottom features cause substantial perturbations on the near shore wave fields and tidal currents. The experimental site for data acquired during this study is in the nearshore region of Marina within Monterey Bay. This region is shadowed by Point Santa Cruz in the northwest and Point Pinos in the southwest.

The Marina site was selected because of the location of a wave array for ground truthing and the required inclusions of land in the scene. Also, the site has a relatively continuous, though moderate, alongshore bottom slope (about 20 m/km) resulting in a relatively small but sufficient region of locally homogeneous bathymetry. This fact constrained the spectral analysis to be applied to small

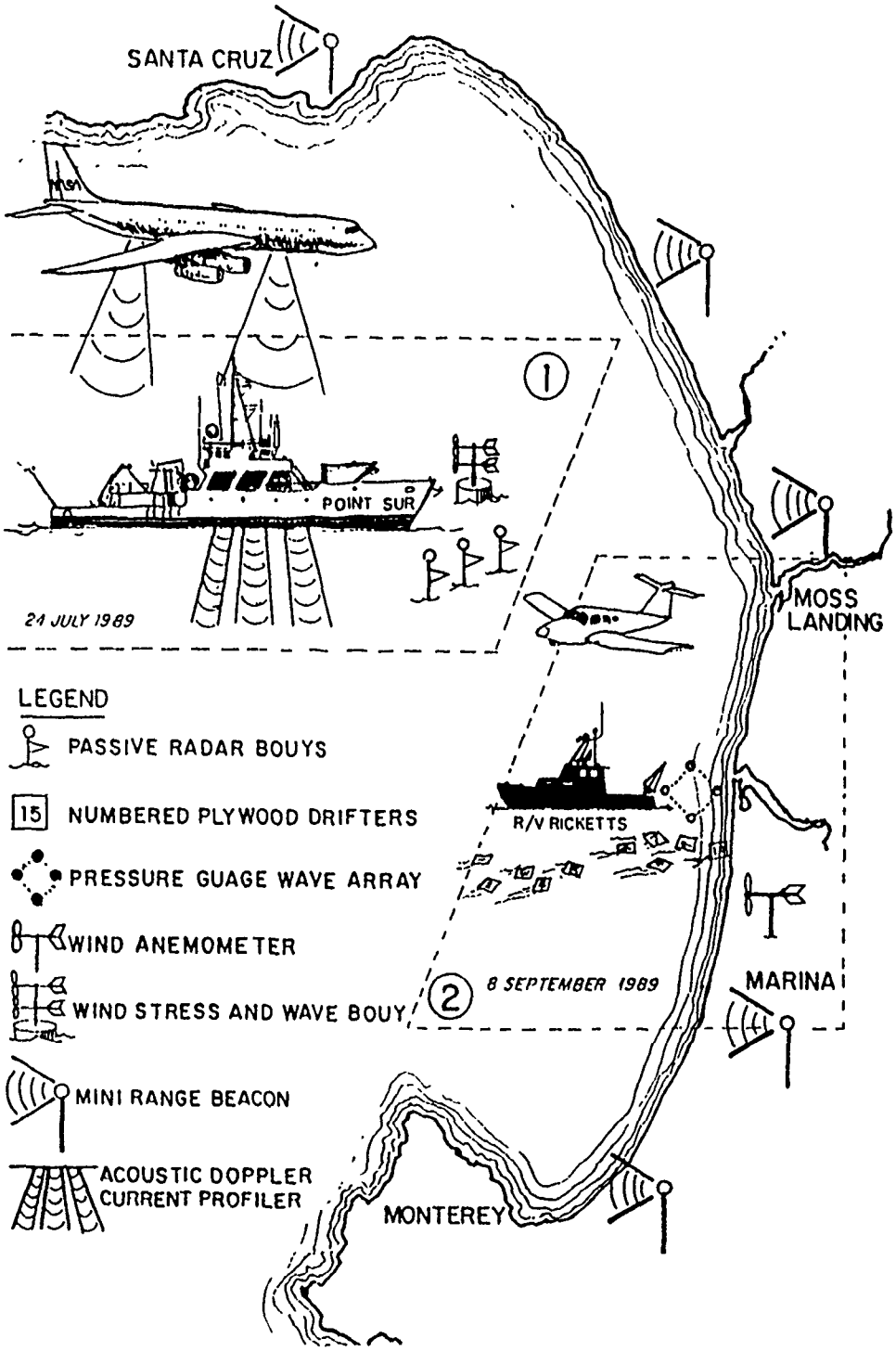

Figure 6.1: An artistic illustration of experiment scenario conducted on July 24 and September 8, 1989.

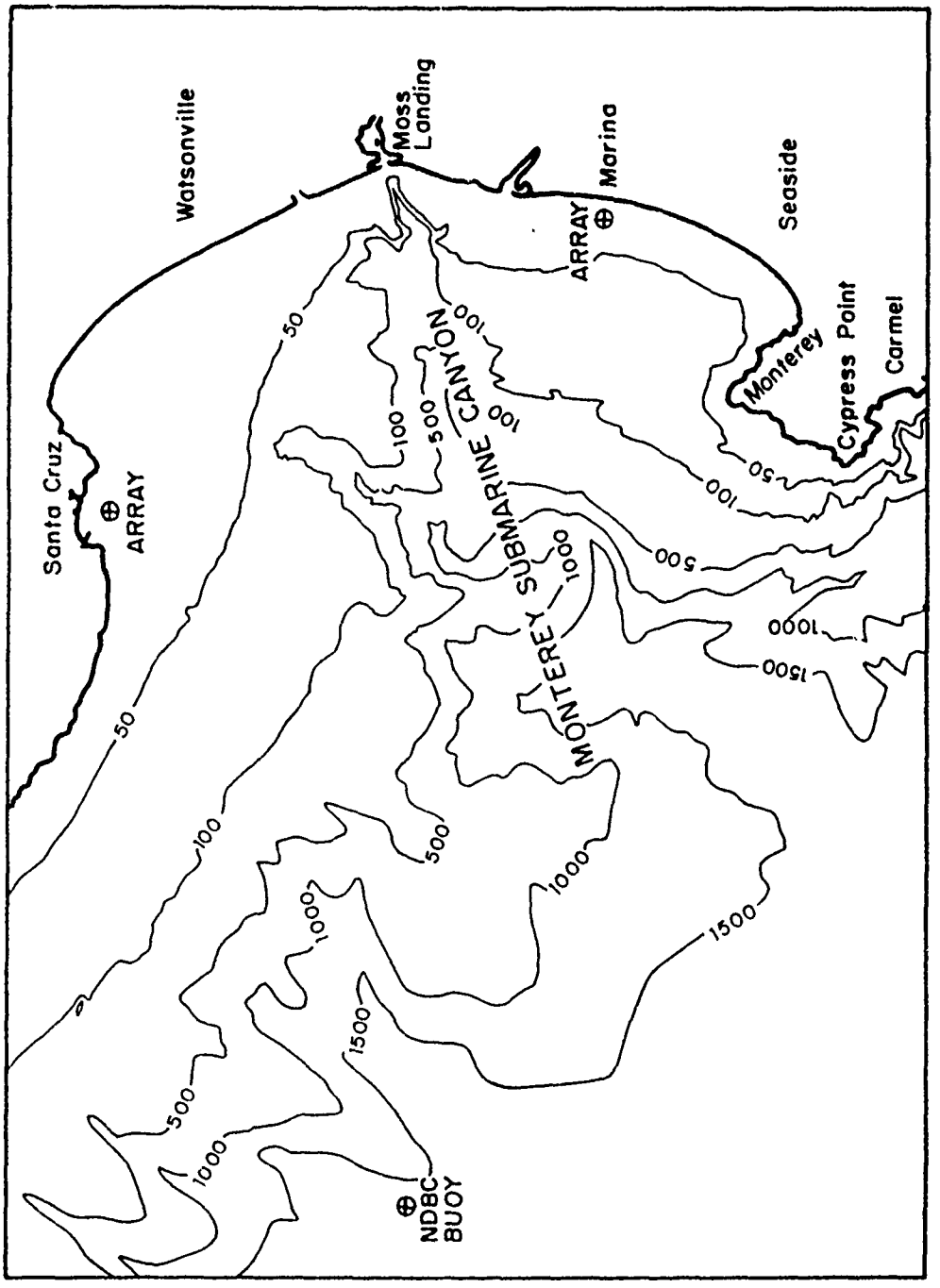

Figure 6.2: Bathymetry and ground truthing assets in Monterey Bay.

spatial regions to meet the required homogeneous conditions. This area presents an interesting problem in predicting directional wave spectra.

The sloping bottom introduces additional various dynamic ocean features like gradients in the tidal flows. The present study concentrates on the dominant surface waves spectra and currents. Shoaling waves undergo refraction, reflection and diffraction influenced by the wave approach angle and bathymetry. The complex bathymetry of Monterey Bay is shown in Figure 6.2, and the detailed bathymetry near Marina in Figure 6.3. Wave refraction at the Marina array site is shown in Figure 6.4 for different frequencies (0.03 Hz to 0.13 Hz). Linear refraction theory (see Chapter V) predicts that lower frequency waves (longer waves) experience more refraction. All possible incoming ray traces with wave angles at increments of 0.2° using Dobson's model (see Dobson, 1967) are plotted from shallow to deep water. High frequency waves of at least 0.11 Hz are limited to directions from 234°–311°, whereas lower frequency waves may arrive also from southerly directions since they experience more refraction.

An important feature in the experimental site is the Salinas River, which was blocked from the sea at this time of the year (June–September) providing a natural closed basin. This allowed the study of Bragg backscattering waves only, without the contamination by interactions with long waves or any underlying currents.

C. THE MARINA EXPERIMENT

The Marina experiment consisted of four SAR and INSAR overflights in the interferometric mode on September 8, 1989. Radar data were acquired about an area centered on the shallow water wave array (see Figure 6.5) with the antenna

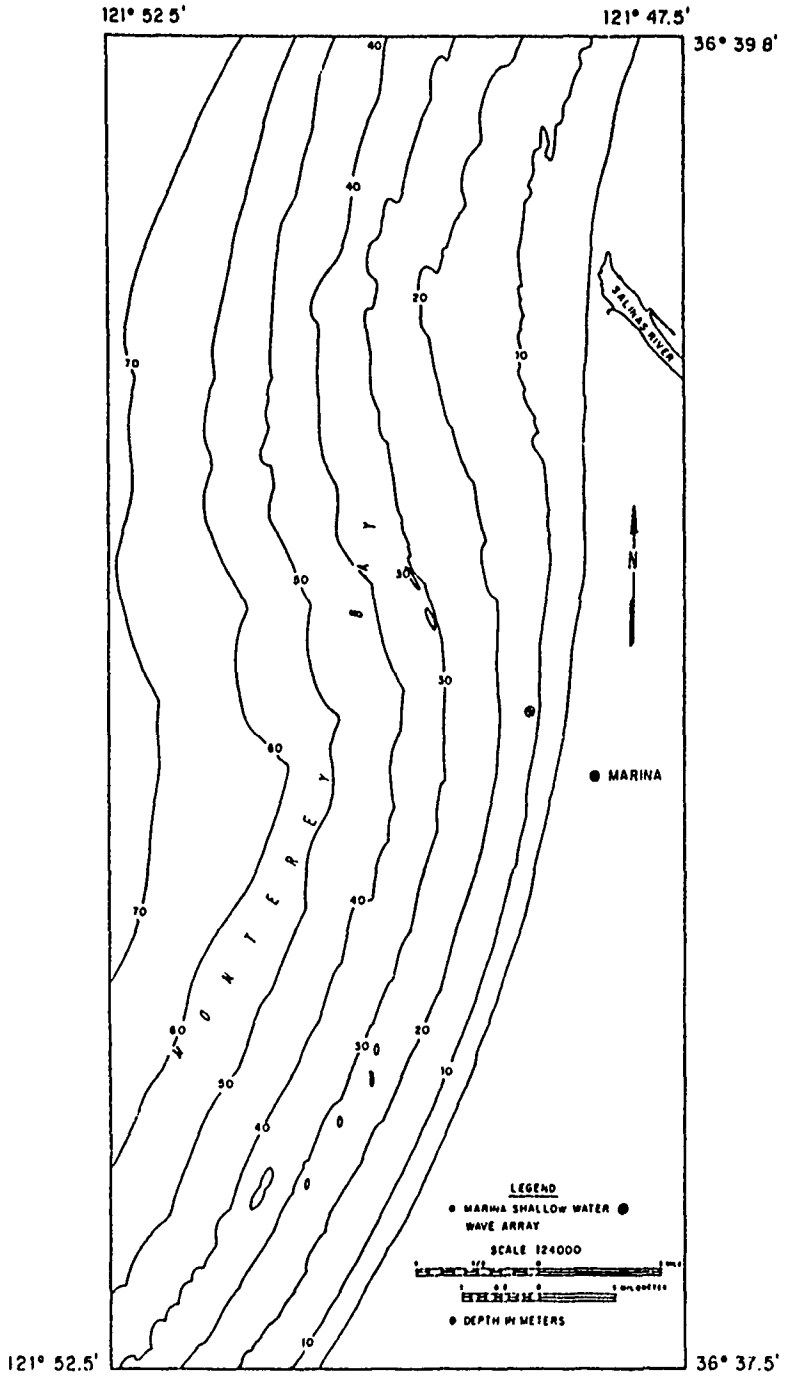

Figure 6.3: Detailed bathymetry of the nearshore region of Marina Beach.

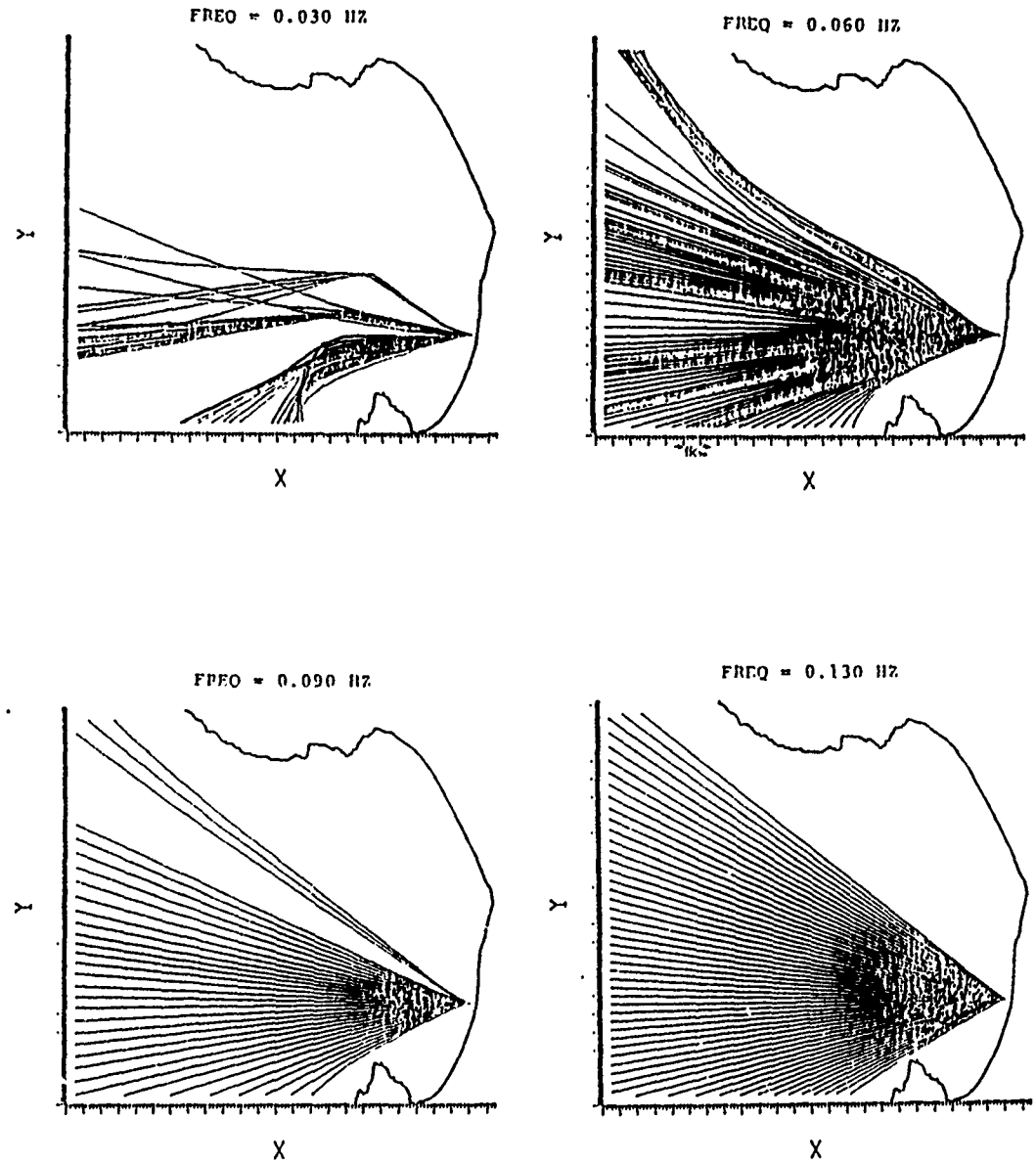

Figure 6.4: Refraction wave ray traces off Marina Beach at different frequencies.

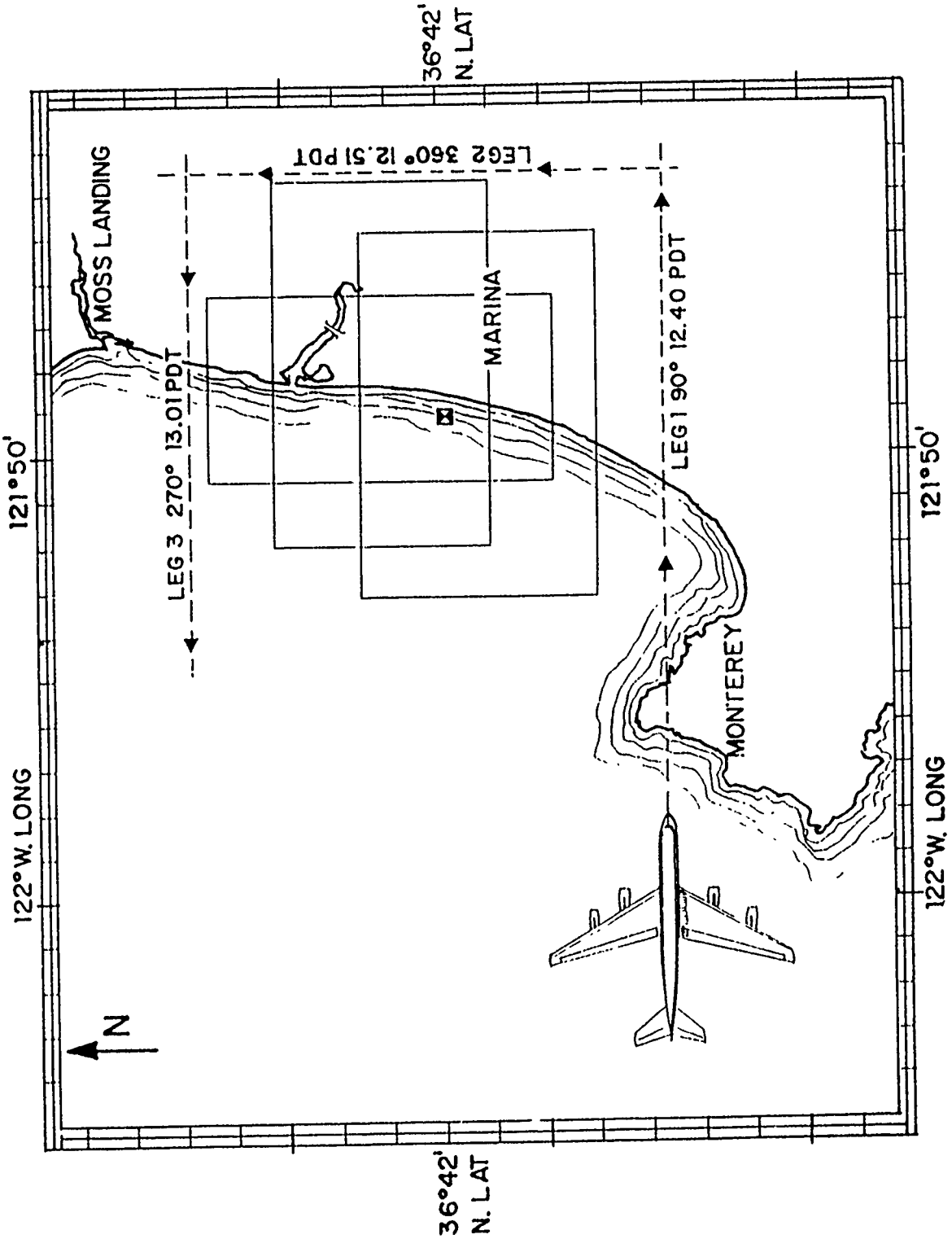

Figure 6.5: Flight pattern and scene locations for radar data collection on September 8, 1989 off Marina Beach.

beams aimed at the *in situ* wave array with a depression angle of 45° and mean altitude of 8250 m. The radar overflights were conducted around 1300 Pacific Daylight Savings Time close to the time of maximum tidal flood current. The flight pattern and the scene locations of radar data collection are illustrated in Figure 6.5. Some key system and flight characteristics are depicted in Table 6.1. More detailed SAR system characteristics are given in the next chapter.

The Lagrangian floating drifters for tracking the very top surface currents were deployed and tracked by the R/V Ricketts with the aid of a Piper Cherokee Arrow (PCA) light aircraft (Figure 4.15). A portable LORAN-C enabled the light aircraft to locate roughly the drifters while the vessel, and hence the drifter positions, were recorded using a high accuracy Motorola Mini-Ranger Falcon 484 system.

The actual time schedule and sequence of events in the Marina experiment on September 8, 1989 were as follows:

081000 Departure of R/V Ricketts from Moss Landing home base.

081050 On station (Marina shallow water array) to test the navigation system (Mini-Ranger) and to estimate local surface currents by deploying and positioning two drifters. This pre-measurement was done in order to optimize the deployment pattern of the drifters to obtain maximum coverage of variable surface currents within the expected airborne radar scene for data collection. The variability of the bathymetry was part of the concern in ground truthing the radar surface current estimates at variable depth.

081120 Termination of initial test, vessel steaming westward to the first deep water deployment station.

081145 – 081230 Buoy deployment from west to east in three distinct groups, each group consisting of five drifters for a total of fifteen (see Figure

TABLE 6.1: System and Flight Data for the Different Aerial DC-8 Aircraft Coverage During Marina Experiment, September 8, 1989

	90° EAST-WARD LEG	270° WEST-WARD LEG	360° NORTH-WARD LEG
Initial data collection time, PDT	12:40	13:01	12:51
Aircraft velocity, m/s	214	216	214
Aircraft altitude, m	8285	8273	8178
Pulse repetition frequency , Hz	283	285	282
Near incidence angle, degrees	17	Nadir	Nadir
Far incidence angle, degrees	52.7	50.2	50.7
Ground pixel range spacing, m	8	7	6
Azimuth pixel spacing, m	12.1	12.1	12.1
Effective coverage range × azimuth, km^2	6 × 14	5.1 × 14	5.8 × 14

6.6). Group one drifters, numbered 1 thru 5, were deployed furthest offshore approximately 3.4 nm west of the shore where the mean water depth is 71 m. This group was positioned four times during the three hour observation period. Group two drifters, 6 thru 10, were deployed closer to the shore, approximately 1.6 nm west of the beach where the mean water depth is 44 m. These were positioned three times. Group three drifters, 11 thru 15, were deployed less than 0.6 nm from the beach and washed ashore before a second position could be obtained. Within

each group, the drifters were deployed roughly 0.1 nm apart as the vessel steamed eastward toward the beach.

081220 The Piper Cherokee Arrow light aircraft arrived on station Monterey Airport and started to position and photograph the drifters from west to east.

081230 – 081515 Drifters chased, with vessel heading west to position the drifters first deployed. The initial detection of the Lagrangian drifters was quite tedious. Applying Direction and Range (DR) estimates based on the early test results, the drifters were not detected. The light aircraft was very helpful in detecting the drifters initially, although the radio communications broke down. Therefore the actual communication was done by turning on the landing lights and heading towards the R/V Ricketts once the Piper overflew a group of drifters. As predicted, the onshore tidal current became more intense close to the time of midtide range (1320), yielding a stronger eastward component, which was measured by the drifters. The second DR prediction based on the initial physical positioning was close to the actual positions of the drifters.

081240 – 081310 SAR overflight acquired data in the INSAR mode.

081405 The Piper light aircraft heads home to Monterey.

081515 R/V Ricketts heads home to Moss Landing after retrieving ten of the drifters from the two most western groups. The most eastward group of drifters, which were washed ashore, were collected four days later from Marina Beach.

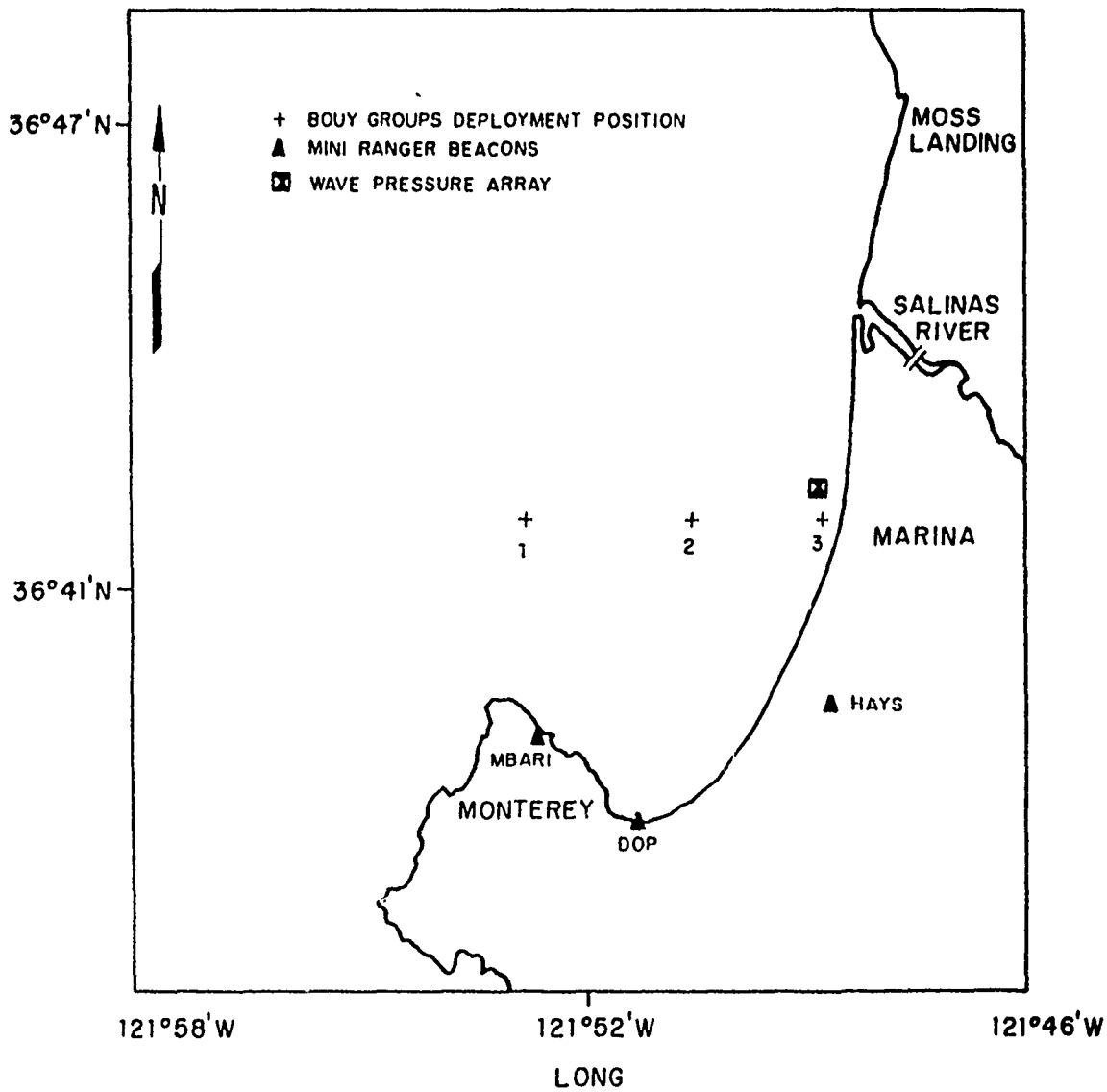

Figure 6.6: Drifter deployment positions and Mini-Ranger reference stations during the Marina experiment, September 8, 1989.

D. ENVIRONMENTAL CONDITIONS

1. Introduction

The environmental conditions which occurred during the Marina experiment on September 8, 1989 were typical late summer conditions for Monterey Bay. Light westerly winds (less than 4 knots), surface air temperature of 14–16°C and clear skies up to 1000 feet blocked by a stratus cloud deck, were observed during the 1000–1500 Pacific Daylight Time (PDT) experiment period (see Table 6.2).

The mild local meteorological conditions during this period resulted in almost no local generation of sea. The sea surface was predominantly long crested, narrow-band waves propagating shoreward. Therefore, the scene was linear in character, yielding a linear Modulation Transfer Function (MTF) of the ocean surface for imaging radars.

Due to the lack of predicted tidal current information for Marina Beach, the time of maximum tidal current was estimated using predicted information of tides at Monterey Harbor and Moss Landing, which are located almost in equal distance (17 km) south and north off Marina Beach. Predicted tidal high and low water times (NOAA 1978 Tide Tables) of Monterey Harbor and Moss Landing are plotted in Figure 6.7. Based on the figure, the maximum flood tidal current was probably at 1320 PDT.

The summer climatological atmosphere surface circulation in the eastern North Pacific consists of a high east-west pressure ridge stretching from west coast California to almost 140° E (east longitude). The ridge extends to approximately 20° N (north latitude). Below 20° N, the atmosphere has tropical characteristics. This late August high pressure system was deformed in shape and orientation (see Figure 6.8) by a series of northwest lows, which might be the source of the northwesterly

TABLE 6.2: Environmental Conditions During the WAFICIN Marina Experiment

Time and date	1030-1500 PDT, September 8, 1989
Air temperature	14 to 16°C
Surface Water temperature	~ 13°C (est.)
Relative humidity	~ 60% to 70% (est.)
Wind direction	Varying between northeast and southeast
Wind speed	$\leq$ 2 m/s
Visibility	Up to 1000 ft 7 miles. Above 1000 ft overcast by low stratus cloud deck.
Significant wave height	< 0.6 m
Dominant swell periods	a. 9.1 sec b. 15.9 sec
Expected time of maximum flooding tidal current	1320 PDT
Swell directions	a. East Northeast (long swell) b. East Southeast (short swell)

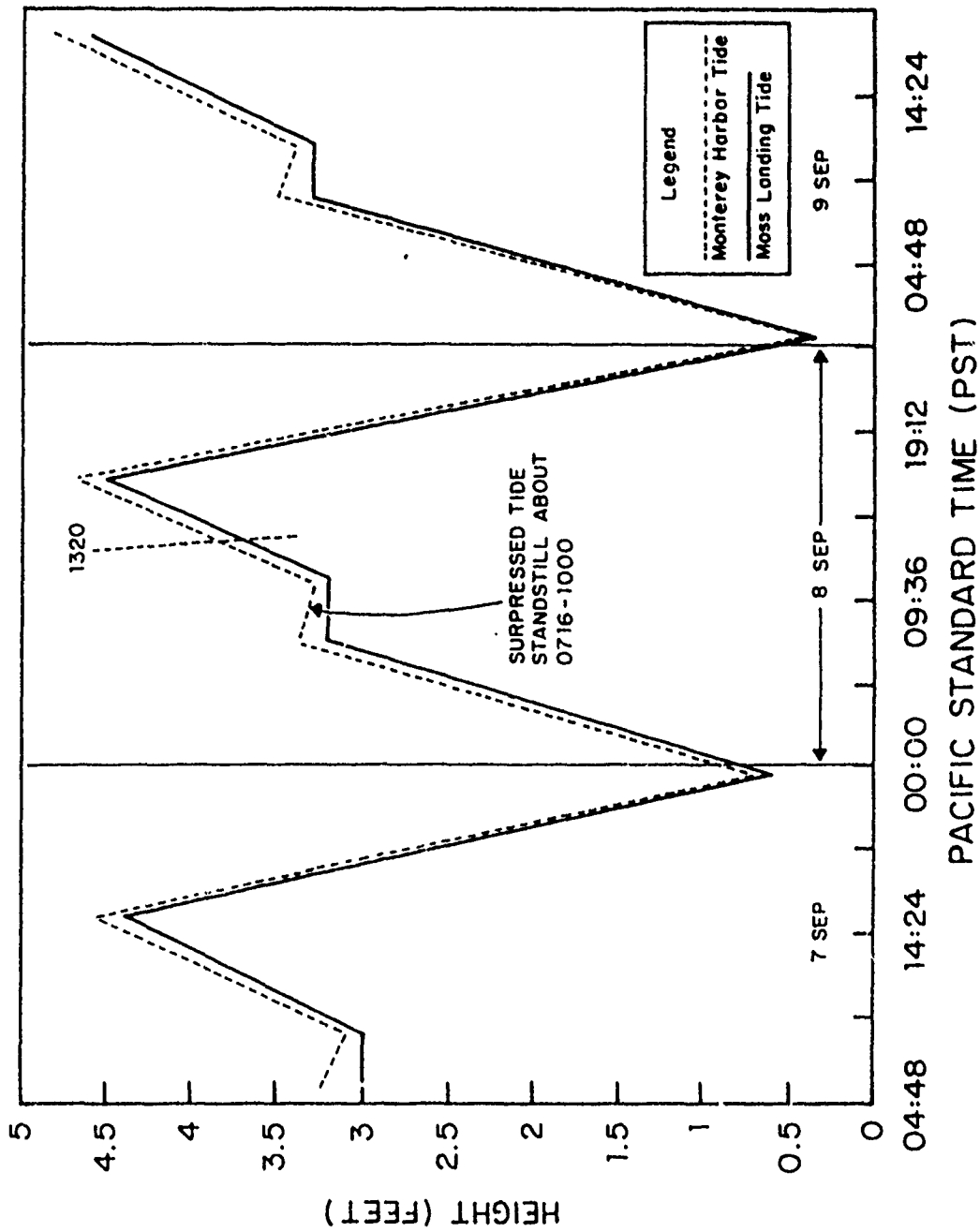

Figure 6.7: Monterey Harbor and Moss Landing predicted tides, September 7–9, 1989.

9.1 sec. swell with travel time of almost 4 days observed in the Marina experiment on September 8, 1989. The 15.9 sec. long crested westerly swell is postulated to be generated by a late winter southern hemisphere storm located at 40° S to 60° S in the South Pacific. The travel time for the swell from this storm to Monterey Bay is almost 8 days (see Figures 6.8 and 6.10).

2. Evolution of Environmental Conditions

When investigating the possible sources of the observed swell waves in the Marina experiment, three different sources of process data were analyzed:

- Surface winds and pressure field patterns between August 31 and September 8, 1989, based on NORAPS/SAC model outputs processed by Fleet Numerical Ocean Center (FNOC) in Monterey (see Figures 6.8, 6.9).
- Wave group velocity vectors and significant wave height contours, based on Global Spectral Ocean Wave Model (GSOWN) outputs, between August 31 and September 8, 1989, also processed by FNOC in Monterey (see Figures 6.10, 6.11).
- Geostationary Operational Environmental Satellite (GOES) visible imagary (Figure 6.12).

3. Surface Winds and Pressure Fields

The surface pressure field pattern on August 31, 1989 in the eastern North Pacific was in good agreement with climatology. From the 1st of September 1989, the east-west orientation of the ridge axis shifted to a northeast, southwest orientation. This shift was caused by the development of a strong low pressure system south of the Aleutian Islands and the development of an induced trough

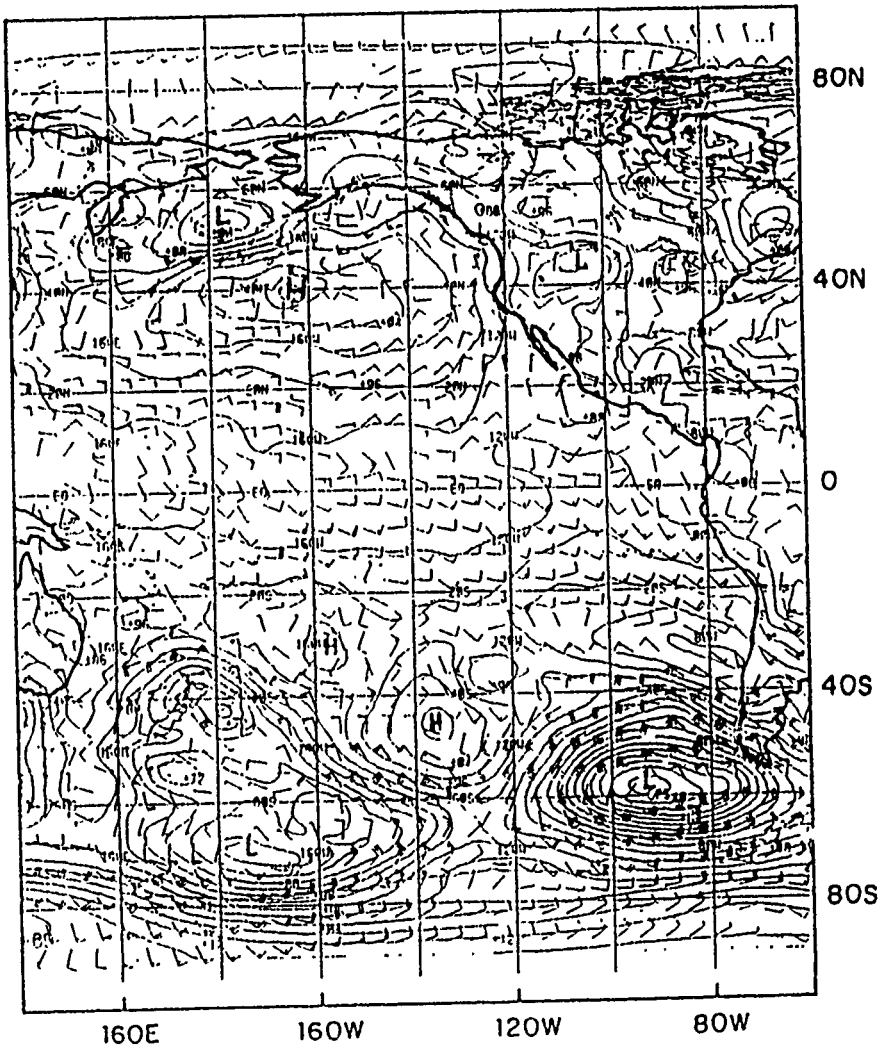

Figure 6.8: Mean sea level pressure contours and wind vectors at 1700 PDT on August 31, 1989.

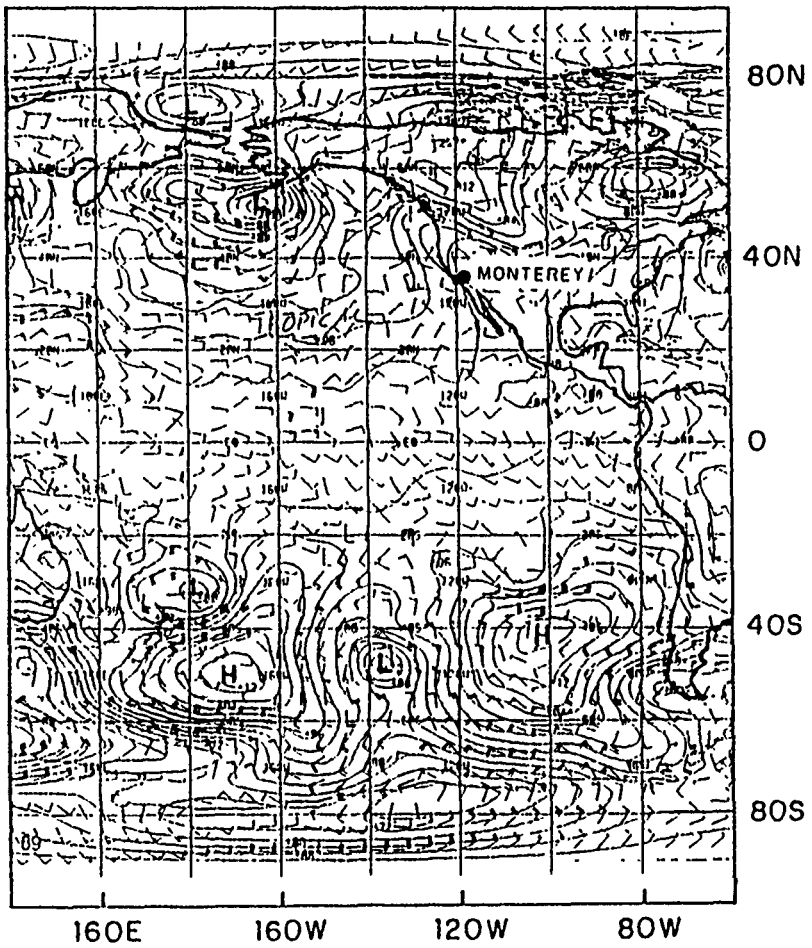

Figure 6.9: Mean sea level pressure contours and wind vectors at 1700 PDT on September 8, 1989.

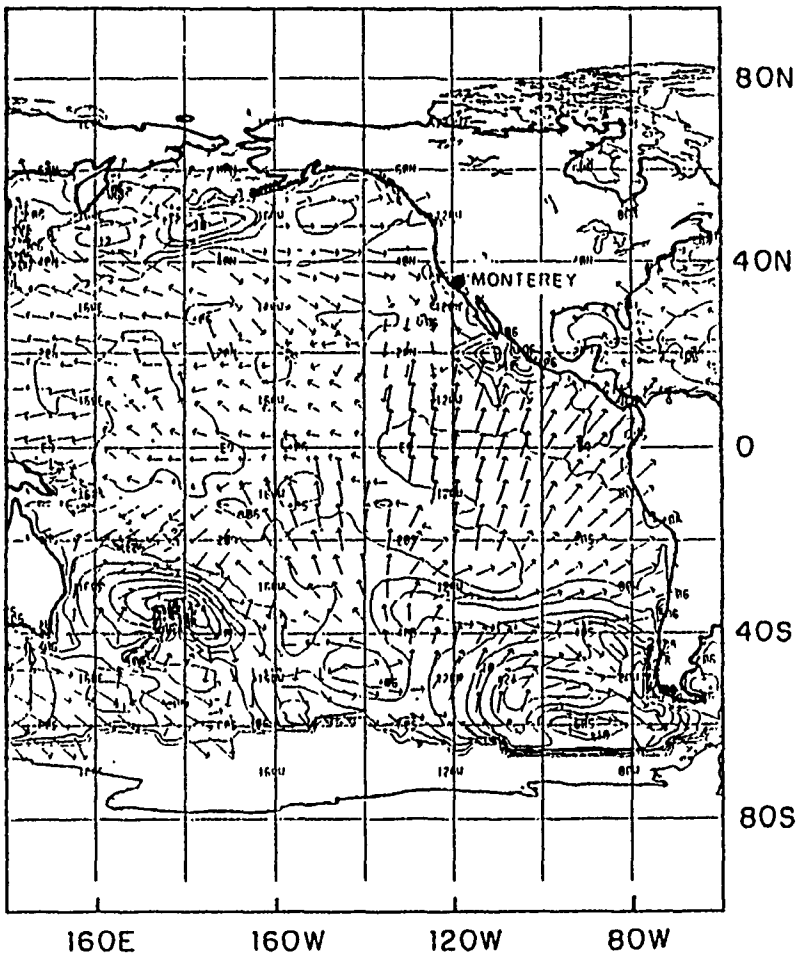

Figure 6.10: GSOWN wave group velocity vectors and significant wave height contours at 1700 PDT on August 31, 1989.

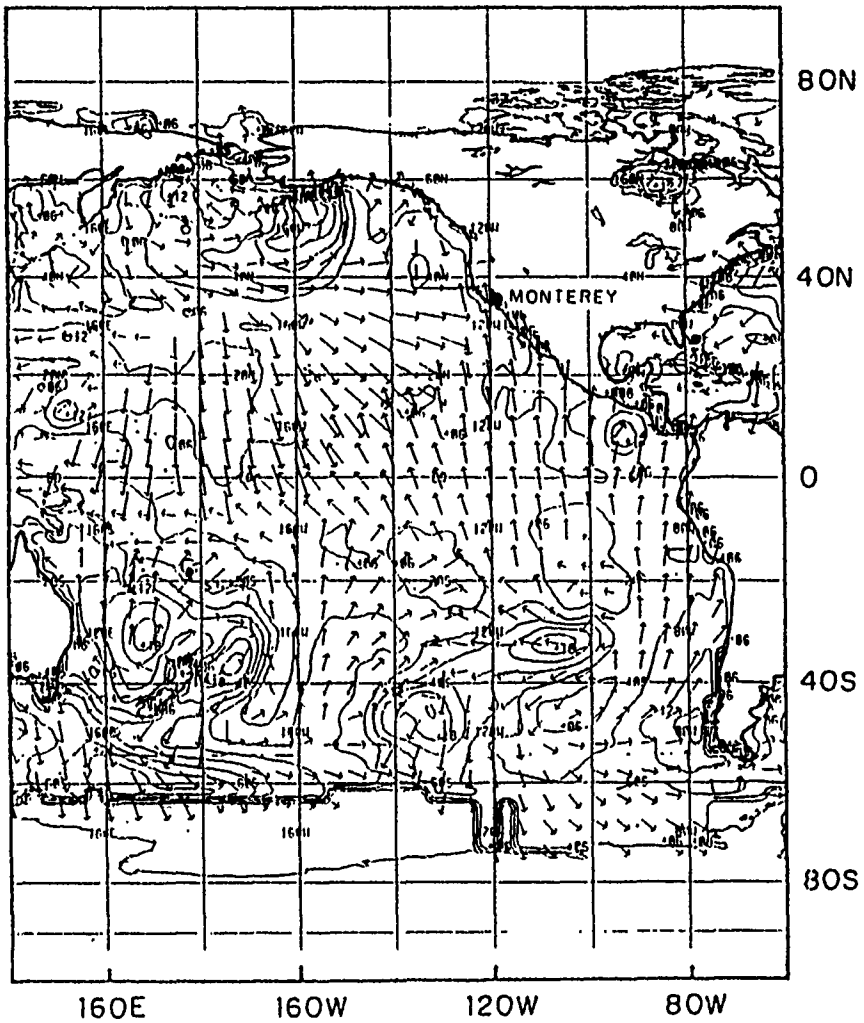

Figure 6.11: GSOWN wave group velocity vectors and significant wave height contours at 1700 PDT on September 8, 1989.

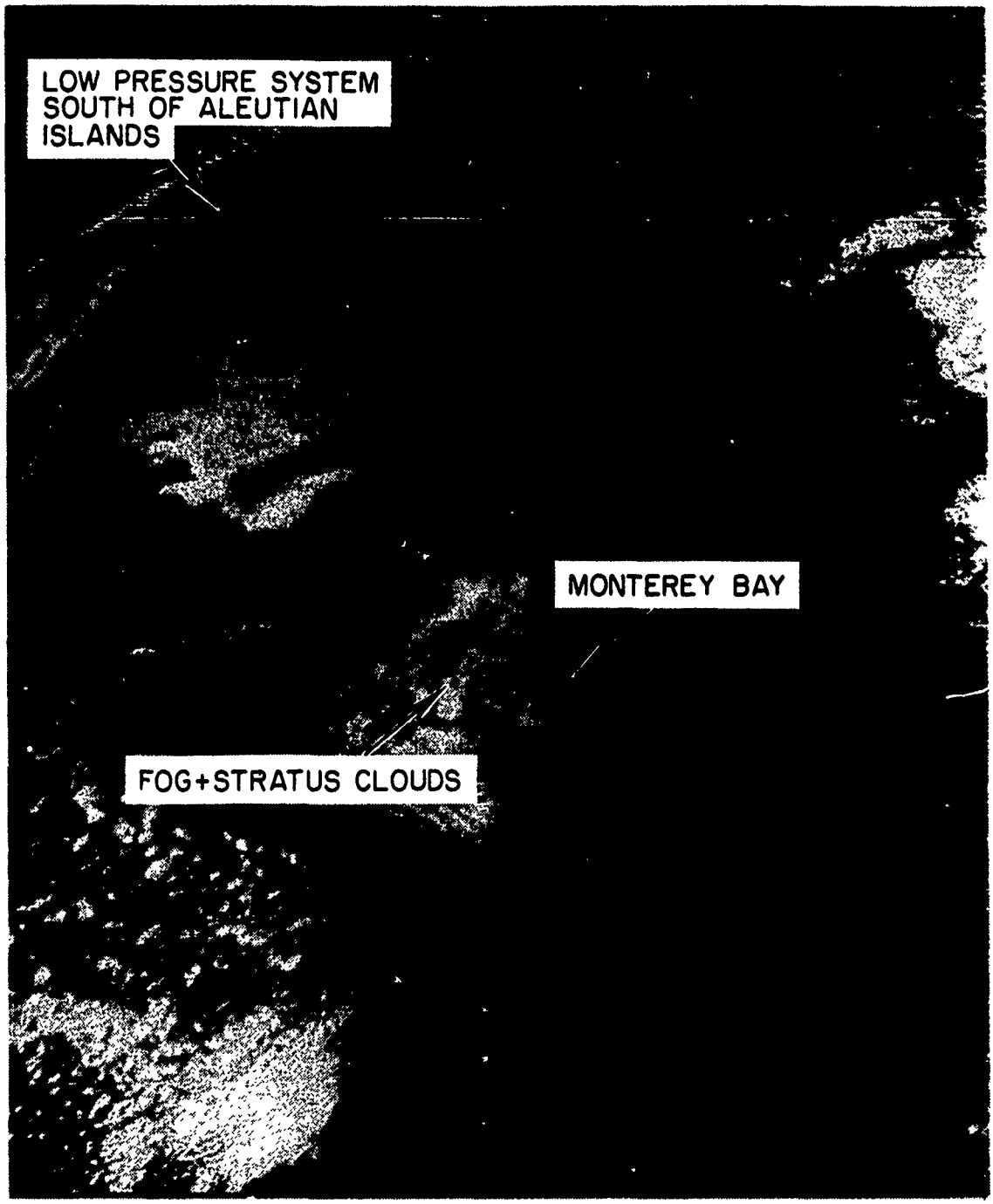

Figure 6.12: GOES visible imagery at 1331 PDT on September 8, 1989.

over California and the Pacific Northwest. These pressure field conditions were maintained through September 8, 1989 yielding stable conditions with light winds parallel to the coast and westerly light winds between 35° N to 38° N (Figure 6.9). These computed wind fields based on NORAPS/SAC model are in agreement with the observed wind tendancy during the Marina experiment.

The migration of the pressure ridge northward inducing stable light wind conditions over the west coast enabled wave systems produced by northwest Pacific storms to propagate eastward without local air-sea disturbances. As mentioned previously, these developing storms appear to be the source of the shorter period swell (9.1 sec.) observed on September 8 in the Marina experiment.

4. Satellite Data

Analysis of GOES imagery confirms the presence of an induced trough over California and Pacific Northwest (see Figure 4.12). The low pressure system south of the Aleutian Islands, which is believed to be the source of westerly winds, caused the 1000 foot ocean stratus deck to approach the central and North California coast. The winds were not strong enough to advect the clouds over the land. The cloud deck prevented the collection of satellite sea surface temperature data for the region of interest on the experiment day, September 8, 1989.

E. INSTRUMENTATION CHARACTERISTICS AND PERFORMANCES

The relevant performance of assets which aided the collection of data in the simultaneous experiments are described in the first part of this section. The procedures of data acquisition and initial sorting are described in the second part of this chapter.

The sensors which were used in the Marina experiment on September 8, 1989 include remote and *in situ* assets measuring synoptic spatial variations and Eulerian and Lagrangian temporal variations of the ocean surface, respectively.

1. Platforms

- NASA/JPL DC-8 airborne INSAR and SAR imaging radar remotely sensing ocean surface velocity fields and surface intensity reflectivity.
- R/V Ricketts for deploying and tracking Lagrangian floating drifters following the very near surface currents. High accuracy Mini-Ranger navigation system ($\sim$ 5m RMS error) for positioning the vessel, and hence drifter positions, was installed on board of R/V Ricketts in addition to the inherent Loran-C navigation system with lower accuracy ($\sim$ 65 m RMS error).
- Light aircraft Piper Cherokee Arrow (Figure 6.15) for detecting and observing the wooden sheet floating drifters, which were undetectable initially by conventional means (radar, visible) from the surface platform (R/V Ricketts).

2. *In situ* Assets

- Ocean wave directional spectra and surface wind data acquired from:
  - Shallow water pressure gauge array located at a depth of 16 m off Marina Beach at:

    36°42′ North Latitude

    121°48.9′ West Longitude
  - Anemometer on Marina Beach located at 36°42′ N. Lat, 121°48.9′ W. Long from which directivity of the Bragg waves may be inferred.
- Lagrangian drifters following the very near surface currents tracked by the Motorola Mini-Ranger navigation system.

- NAVSTAR Global Positioning System (GPS) extremely accurate positioning system for ground truthing the geographic coordinates of SAR and INSAR images (see Chapter VII. B3).

3. Platform Characteristics

a. NASA/JPL DC-8

The NASA/JPL DC-8 (Figure 6.13) has a multifrequency, multipolarization airborne SAR system operating at L, C and P-Band (Held et al., 1988) with a full digital recording capability and an inertial navigator system for measuring three dimensionally the aircraft attitude. Detailed performance of the system characteristics are given in in Table 6.3.

At L and C-Band the radar can operate in an along track interferometer mode by using the physically separated fore and aft antennas mounted on the left looking side of the aircraft fuselage. In this experiment, the L-Band interferometer was used in vertical polarization since the ocean reflectivity at moderate incidence angles 20°–70° (Bragg resonant backscatter) is more intense as compared with horizontal polarization.

The receiver has no Sensitivity Time Control (STC) or Automatic Gain Control (AGC) capabilities. Instead a wide dynamic gain range (30–56 dB) is implemented to compensate for signal saturation. This is achieved using 8 bit Analog to Digital Converters (ADC) which are clocked together to ensure registered samples. Due to the high digitizing rate of the ADC's (45 MHz), real data samples (the imaginary part is not recorded) are produced at a total data rate of 20 to 60 MBytes/second. The data from each receiving channel is multiplexed together to form an extended "range line" for recording onto any of the three available High

Density Digital Recorders (HDDR) at a rate of 80 MBits/s (see Fig. 6.15). No high resolution processing capabilities exist onboard the aircraft (Held et al., 1988).

b. R/V Ricketts

R/V Ricketts (see Figure 6.16) is a 35 foot light craft suited for day cruises on Monterey Bay. The vessel is owned and operated by Moss Landing Marine Laboratories. For her size the R/V Ricketts is reasonably equipped with navigation and deck handling equipment to function as a field station for oceanographic observations.

4. *In Situ* Assets Characteristics

a. Shallow Water Wave Array

The Marina shallow water wave array consists of four pressure gauges configured in a square, six meters on a side, aligned 6° off true North (see Figure 6.16). The pressure sensors are located 0.5–1 m above a mean bottom depth of 16.2 m. The northern sensor is a parascientific model 2100AS, digiquartz pressure sensor which produces output voltage signal proportional to the absolute water surface elevation. The other three pressure sensors are based on a piezo-resistive gauge transducer manufactured by Kulite Semiconductor. The array was developed to provide wave directivity in shallow water. The azimuthal resolution of the array depends on processing methods, and was 4–6 degrees for the range of resolved wave periods between 5–20 sec. Data from the shore station is acquired and initially screened by a computer based control station located at Scripps Institution of Oceanography, La Jolla, California.

b. Wind Speed and Direction from Skyvane Wind Sensor

A 2102 Skyvane four bladed, low threshold propeller wind sensor is mounted on the beach at Marina at an altitude of 27 m from MSL (see Figure 6.17).

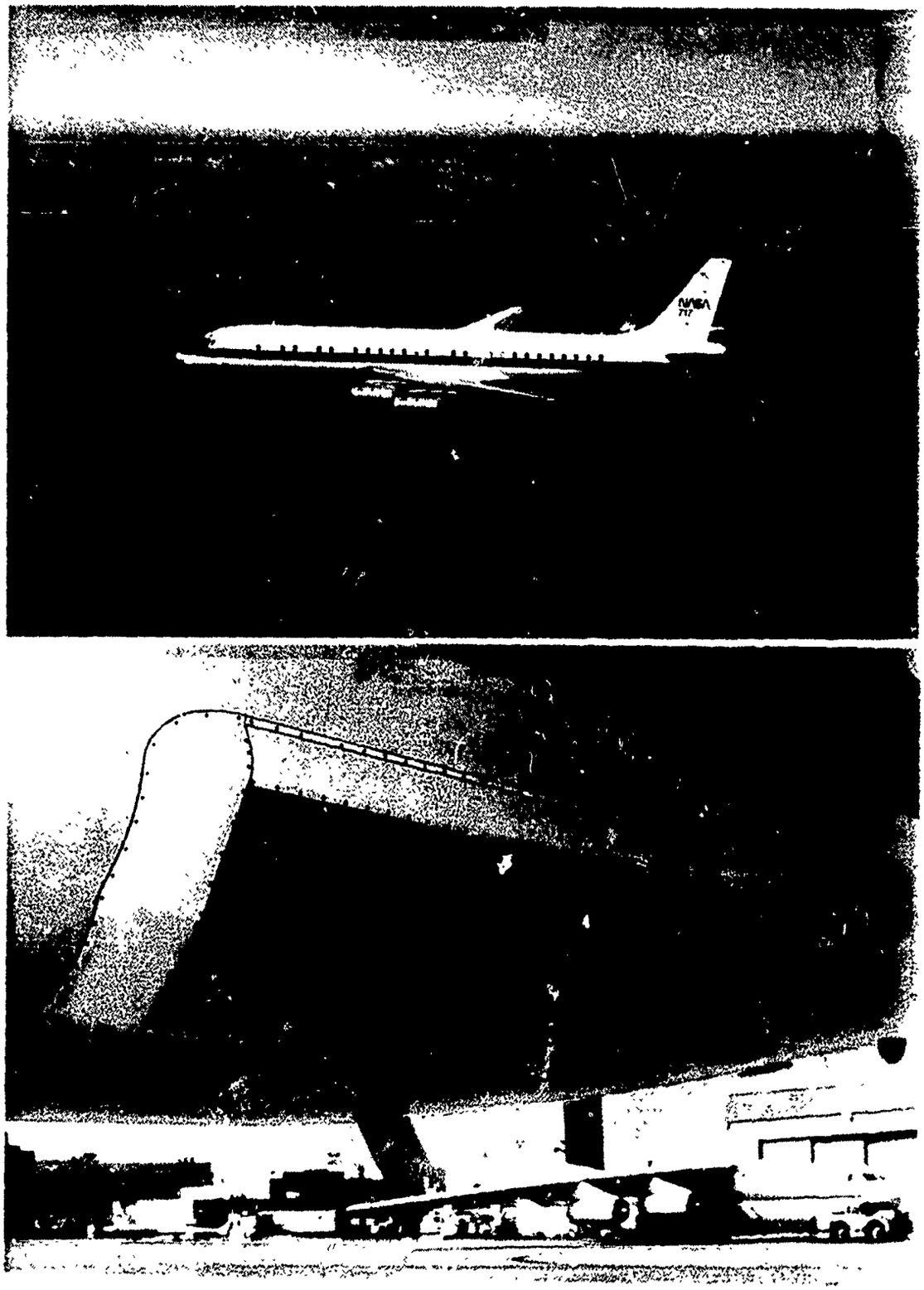

Figure 6.13: NASA/JPL DC-8 research aircraft. *Top*: overall view; *Bottom*: SAR antennas.

TABLE 6.3: NASA/JPL DC-8 Airborne Imaging Radar Parameters Employed During Marina Experiment, September 8, 1989

Data	L-Band
Frequency, MHz	1237–1260
Center frequency, MHz	1248.75
Wavelength, cm	24
Chirp length, μs	11.25
PRF/V, Hz / m/s	1.32
Band width, MHz	20
Peak power, kW	6
Azimuthal beamwidth, deg	8
Vertical beamwidth, deg	44
Antenna beamcenter gain, dB	18.3
Azimuthal pixel spacing, m	3.03 × 4
Slant range spacing, m	6.6
Polarization	VV
Receiver dynamic range (dB)	30–56
Number of bits per sample	8
Number of looks	1
Available number of pixels (range × aximuth)	750 × 1024

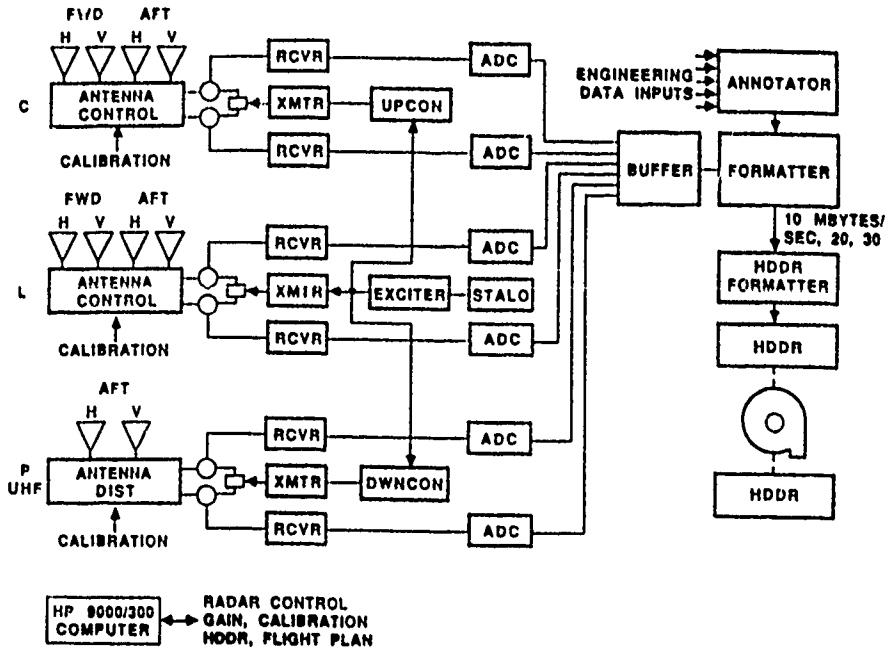

Figure 6.14: NASA/JPL airborne radar and recording block diagram. The L-band interferometric mode was used for the acquisition of data in this study (from Held et al., 1988).

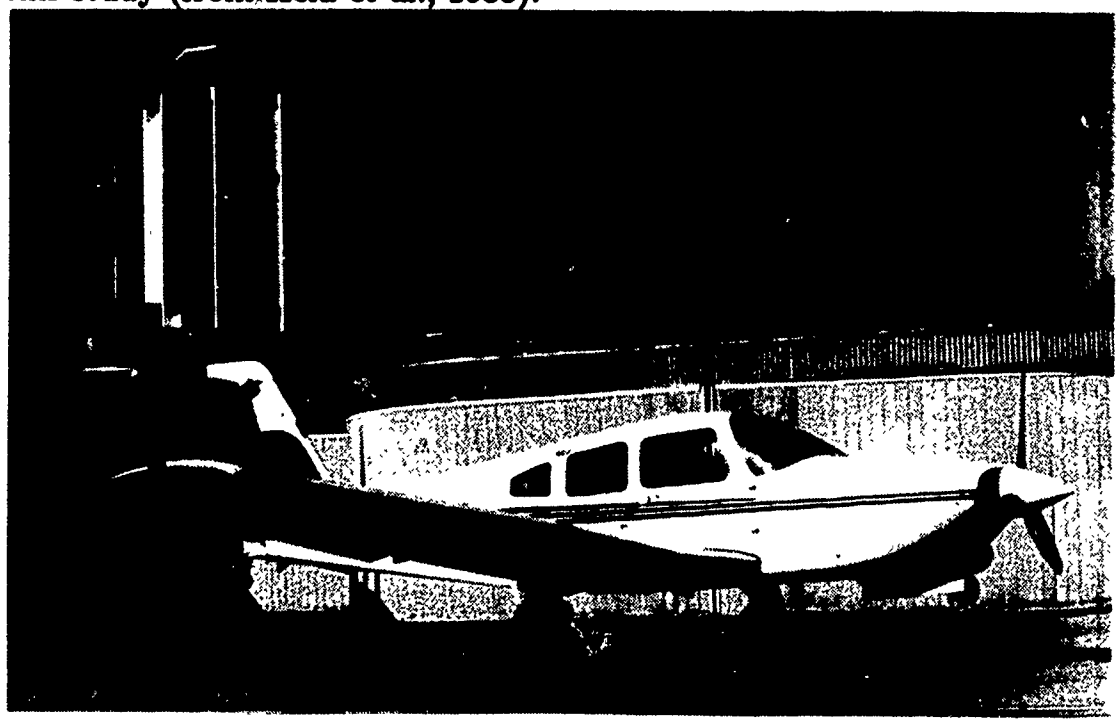

Figure 6.15: Light aircraft Piper Cherokee Arrow participated in the Marina experiment, September 8, 1989.

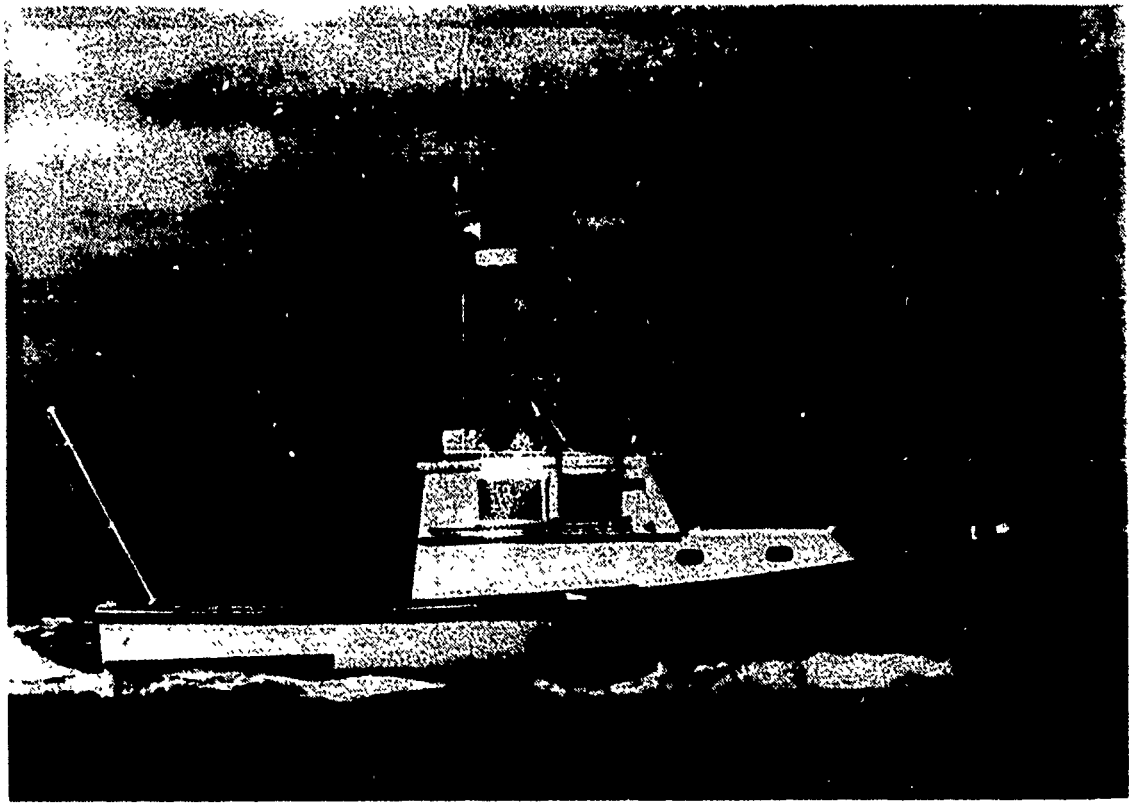

Figure 6.16: R/V Ricketts participated on the final experiment on September 8, 1989.

The accuracy of wind speed measurement is ± 0.5 m/sec for wind speeds less than 15 m/sec. The accuracy for wind direction is ± 1% of the full scale (±180°).

c. Lagrangian Drifters

Two types of drifters were tested in our experiments to measure near surface currents. In the preliminary experiment on July 24, 1989, a passive radar free floating drogue was used. It was tracked by a surface navigation radar installed on R/V Point Sur and positioned accurately by the Mini-Ranger navigation system. A prototype test of various drogue types were tested on June 1, 1989. For further details see Appendix C.

Based on the results of the preliminary experiments, a Lagrangian drifter, made of a 2 cm thick plywood sheet and 0.4 × 1.2 m in dimension was used

for ground truthing in the analysis of this study. The dimensions of the drifters were selected after considering the measurements by Stewart and Joy (1974) and Goldstein et al. (1989), in which radar measurements of near surface currents were compared with simultaneous measurement by drifters. At L-band the corresponding ocean resonant Bragg waves (21–25 cm at 30° viewing angle) mostly feel currents in the upper 2 cm of the ocean surface. Therefore, the drifter's thickness insured measurement of the near surface flows experienced by the Bragg backscattering waves while the horizontal dimension reduced the sensitivity to vertical motion of short waves (Goldstein et al., 1989). The drifters were painted red with an identification number on both sides in case of rolling over in the surf zone (see Figure 6.19).

d. Mini-Ranger Navigation System

Vessel positions, and hence drifter positions, were determined using the Motorola Mini-Ranger Falcon 484 system. The system is widely used for precise positioning in a variety of nearshore marine applications. The system consists of a transceiving master station borne on a vessel, and up to four stationary reference stations (see Table 6.4) along the shore. The range to each reference station is computed at the master station based on the measured round trip travel time of the microwave transmitted pulse. The system operates on the principle of a pulse coded transponder. The master and reference stations transmit on different frequencies in the microwave band, 5510 and 5480 MHz to avoid interference. The standard system has a maximum range of 37 km (20 nm) with reference station gain antenna of 13 dB, and a master station omni-directional antenna gain of 6 dB. Ranges from up to

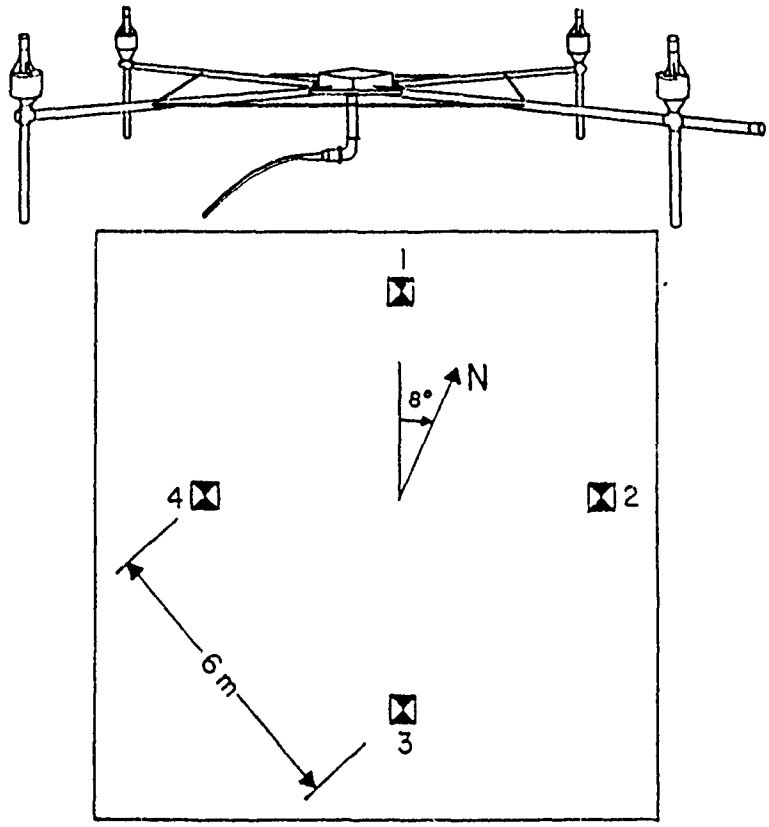

Figure 6.17: Marina shallow water wave array. *Top*: hardware configuration; *Bottom*: geometric orientation.

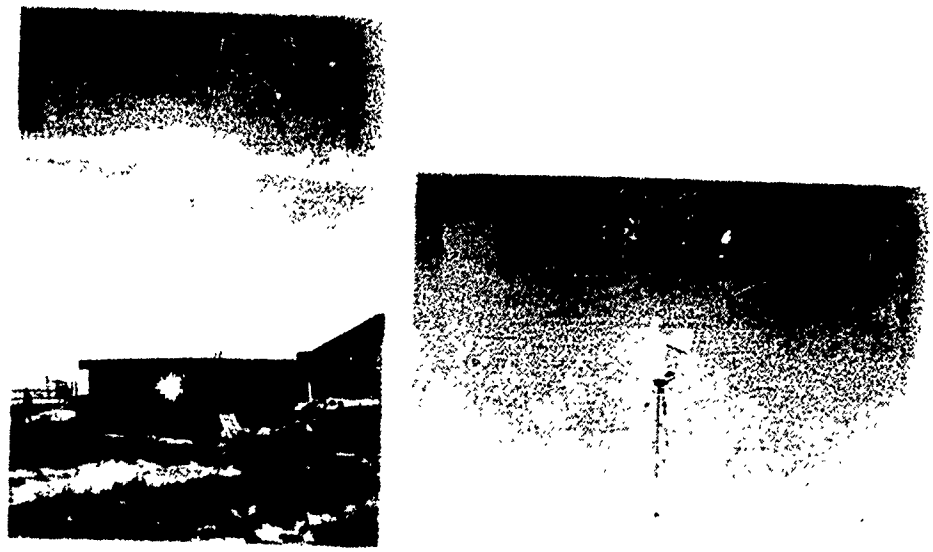

Figure 6.18 Wind anemometer at Marina Beach.

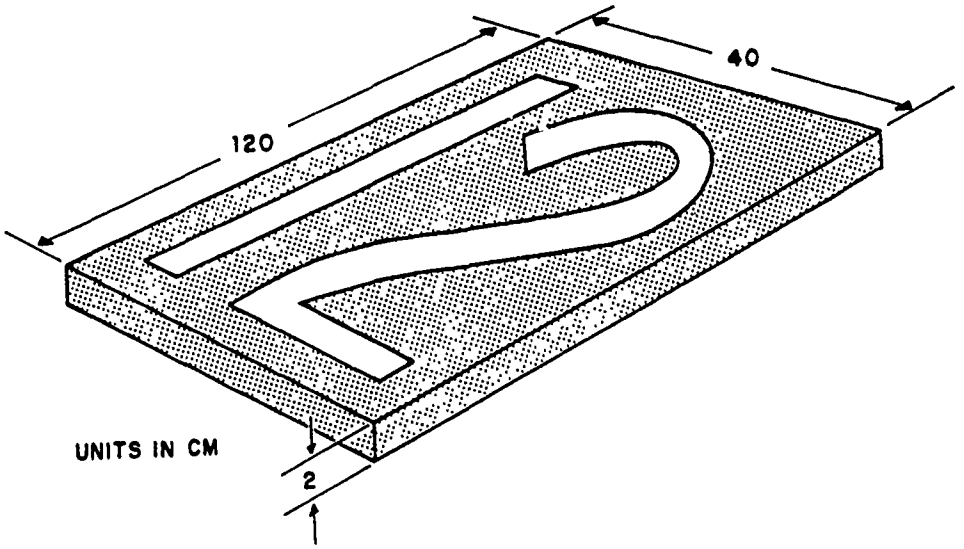

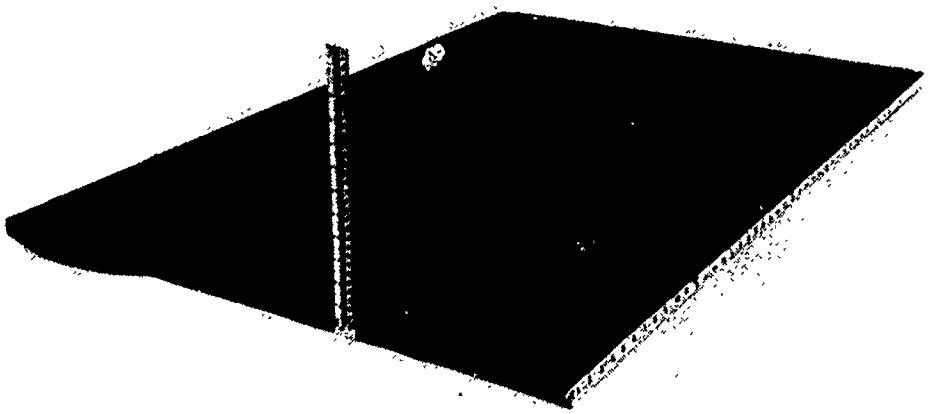

Figure 6.19 Plywood drifter used to Lagrangianly follow surface currents during the Marina experiment, September 8, 1989. *Top*: perspective view; *Bottom*: apparent drifter.

TABLE 6.4: Station and Equipment Data

Horizontal Datum:	North American Datum of 1983 (NAD 83)
Computational Grid:	Universal Transverse Mercator (UTM) Zone 10, central meridian 123° W
Grid Scale Factor Used in Computations:	0.999743
Source of Station Positions:	Surveys by NPS Hydrographic Sciences 1988–1989

Reference Station Positions
(see Figure 6.6):

Nick-Name	N Latitude W Longitude (deg min sec)	UTM Coordinates Easting (m) Northing (m)	Elevation MSL (m)
WATS	36 54 26.895 121 50 39.819	602947.7 4085231.4	23.1
HAYS	36 38 33.826 121 47 45.895	607621.3 4055915.3	137.2
DOP RM1	36 36 5.601 121 52 37.479	600434.0 4051260.0	10.0
MBARI RM	36 37 6.868 121 54 20.156	597861.5 4053118.5	30.7

four reference stations, with an rms triangulation position of ~ 5 m, were recorded onboard (see next section).

F. DATA ACQUISITION AND INITIAL DIGITAL PROCESSING

In this section, the initial processing methods of the data acquired in the Marina experiment on September 8, 1989 are discussed. The processing of the airborne radar data at JPL, the shallow water wave array data initially processed at Scripps Institute of Oceanography, and the processing of the drifter and GPS data acquisition are described.

1. Airborne Radar Data

The onboard high density digitally recorded radar data is processed into a two dimensional imaging map at JPL. The Airborne Imaging Radar (AIR) off-line processor is run on a VAX 11/730 minicomputer assisted by an array processor FPS-5210. The AIR processor is able to provide two main products: a survey product and a high resolution product. The survey processor is a quick look processor, scanning the raw data tape to determine the quality of the data and whether the data is suitable for futher processing. The high resolution processor provides a high quality complex image. The functions which were used to process the data in the present study are as follows (Nguyen, 1987, Held et al., 1988).

a. Range Compression

The range complex matched filter to the transmitted signal is generated from a real range offset signal whose spectrum is the complex conjugate of the transmitted signal. In order to suppress sidelobes, the range reference function is weighted by a cosine function. The range compression is done by inverse Fourier transforming the product of two Fourier transform sequences of the match filter and

the data. In order to reduce spectrum overlap, the data were subjected to a four-fold decimation by applying a bandpass prefilter in the azimuth dimension centered at the Doppler centroid frequency. This decimates the azimuth resolution by a factor of 4 relative to the nominal SAR resolution.

b. Azimuth Transform

The temporal range history, that is, the phase history of a stationary synthesized target, is a function of the instantaneous range difference between the airborne radar and the target. Therefore, the range of this target can be approximated as a quadratic function of time over the synthetic radar aperture. This effect is known as range curvature, or range migration, and has to be corrected so that the energy of a point target will be contained only in range bias parallel to the azimuth dimension. This correction is done in the frequency domain. The range compressed data are first read into azimuth direction format and then Fourier transformed using a 8192 point FFT.

c. Range Cell Migration (RCM) Correction

The RCM correction algorithm rearranges the data so that the quadratic phase history effect in the range dimension is mitigated.

d. Azimuth Compression

The data is compressed in the azimuth dimension by convolving the data with an azimuth matched filter. This operation is done in the frequency domain by taking the FFT of the azimuth matched filter, multiplying it with the FFT of the range compressed data, and taking the inverse FFT to produce the one look complex image.

For each of the three legs processed for this study, four separate complex image files of the same scene for each antenna are received from the high resolution

AIR processor. The size of these files are 750 range lines with 1024 azimuth pixels in each line. The initially processed pixel spacing are approximately 6.7 m in the viewing direction (range) and 3 m in the azimuth direction. In order to reduce speckle noise, the corresponding pixels of each set of the four files are averaged incoherently in azimuth. The resulting image from each antenna has therefore a degraded azimuth pixel size by a factor of 4, namely 12 m. These two sets of files are further registered and combined pixel by corresponding pixel to obtain a phase and intensity INSAR image. The phase of each pixel in the combined interferogram is the phase difference between the corresponding pixels obtained by the two antennas, while the magnitude image represents the product of the amplitudes of the corresponding pixels. A brief description for obtaining the INSAR images is depicted in Appendix A.

Further, the aircraft yaw and pitch, which cause sideways motion errors were subtracted from the interferogram resulting in pixel phases which represent spatial ocean surface velocity fields only.

The image processed from each flight leg (see Figure 4.5) was received from JPL on computer compatible 6250 BPI magnetic tapes. The analysis of these images was done at the Air-Ocean Interactive Digital Environmental Analysis (IDEA) Lab, which is a remote sensing image processing laboratory for geophysical data at the Naval Postgraduate School.

2. Pressure Array Data

Time series records of 2048 samples of pressure data from all four channels (sensors) were processed for the required experimental period 1000–1500 PDT. These records were examined for data gaps and signal interference. Some of the relevant recognized errors which were taken care of in the initial preprocessing by Scripps Institute of Oceanography are: *Spikes* — Any value of the time series that

is more than five times the standard deviation from the mean is considered as a spike. Spikes are replaced with the previous value in the time series. *Absence of zero crossing* — a wave time series (after detranding and demeaning) that does not cross the zero mean level for a specified number of points is considered unacceptable. *Filtering* — the tidal component is removed.

The initially processed data by Scripps Institute of Oceanography was recorded on a 9 track magnetic tape. Further data analysis was done at the Naval Postgraduate School (NPS) and described in the next chapter.

3. Lagrangian Drifter Data

Ranges from up to four Mini-Ranger shore stations were logged onboard the R/V Ricketts on a mini-computer at 5-second intervals while the vessel maneuvered slowly alongside each drifter. The positioning records indicate that vessel speeds while passing the drifters were typically less than 2 m/sec. Hence, vessel positions were measured at a spacing of 10 meters or less alongtrack (during the Group One deployments, data logging was at 10-second intervals which implies positioning data about every 20 meters alongtrack).

Times when each drifter was abeam the Mini-Ranger antenna were hand-logged for later interpolation of vessel position from the Mini-Ranger data file. The drifters always were passed down the starboard side at a distance of about 2 to 3 meters from the vessel (antenna).

Drifter positions were assumed to be the same as the vessel position, linearly interpolated between successive Mini-Ranger fixes to the time when the drifter was abeam. This procedure does introduce some uncertainty in drifter position, because (1), the drifter actually was 2 to 3 meters off the antenna position, and (2), the interpolation assumes the vessel followed a straight line during the 5 to

10 seconds between recorded fixes. However, these assumptions do not practically degrade the surface velocity estimates as discussed in the next chapter.

4. Global Positioning System (GPS) Data

A set of eleven ground points, visible in the SAR images, were selected and positioned to determine their ground coordinates in latitude and longitude. Typical points were road intersections and fence line corners. Because the pixel size on the images being used was on the order of 20[1] meters, it was felt that the positioning technique did not need geodetic survey quality precision. A single GPS receiver was used with the antenna set as close as practical to the imaged point. Once the receiver had acquired the satellites and the readings stabilized (about 15 minutes), a single position and PDOP value (precision indicator) was recorded and the equipment moved to the next point.

The GPS receiver was operated in the point positioning mode, tracking at least four satellites. It should be noted that the observations were made in early December 1989, using Block I satellites before "selective availability" was activated, which otherwise could have degraded the accuracy of this point positioning technique significantly. The standard error in ground coordinates was estimated to be 30 meters, based on prior experience using GPS for geodetic surveys in the area.

The ground coordinates obtained from the GPS receiver were latitudes and longitudes on the World Geodetic System 1984 (WGS 84) datum, essentially the same as the North American Datum of 1983 (NAD 83). Knowledge of the datum was important because the bathymetric data was provided on an earlier datum, NAD 27, and the shift between the two is significant.

[1]The rectified image is of size 1024 × 1024 pixel (see Chapter VII. B) monitored on a screen of 512 × 512 (lines × columns). Therefore, the azimuth and range pixel size are doubled (e.g., 12.1 × 2 m in azimuth) due to this constrain.

Elevations of the ground points also were needed, to compute a small correction to the range (y) pixel numbers. The elevations were scaled from a topographic map of the area, specifically the MARINA quadrangle published by the United States Geological Survey. Image coordinates for each ground control point were scaled from compressed versions of the three images. It was necessary to use compressed images in order to fit the original 1024 × 1024 pixel format on the 512 × 512 display available. The standard error in picking image coordinates was estimated to be three pixels (0.6%) on the 512 pixel format.

Of the eleven ground control points originally selected, five were discarded because of unresolved blunders, most probably mistaken identification of the ground point in the image. This left a set of six ground points to use in the adjustments. A listing of these points and their coordinates is given in Table 1, Appendix C, along with other constants pertinent to the adjustment process.

5. Summary

This chapter has described the methods, asset performance and data collection of the Wave Field and Surface Currents Marina 1989 experiment. The digital remote sensing data sets of the L-band INSAR and SAR images from the orthogonal and/or opposite legs are further processed to analyze surface currents and wavefields. These results will also be compared with conventional data sets processed from *in situ* observations of drifters and wave array data (see Chapter VII).

VII. DATA ANALYSIS METHODS AND RESULTS

A. INTRODUCTION

Methods by which the raw data were processed to obtain radar remote sensing spatial images and *in situ* temporal records were described in the previous chapter. In this chapter, the SAR and INSAR digital images are further processed to obtain two-dimensional wave number spectra of dominant waves, nearshore surface current vectors, and estimations of the decorrelation time of the backscattering ocean surface. INSAR wavenumber spectra (wavelength and direction) are compared for the first time with *in situ* wave array spectra and theoretical refraction and shoaling predictions. The INSAR measured ocean surface current field is compared with Lagrangian drifting buoys following surface currents. The results are in agreement and demonstrate the feasibility of INSAR to measure ocean surface wave spectra and currents.

B. SAR AND INSAR IMAGE PROCESSING

The SAR initial processing at JPL basically generates the two-dimensional digital image with a number of inherent geometric and radiometric distortions. Usually a number of corrections needs to be applied in order to have a correct representation of the imaged scene. The major post processing methods which were applied to the data presented in this study are described below. Digital image data sets obtained from flight paths (Figure 6.5) in the Marina experiment September 8, 1989 are presented.

1. Geometric Rectification

Since the image has equal pixel spacing in the slant range, the data have to be interpolated in order to get equal pixel spacing in the ground range format. The raw image of 750 lines (in range direction) of equal slant spacing and 1024 pixels in each lines (in azimuth direction) is first scanned to find the number of initial unprocessed lines in the image provided by JPL. Next, the meaningful nonzero lines are linearly interpolated with equal slant range pixel spacing into 1024 equal ground range spacing.

$$A'(g_j) = A(S_i) + \frac{A(S_{i+1}) - A(S_i)}{S_{i+1} - S_i}(g_j - S_i) \qquad \begin{array}{l} i = 1, 2, \ldots, 750 \\ j = 1, 2, \ldots, 1024 \end{array} \tag{7.1}$$

where $A'(g_j)$ is the new interpolated pixel value, S_i, g_j are the slant and ground range coordinates of a given pixel with a fixed azimuth coordinate before and after rectification, and $A(S_i)$ is the original pixel value centered at S_i. Since the images cover relatively small regions ($\sim$ 12 km $\times$ 7 km) the effect of Doppler shift due to the Earth's rotation which might skew the image in the azimuth dimension is not considered.

2. Radiometric Rectification

As described in the previous chapter, each image processed data set obtained from the three different flight lines in the Marina experiment consists of: two complex SAR images and two interferometric 1024 $\times$ 750 phase and amplitude images. The amplitude or brightness of the INSAR image is similar in a way to the conventional SAR image except that it was obtained by taking the modulus of the product of corresponding complex pixel images from the two antennas. The image pixel brightness I_i is a function of the reflectivity or the backscatter cross section σ of the corresponding imaged surface area

$$I_i = f(\sigma_i), \tag{7.2}$$

where $f(\sigma_i)$ is a function of the radar transmitted power, the antenna gain pattern, the effect of range attenuation, and the transfer function of the radar receiver and the post processor. For an airborne imaging radar (low altitude, small swath) it is assumed that the main contribution to brightness attenuation is the range parameter, which attenuates the two way transmitted signal by the fourth power R^{-4}. In order to mitigate this effect in the amplitude (or intensity) images, each range line is normalized in the image pixel brightness by

$$R_{Ni} = \left(\frac{R_1}{R_i}\right)^4 \tag{7.3}$$

where R_1 is the slant range to the first line and R_i is the range of line i ($i = 1, 2, \ldots, 1024$). This operation yields a more uniform brightness image in the range direction. Figure 7.1 illustrates two brightness images from the northern flight path 360° before and after radiometric rectification; the difference between the two images is clearly observed. Figure 7.2 shows a rectified brightness image from the western and eastern flight lines, legs 270° and 90°.

3. Computation of Image Coordinates

Ground coordinates for each flight path for SAR, and hence INSAR, images were found by computing parameters of a best-fit transformation between image and ground coordinates using a small set of GPS surveyed ground points visible in each image. A least-squares, minimum-variance adjustment technique was used to solve for the five parameters describing a simple rescaling rotation and translation transformation:

k'_x = pixel size scale in the azimuth direction (along track);

k'_y = pixel size scale in the range direction (cross track);

α = geographic azimuth of the flight line;

Eo = easting ground coordinate of image origin; and

No = northing ground coordinate of image origin.

Hence, the image coordinates, expressed as (x, y) pixel number pairs, were treated as an orthogonal coordinate system with constant, although different metric scales in the x and y directions, the azimuth and range directions, respectively.

A priori values for the first three parameters k'_x, k'_y, α were provided with the image data from JPL, or alternatively were computed from information provided. These *a priori* values were used as additional "observations" in the adjustment process, and were accepted as the best values for computations using image data.

Consequently, the adjustment process served two purposes. First, it confirmed that the *a priori* pixel scale sizes and flight path directions (azimuth values) were reasonably correct. Second, the adjustment estimated values for the ground coordinates of the image or origin, which was needed in order to register each image against the bathymetric data set, surface current ground truth measurements, ray traces, and station positions (Figure 7.9).

4. Interferometric Phase Images

The interferometric phase images (interferograms) are further processed to reduce the speckle noise and to obtain image pixels with equal size in azimuth and range dimension. The phase image contains the radial component of ocean surface velocity. This physical information has to be carefully preserved throughout the image; for instance, smoothing methods of the speckle noise have to consider this requirement. The extreme dark and bright pixels representing high positive and negative velocities are screened out carefully after determining the dynamic range of image pixel values. The upper and lower limits of this dynamic range is

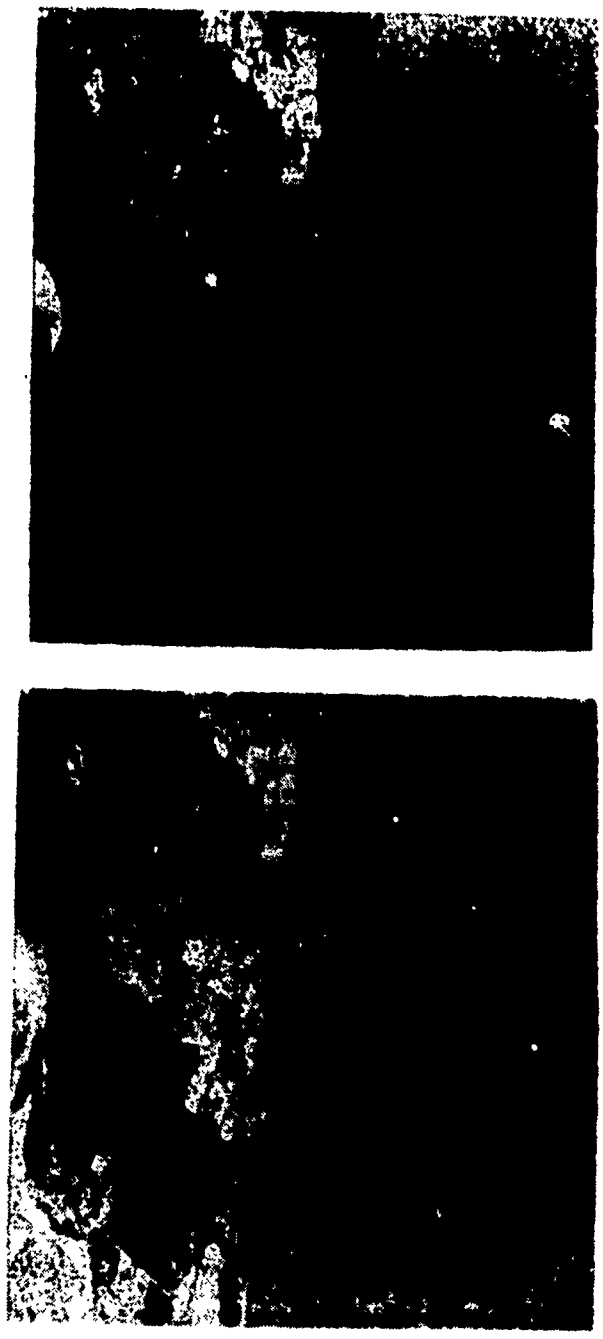

Figure 7.1: Conventional synthetic aperture radar image of the Marina Beach region in Monterey Bay; *Top*: before radiometric rectification; *Bottom*: after radiometric rectification. The aircraft attitude was Eastward (90°).

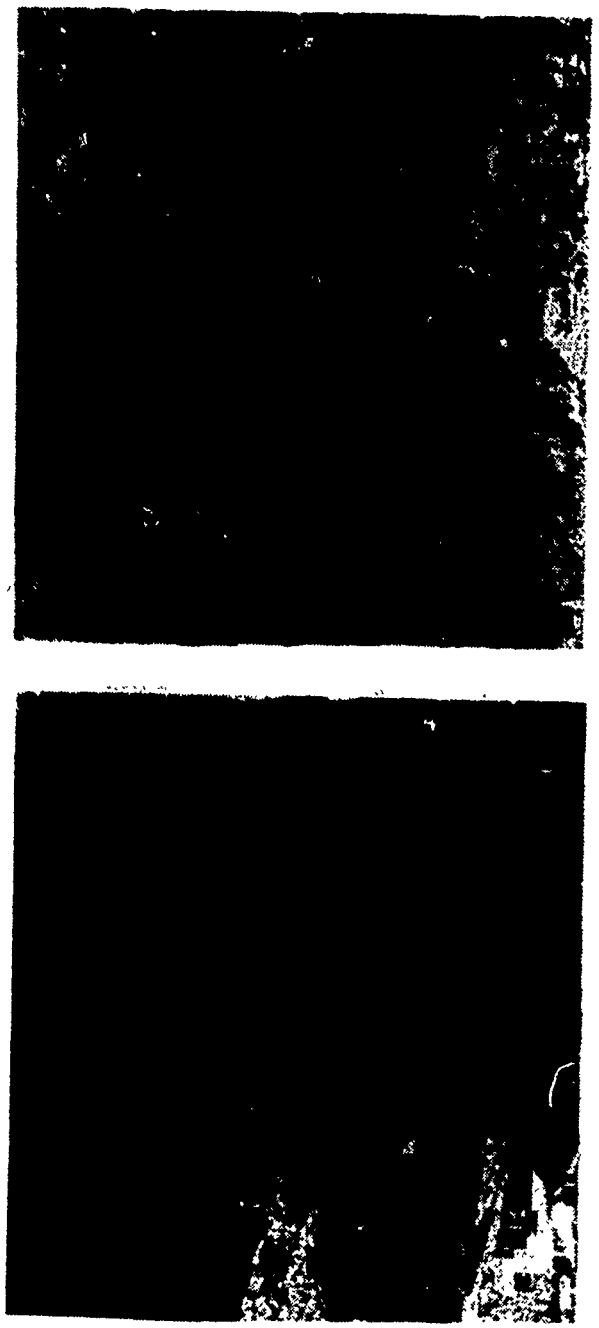

Figure 7.2: Conventional SAR image of similar area as Figure 7.1 with aircraft attitude in: *Top*: Northward (360°) and *Bottom*: Westward (270°).

determined by scanning the dark and bright pixel values over the image relative to the "normal" pixel values. Any pixel image value which is beyond or under the determined threshold is replaced by a mean pixel value of its four or eight nearest neighbors in azimuth and range dimension. The interpolation of pixels for equal size in both dimensions assists the extraction of wavenumber in the two-dimensional wavenumber spectra (see below). Figures 7.3, 7.4 are phase images corresponding to the subswaths illustrated in Figure 6.5.

C. MEAN SURFACE WIND DIRECTION ESTIMATION

Fortunately, the imaged scene in the Marina experiment included the Salinas River. The phase images (Figures 7.3, 7.4) illustrate the difference between the stationary coast and moving water surface. This contrast is significantly enhanced as compared with the conventional SAR image. The image of the coast is nearly uniform with the expected zero velocity except for the moving surface of the Salinas River. As can be seen in Figures 7.3, 7.4, and in more detail in Figure 7.5, the river is blocked off from the ocean at this time of the year and constitutes a basin of standing water in which waves are only generated by local wind with no contamination by long fetch dominant waves or advecting currents. The apparent nonzero surface velocity in this basin was measured and compared with Bragg phase velocity and wind direction. Anemometer wind measurements at the time of the radar airborne overflights taken close to the shoreline of Marina Beach at a height of 27 m show clearly an eastward wind component of almost 2 m/sec. This indicates that for leg 360° the radar was looking at upwind Bragg waves. The measured mean surface velocity obtained from the Salinas River is estimated by INSAR phase difference expressed by

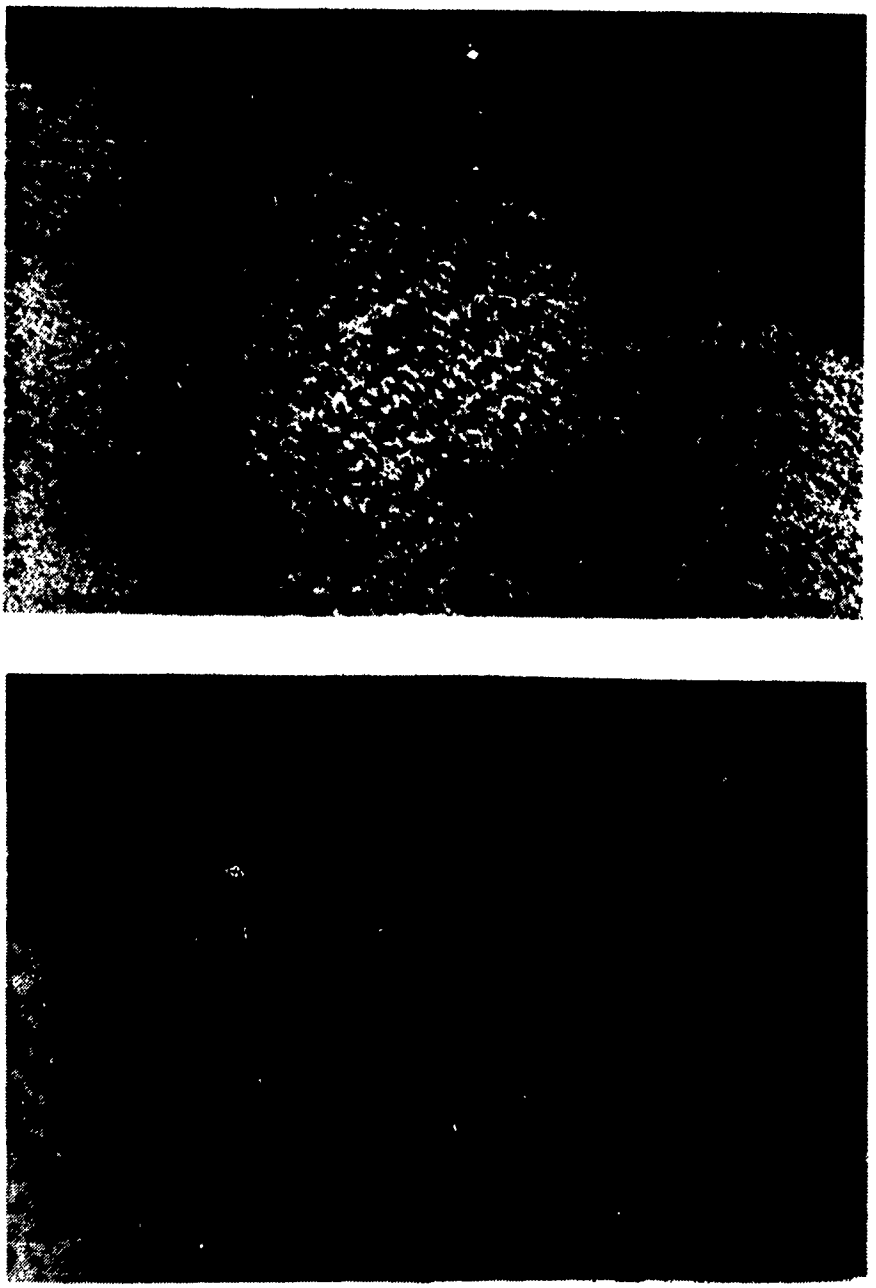

Figure 7.3: Radar interferograms off Marina Beach in Monterey Bay, September 8, 1989. Brightness represents surface motions. The aircraft flight path is from right to left along the top of the image (Northward (360°) attitude). A narrow band long crested swell from south-southwest together with a wider band wave field from north-northwest are clearly observed as they propagate ashore. *Top*: before filtering; *Bottom*: after Gaussian filtering.

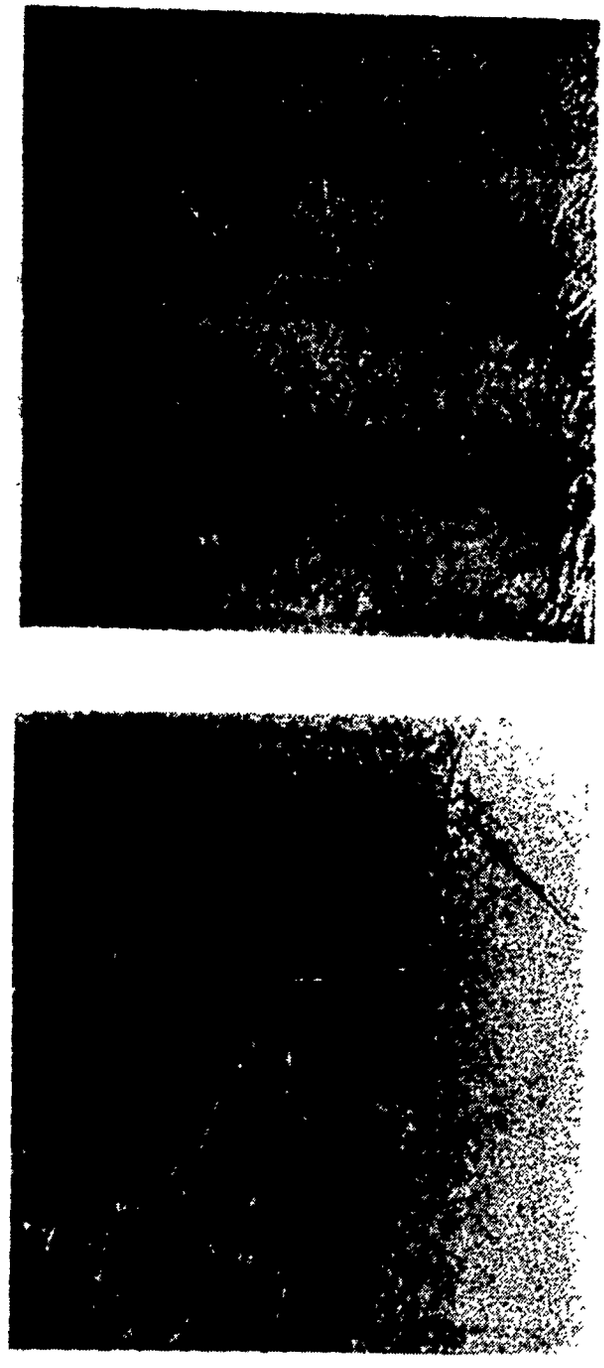

Figure 7.4: Radar interferograms of the similar area as in Figure 7.3 but for flight paths: *Top*: 90° and *Bottom*: 270°.

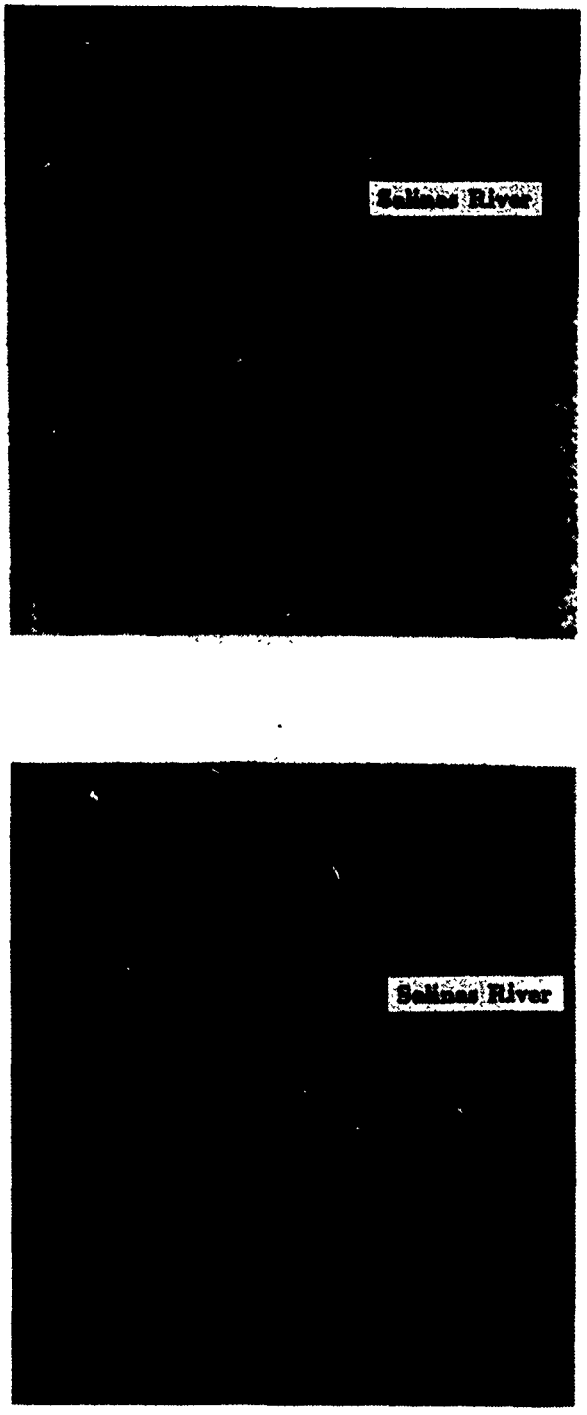

Figure 7.5: Salinas River interferograms: *Top*: for flight path 360°; *Bottom*: for flight path 270°.

$$\alpha = \frac{2\pi}{\lambda}\frac{B}{V}U_r \tag{7.4}$$

The radial velocity U_r is in this case directly proportional to the net contribution by the Bragg wave phase velocity propagating towards and away from the radar in the viewing direction. The radial component of the phase velocity contribution is rectified by the local incidence angle to obtain surface components in the range direction:

$$C_p = \frac{U_r}{\sin\gamma} \tag{7.5}$$

The phase difference α, which can vary between 0 and 2π radians, is represented by 0–255 image pixel gray shades with zero velocity at pixel value of 128. The estimated surface phase velocity C_{PSR} in the Salinas River from the image pixel values is given by

$$C_{PSR} = \left(\frac{\text{PIXVAL} - 128}{128}\right)\frac{\lambda V}{2B\sin\gamma} \tag{7.6}$$

where PIXVAL is the actual pixel image value. From linear theory, the phase velocity of a surface gravity wave is taken to be:

$$C_p = \sqrt{\frac{g}{k}} \tag{7.7}$$

Substituting the Bragg resonant condition (Equation 2.6) into Equation (7.6) results in

$$C_p = \sqrt{\frac{g}{2\pi}\frac{\lambda}{2}\frac{1}{\sin\gamma}} \tag{7.8}$$

Using Equations 7.5, and 7.7, the estimated apparent INSAR Bragg waves phase velocity is computed from two observations and compared with theoretical prediction. The results are shown in Table 7.1.

TABLE 7.1: Surface Bragg Wave Phase Velocity Estimated from INSAR Interferogram and Linear Theory Phase Velocity

Flight Path	$\overline{\gamma}$ [deg]	$\overline{C}_{PSR}$ [cm/sec]	C_{PTH} [cm/sec]
360°	46	53 ± 2	51
270°	33	$-41^1 \pm 7$	58

[1] The minus sign indicates Bragg waves propagating away from the aircraft in range direction.

Based on these results, the surface wind is infered to have had mainly an eastward component with a weaker ambiguous northerly component. The result clearly supports the assumption that in flight path 360° the radar was looking at an upwind surface roughness while in flight path 270° the radar looked at a weakly crosswind scene. This indicates that the resonant Bragg waves responsible for the radar reflectivity travelled ambiguously in both directions (for flight path 270°), towards and away from the radar, resulting in difficulties in estimating their apparent contribution to the observed radial velocity from the ocean surface.

D. CORRELATION OF OCEAN SURFACE REFLECTIVITY WITH WIND DIRECTION

The estimate of the surface wind pattern from the Salinas River interferograms (Table 7.1), are further infered regarding the mean surface reflectivity obtained from the conventional SAR amplitude images from the three flight paths. The surface wind direction as estimated in the previous section had mainly an eastward component with a weaker component southward. The image intensity, which

is a function of the backscatter cross-section of the corresponding surface, should in turn be most intense when looking upwind and weaker when looking crosswind.

Corresponding mean image intensities from the three flight paths were taken. The results are not surprising and are consistent with the estimates of the Bragg phase velocity in Salinas River.

$$\frac{\overline{I}_{360^\circ}}{\overline{I}_{90^\circ}} = 4 \div 7 \tag{7.9}$$

$$\frac{\overline{I}_{90^\circ}}{\overline{I}_{270^\circ}} = 1.5 \div 3 \tag{7.10}$$

These results clearly show that the surface reflectivity is strongest when looking upwind, weaker when the radar is looking cross-upwind, and weakest when looking cross-downwind. This might be one of the reasons for the difference in the quality of the phase images of opposite flights (90° and 270°) covering similar scenes (see Figure 7.3). The eastward 90° interferogram seems to be less noisy because the essential backscatter signal is sufficient enough to extract the phase information. The radar signal obtained from the Bragg backscattering waves is probably less than the minimum required in the 270° flight path to obtain a meaningful interferogram representing ocean surface dominant waves and currents.

E. ESTIMATION OF SCENE COHERENCE TIME

The estimation of the radar scene coherence time of the ocean surface is processed following the method described in Chapter IV. D2. Image intensities of similar subscenes obtained separately from the two antennas and from the product of the two were averaged. The scene coherence time was computed using Equation (4.61)

$$\tau_c = \frac{B}{2V}\left(-2\ln K/K_0\right)^{-1/2}$$

The scene coherence time was computed for all the three flight paths for different subscenes. The corresponding averaged subscenes were chosen from near to far incidence angle. The results are depicted in Table 7.2. For the Northern flight path (360°), the viewing ocean scene is only between 40°–50° of incidence angle; the scene coherence time first increases slightly (until 46°) and then remains almost constant. For further discussion of these results, see Chapter VIII. B.

F. AMBIENT SURFACE CURRENT ESTIMATES FOLLOWING DRIFTING BUOYS

Vessel positions were computed from the Mini-Ranger ranges using a least-squares technique called "variation of coordinates". Descriptions of the procedure can be found in most surveying texts. The presentation in Cross (1981) is virtually identical to that used in the present analysis.

Although the Mini-Ranger system computes and logs a position on line, all range data were reprocessed in order to eliminate errors caused by erratic reception from the station at MBARI RM (Table 6.6). In fact all data from that station were eventually rejected.

1. Positional Accuracy

The two-dimensional random errors in vessel position are estimated as part of the "variation of coordinates" procedure. These errors are primarily functions of the relative geometry between the ship and shore stations, and the estimated precision of a single range measurement. This random error is expressed as a variance-covariance matrix computed as follows:

$$C = \sigma_0^2 (A^T P A)^{-1} \tag{7.11}$$

Table 7.2: Estimates of Scene Coherence Time as a Function of Incidence Angle Obtained from Three Flight Paths in the Marina Experiment, September 8, 1989

Mean Incidence Angle γ	Scene Coherence Time τ [msec]		
	leg 90°	leg 270°	leg 360°
25°	136	121	—
29°	146	123	—
33°	139	134	—
36°	117	116	—
40°	121	105	119
42°	114	97	134
45°	96	95	133
48°	109	95	138
50°	112	94	140
Mean	121	109	132.8
Standard Deviation, σ	15.2	13.2	7.35

where C is the 2×2 symmetric variance-covariance matrix with the diagonal elements being the variances of easting and northing coordinates and the off-diagonal being their covariance. The quantity σ_0^2 is the "*a priori* variance of unit weight" which scales C. Practically, σ_0^2 is assumed to be unity in these computations and checked with an "*a posteriori*" estimate derived from the actual range measurements in each fix.

The matrix A, is the $N \times 2$ Jacobian for the transformation from the N-dimensional range coordinate system to the two-dimensional UTM coordinate system. In this case N typically was 3 for the ranges from reference stations WATS, HAYS, and DOP RM1 finally used (see Table 4.6).

$$A_{ij} = (X_j - Si_j)/Ri \qquad i = 1,2,3; \qquad j = 1,2; \tag{7.12}$$

where X is the ship position, Si is the i-th station position, and Ri is the horizontal distance on the UTM grid between X and Si.

The matrix P is the $N \times N$ weight matrix which is the inverse of the variance-covariance matrix for the N range observations. It is assumed the range measurements are all independent with equal variances (it is assumed here $\sigma = 3$ meters for any single range measurement). Hence P becomes a simple identity matrix times the scalar quantity $1/\sigma^2$, or $1/9$.

Because the drifters were offset from the Mini-Ranger antenna, an additional random error must be included. The offset distance was between 2 and 3 meters, but the direction was not known. In theory, the course-made-good derived from successive fixes could be used to estimate the ship's heading, and hence the direction to the drifter. However, uncertainty in direction still would be very large because of the relatively slow speeds and inherent "crabing". It was simpler to just add a circular random error of 2 meters to the variance-covariance matricies derived

above. It can be shown this is accomplished by simply increasing the easting and northing variances by 4 m^2 each.

This additional circular random error also serves to represent an uncertainty due to the linear interpolation assumption. No theoretical approaches could be found in estimating the random error in the interpolation, however, based on simulation runs, the maximum error due to interpolation between fixes of 10 m apart would be about 2 m.

In Appendix D, the variance-covariance matrices computed for each observation of drifters from Group One and Two are presented. Only one matrix was computed for each group of observation because the drifters were so closely bunched that the relative geometry did not change significantly and hence, the random errors were essentially the same for all.

In general, errors increased slightly closer towards the shore. Circular errors increased from about 11 m to 13 m (CE 95%), going from the most offshore positions where Group One was deployed to the nearshore area where Group Two was recovered. Also note that the northing coordinate was determined more precisely than the easting, by a factor of about 3. Both effects are due to the fact that the reference shore stations lay essentially along a north-south line passing close to the experiment region.

2. Accuracy of Velocity Estimates

Drifter velocities were computed by the difference of positions divided by time interval. Standard error propagation techniques were used to estimate a variance-covariance matrix for the U and V velocity components. The reader is refered to the MATHCAD documentation for a description of the math and the actual computation of the estimates given below.

The error estimates of the sorted data are small, of the order of 0.1 cm/sec as shown in Table 7.3. The errors depicted are small primarily because of the relatively long time intervals between drifter position observations, typically about 40 minutes. The relatively large time period of drifter positioning is allowable since the environmental conditions on September 8, 1989 were almost steady for this time interval. Also note that these error estimates assume that U and V components are constant over the period between drifter positionings. In other words, these are estimates of the error in the mean velocities.

TABLE 7.3: Standard Deviation of Velocity Components (cm/sec)

		σ_U	σ_V
Group One:	Obs 1 to 2	0.13	0.08
	Obs 2 to 3	0.19	0.11
	Obs 3 to 4	0.22	0.12
Group Two:	Obs 1 to 2	0.14	0.07
	Obs 2 to 3	0.20	0.10

G. INSAR MEASUREMENT AND GROUND TRUTHING OF NEARSHORE OCEAN SURFACE CURRENTS

INSAR phase images (Figures 7.3, 7.4) were further processed to obtain estimates of very near ocean surface currents. The radial component of surface velocity U_r of each pixel is rectified from the incidence angle dependence resulting in the horizontal component of ocean surface velocity in the viewing (range) direction. The bias introduced by the Bragg wave phase velocity estimated from the Salinas River

(see Chapter VII. C) is then subtracted. The resulting phase image is averaged two-dimensionally to mitigate the quasi-periodic wave orbital velocity. The scale of averaging is the orbital motion scale of the largest observed wave. All smaller wave multiples of this scale are averaged out. The surface velocity image from one flight path represents only one component of the surface current vector in the viewing direction. Two orthogonal flight paths observing the same area are needed to estimate the full current vector. The phase image data from flight paths 360° and 90° were selected to obtain interferometric virtual estimates of ocean surface current fields. These estimates are compared with simultaneous observations of the Langrangian floating drifters, and good agreement is obtained.

1. Additional Considerations and Processing

When computing current estimates from INSAR phase images, the following additional considerations were taken:

- When using the interferometric SAR technique to measure surface velocities, one has to consider sideways motion of the antennas, introducing a phase shift making the imaged scene appear to move when it is stationary. The prominent errors in the image phase data were corrected at JPL (see Chapter VI. F) using the Inertial Navigation System (INS) data and land imagery as a stationary reference (Goldstein et al., 1989).

- Mini-Ranger positions of the floating drifters were transformed to image pixel coordinates using the GPS adjustment method (see section B3). Image subareas from flight paths 90° and 360° containing the observed path of the Lagrangian drifters were selected to match the current estimates as spatially similar in nature as possible to the *in situ* observation.

- The image constructed from the 360° flight path looking upwind is less noisy compared with images constructed from flight paths 90° and 270° looking crosswinds (see section C, D). Therefore, prior to the computation of current estimates, the phase image from the eastward flight path was smoothed. Pixel phase values, which deviate by more than two standard deviations from the mean phase value of a selected subarea, were rejected, resulting in a less noisy phase image for current computation.

An additional problem is the appearance of slicks (seen as dark regions in the conventional SAR amplitude image, Figures 7.1, 7.2) in the selected area. In these areas the essential backscattering amplitude is probably too weak, i.e., very noisy, to extract a reliable interferometric phase due to surface motion. Nearby regions with no slicks were selected to compute current estimates for areas observed by drifters 3, 4.

2. Comparison of INSAR Current Estimates with Lagrangian Drifter Measurements

The simultaneous *in situ* surface current estimates are shown in Figure 7.6. Three groups of five Lagrangian drifters each were deployed close to the time of INSAR aircraft overflights (see Chapter VI. C). Radar data was initially acquired 30 minutes before the predicted time of maximum flood tide current (1320 PDT). This timing was predicted on observing the stronger flows to make the current estimates more reliable in an area (Marina Beach) which is known to have unpredictable weak tidal currents.

The Lagrangian drifters (Figure 7.6) experienced a dominant eastward component and a much weaker northward component. Some estimates of surface current derived from interferometric SAR data and Lagrangian drifters are tabulated in Table 7.4. It is shown that the dominant eastward components are in better agree-

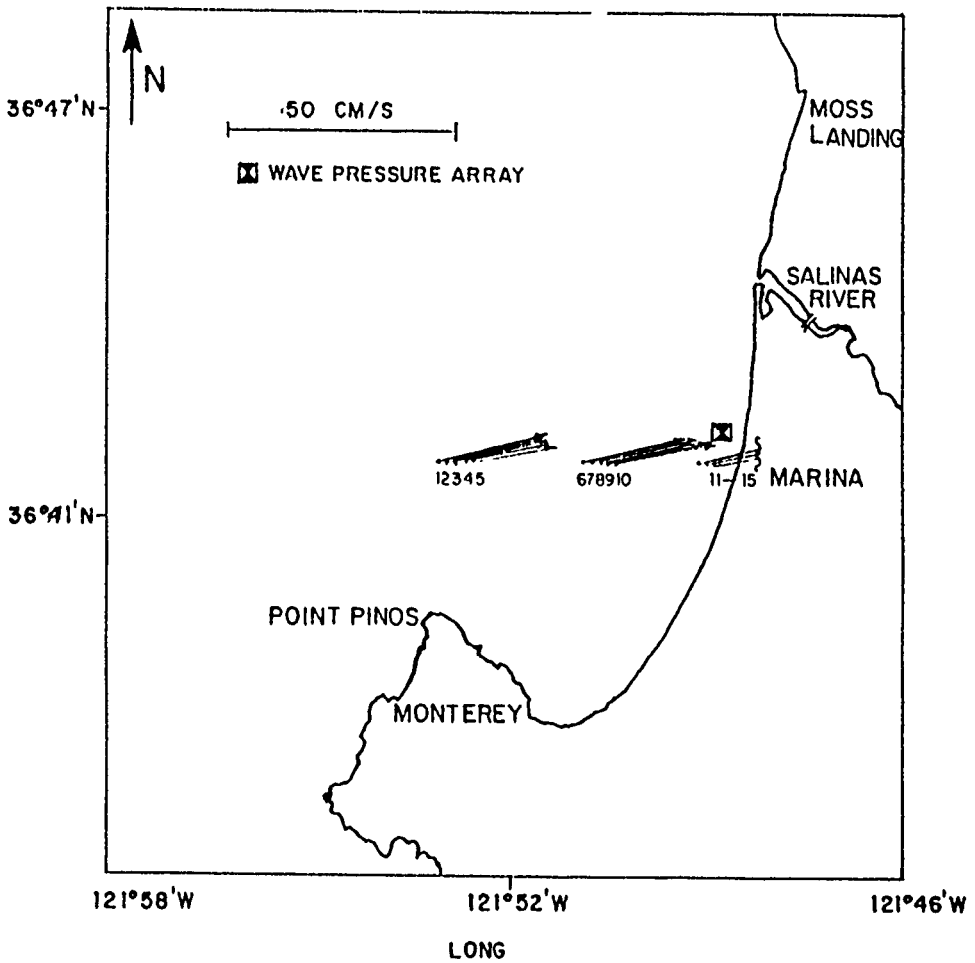

Figure 7.6: Direct observation of surface currents following Lagrangian drifters near Marina Beach in Monterey Bay, California. The arrows point in the direction of the current and the length of each arrow is proportional to the observed speed.

ment (correlation 0.9) than the weaker and hence, difficult to determine, northward component (correlation 0.5). The velocity magnitudes are most consistent with a correlation of 0.94. The reasons for these results are assumed to be associated with the physical difference between the two types of measurements, Lagrangian versus spatial synoptic observation, and are further discussed in Chapter VIII. C.

The drifter velocity estimates with almost nil standard deviations (σ_u = 0.18 cm/s, σ_v = 0.1 cm/s) were discussed in the last section. The INSAR measurements had a larger standard deviation of 20-30 cm/sec computed from selected

TABLE 7.4: INSAR Estimates and *In Situ* Observation of Ocean Surface Currents (in cm/sec). Subscript d Denotes Drifter and s for INSAR.

Drifter Number	Zonal Component		Meridional Component		Velocity Magnitude	
	u_d	u_s (360°)	v_d	v_s (90°)	U_d	U_s
1, 2	20	–	5	–	21	–
3, 4	18	15	5	4	19	16
5	18	16	4	5	18	17
6, 7	22	17	5	9	23	19
8	21	17	5	8	22	19
9, 10	22	18	4	5	22	19
Average	20	17	5	6	21	18
rms error (cm/sec)	0.5		1.7		0.5	

subareas, which were averaged to estimate INSAR current components. This large velocity deviation is believed to be primarily associated with the orbital velocity of the quasi-periodic surface gravity waves which are averaged out. To get an estimate of the order of magnitude of this assumption, consider a a deep water surface gravity wave propagating in the cross-track (range) direction of a moving radar platform. For this geometry, the observed radial component is the actual wave orbital velocity. For waves propagating in the along track (azimuth) direction, only the vertical particle velocity is observed. Therefore, the largest observed orbital velocity in deep water is given by

$$\mathrm{U}_{OB} = \frac{H}{2}\frac{gT'}{L} \tag{7.13}$$

where H is the wave height. The orbital velocity of a shoaling wave increases with decreasing wavelength; hence, the expected dominant contribution to the observed

mean orbital velocity is from the shorter observed swell component (see Chapter IV. C).

For a wave with $L = 97$ m, period $T' = 9.1$ sec and a rms wave height $H_s = 0.32$ m (the wave height and period are estimated from the *in situ* power spectrum, see Figure 7.10) as observed in the Marina experiment, $U_{rOB} = 0.20$ m/sec. This result is consistent with the computed standard deviation from the estimated mean surface currents. It indicates that most of the contribution to the standard deviation is from the quasi-periodic orbital velocity of dominant waves which are averaged out. Additional contribution to the standard deviation of the mean surface current component estimates is attributed to speckle noise. Estimates of current velocity vectors for radar and direct observed measurements are shown in Figure 7.7. The agreement is felt to be encouraging. For further discussion on these results, see Chapter VIII. C.

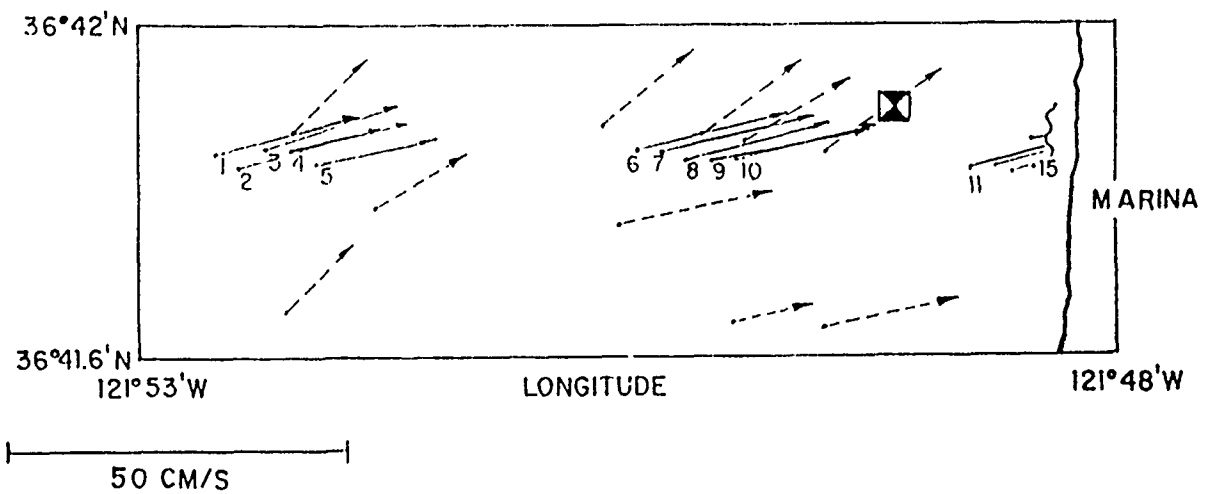

Figure 7.7: Detailed presentation of Figure 7.6 together with INSAR current estimates (dashed arrows).

H. OBSERVATION OF SPATIAL AND TEMPORAL NEARSHORE OCEAN WAVE SPECTRA

Shoaling and refraction of waves can be characterized by two dimensional spectral analysis. The two-dimensional wavenumber ($\mathbf{k} = (k_x, k_y)$) spectra obtained by INSAR imagery are tested against the conventional measurement of directional spectra computed from time series records obtained from the pressure wave array in the shallow water off Marina Beach. In addition, the two swell components observed by the shallow water array were used as inputs to compute wave ray traces using Dobson's numerical model (see Chapter V. B). Two-dimensional INSAR wave number spectra were computed for subscenes along the ray traces. The results are consistent with the refraction model outputs and with the shallow water array directional spectra.

1. INSAR Two-Dimensional Wavenumber Spectra

Following the description in Chapter V. C, a software package was developed to calculate two-dimensional wavenumber spectra from INSAR images.

The rectified phase images illustrated in Figures 7.3, 7.4 were further processed by linear interpolation (see Equation 7.1) to equalize the azimuthal pixel size with the range size resulting in square pixels. This operation was done to simplify the computation of the wave lengths and directions of the peaks of the wave number spectra.

Due to the complex shallow water region in which the experiment was conducted, relatively small subscenes had to be selected to fulfill the homogeneity requirement for spectral analysis. Trade off is between satisfying the requirement of homogeneity and obtaining confidence in the spectral estimates. To obtain confidence in the spectral estimates, a minimum sea surface area equivalent in size to approximately 6–10 wavelengths on a side must be used to calculate INSAR image

spectra to provide reasonable estimates of wavelength and direction. Therefore, a flexible 2D FFT code was developed which allows a selection of any number of pixels in either dimension resulting in rectangle sub-areas for spectral analysis of any size. If the number of pixels in the sub-area is not a power of 2, the sub-area is zero paded to the nearest power of 2 number of pixels. This increases artificially the effective resolution for wavelength and angle computations. The edges of the subscenes were cosine tapered to reduce spectral leakage and demeaned. Figure 7.8 shows some of the sub-areas that were subjected to spectral analysis. The INSAR image spectra of the corresponding sub-areas are illustrated in Figures 7.12 to 7.15. They are smoothed with a Gaussian smoothing kernel providing spectral estimates with 25–30 degrees of freedom.

2. Shallow Water Array Directional Spectra

Computation of shallow water array directional spectra was done using the Grauzinis (1989) method (see Chapter V. C). The available Fourier coefficients of the wave field angular distribution function were computed using Equations (5.31)–(5.35). The model distribution function that was used to match the Fourier coefficients is the wrapped Cauchy distribution

$$D(\theta) = \frac{1}{2\pi}\left\{\frac{1 - m_1^2}{1 - 2m_1\cos\theta + m_1^2}\right\}$$

This distribution gives suitable narrow estimates and allows for bimodal directional spectra.

The spectral analysis was performed for a one hour time series 1200–1308 PDT on September 8, 1989 with subsequent FFT's computed over 128 second intervals with a sampling rate of 0.5 Hz. The averaged spectral estimates have approximately 64 degrees of freedom. As mentioned in Chapter VI. F2, the data were detrended and demeaned before being Fourier transformed to eliminate contamina-

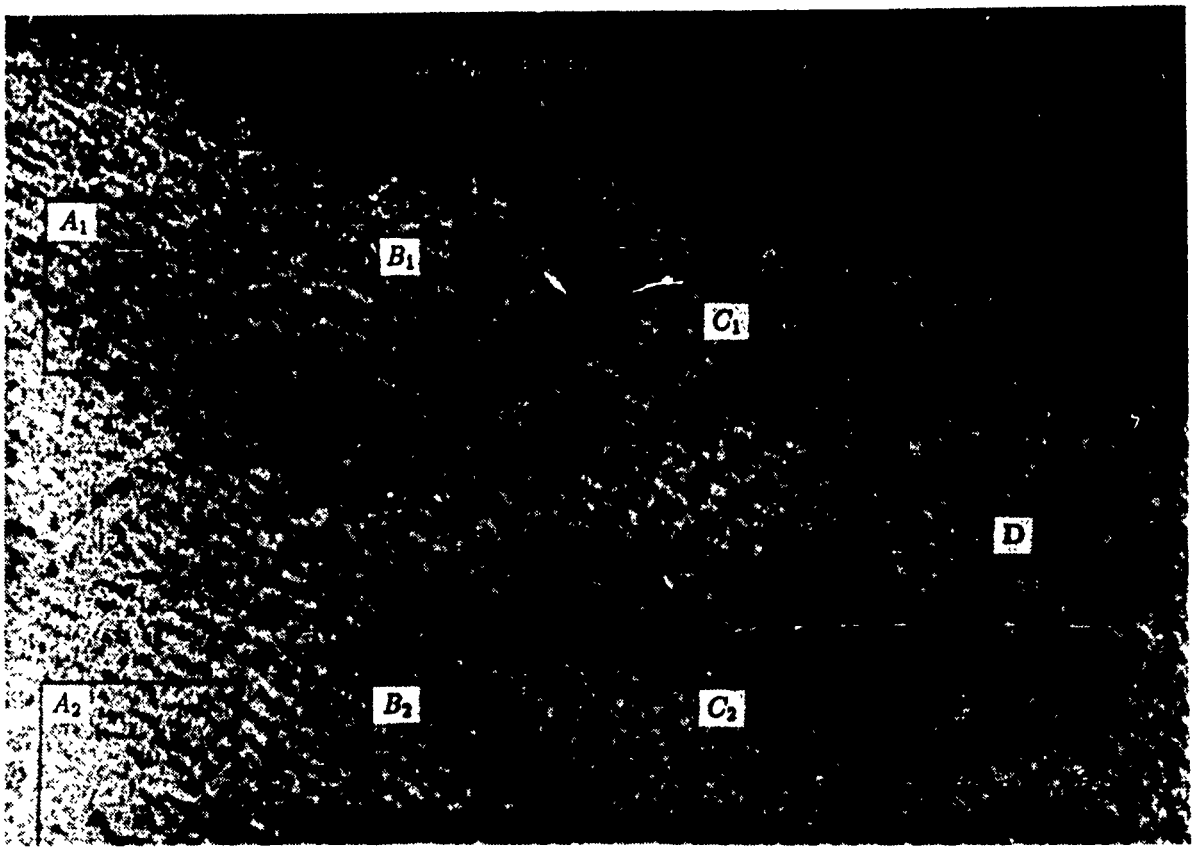

Figure 7.8: Radar interferogram of Marina Beach area, September 8, 1989. The indicated sub-areas were subjected to spectral analysis with results appearing in Figures 7.12–7.15.

tion of the wave frequency bands due to leakage of low frequency signals. The wave pressure power spectrum is calculated and transformed into surface elevation and surface slopes spectra by applying linear wave theory transfer functions as described in Chapter V. C, and subsequently converted from a frequency angle presentation to a directional wavenumber presentation via intermediate water linear wave equations.

3. Comparison of INSAR 2D Wavenumber Spectra with Temporal Wave Array Spectra

Wave refraction rays for the two dominant waves observed by the Marina shallow water array were constructed using the Dobson model. The rays at these peak frequencies (0.063, 0.109 Hz) were propagated offshore. The predicted

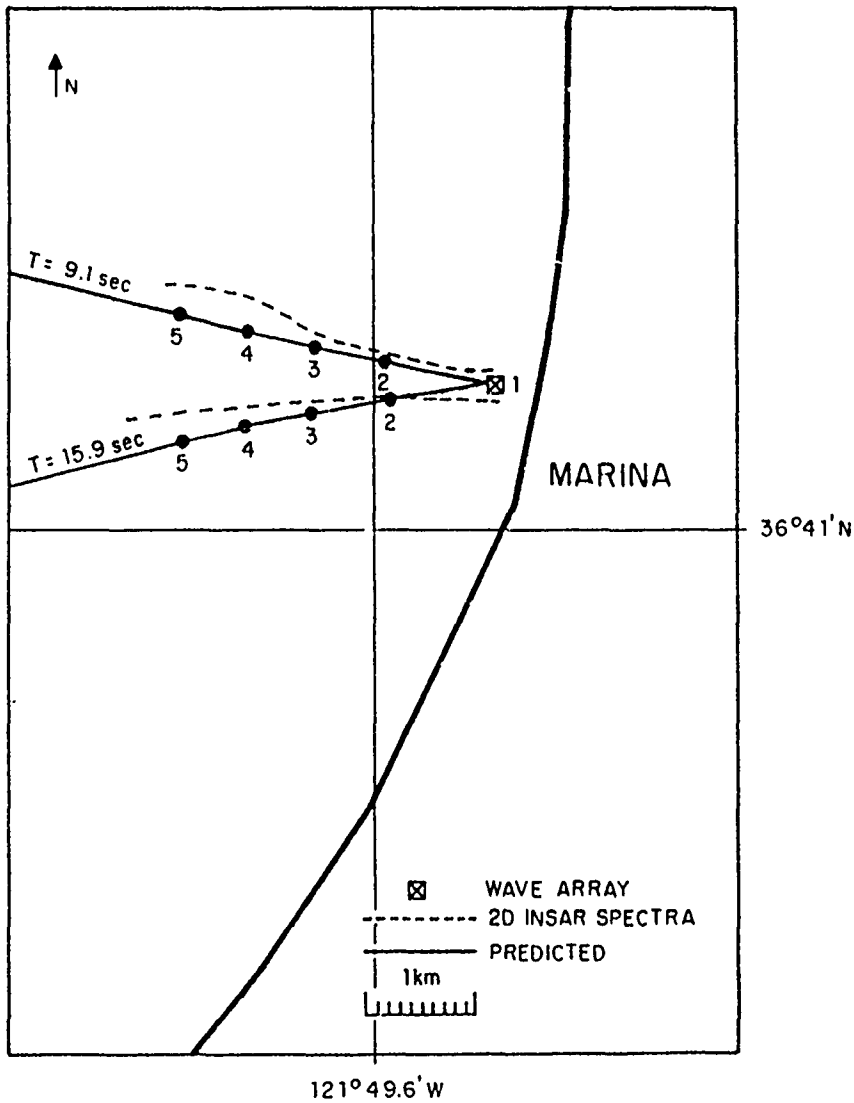

Figure 7.9: Observed ray traces — from INSAR spectral analysis versus predicted wave orthogonals for the two swells measured by the shallow water array of Marina Beach. The numbers are the centers (stations) of the 2D FFT sub-areas.

Table 7.5: Actual INSAR 2D Wavenumber Wave Array Spectra Results and Predicted Refraction and Shoaling Data

Station	Mean Depth (m)	INSAR 2D FFT				Predicted and Buoy Data				Comments
		L_1 (m)	$\alpha_1(°)$	L_2 (m)	$\alpha_2(°)$	L'_1 (m)	$\alpha'_1(°)$	L'_2 (m)	$\alpha'_2(°)$	
1	16	96	291	192	256	98	283	192	260	L', α' measured by wave array
2	27	110	282	250	252	116	286	241	257	L', α' from model prediction
3	39	125	288	283	265	124	287	280	255	– " –
4	52	135	301	310	264	127	288	306	253	– " –

wavelength and direction along the refracted ray (about every 800 m) were compared with the actual wavelength and direction of the two dimensional INSAR image wavenumber spectra from the Northern (360°) flight path image (see Figure 7.8). The analysis is summarized in Figure 7.9 and Table 7.5.

The effects of tides and coastal currents on wavelength and propagation direction were ignored and considered negligible when constructing the ray traces. The comparison between the predicted and INSAR results clearly demonstrate the feasibility of INSAR in imaging ocean wave spectra in a complex region under the given experimental environmental conditions.

An inherent limitation in applying the refraction model to INSAR's data is that the bathymetry used in the model is not as accurate as would be desired. The density of depth data varied based on various ship tracks and was available only every 6 seconds.

The *in situ* wave array spectral results are more reliable for comparison with INSAR's measurements. The surface elevation power spectrum obtained by the wave sensors is illustrated in Figure 7.10. The two observed peaks in the spectrum correspond to wave periods of $T_1 = 15.9$ sec and $T_2 = 9.1$ sec. The wavelengths (Station 1, Table 7.5) are calculated at the appropriate sensor depth (16 m) using the linear wave dispersion relation (Equation 5.3). The higher energy region around the short wave peak (T_1) shows a range of spectral average (0.1 to 0.17 Hz), while the region around the lower energy peak (T_2 long swell) is much narrower; thus, the spectrum indicates the existence of two swells with the shorter wave field having a broader spectrum.

The directional wave spectrum computed using the exact Fourier coefficient representation method (Grauzinis method) is presented in Figure 7.11. The shorter wave field propagates from west-northwest to east-southeast, while

the longer swell propagates from south–westsouth to east–northeast. The wavelength estimates from the spectral analysis of the two data are identical while the directions are in good agreement (see Table 7.5).

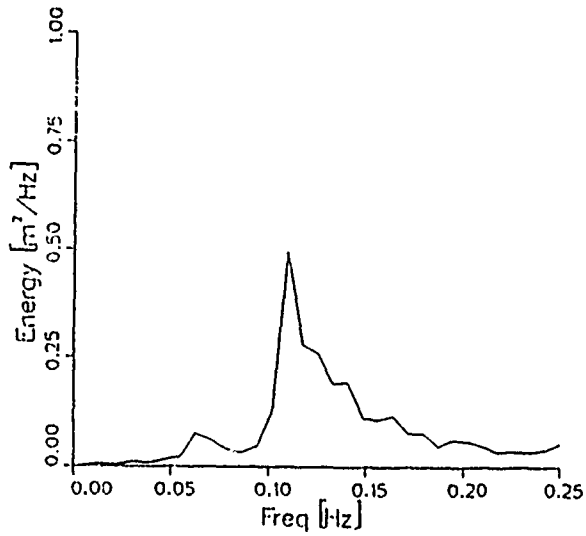

Figure 7.10: ***In situ*** **surface elevation power spectrum measured by the Marina shallow water array on September 8, 1989, 1200–1308 PDT, at a depth of 16 m.**

In order to reduce bathymetric constraints, two typical sizes of image sub-areas were selected for computing the 2D wavenumber spectra. For the shorter wave field, sub-areas of $\sim 1400 \times 700$ m were selected for computing wavelength and direction depicted in Table 7.5, while for the long crested swell sub-areas of $\sim 1400 \times 1400$ m with overlap between the sub-areas were used. The variation of bottom topography over the subscene changes the wavelength and direction. This distortion is reflected in the 2D wavenumber spectra. Table 7.5 illustrates the 2D wavenumber spectra of INSAR along the ray traces depicted in Figure 7.9.

The computed spectra (Figures 7.12–7.15) illustrates shoaling and refraction of the two dominant swells over a wide imaged region ($\sim 12 \times 6$ km). For

region A, B where the ocean is relatively deeper, shoaling and refraction are less pronounced compared to the southern regions C, D.

In spite of the limitations mentioned above, INSAR image spectra verified by wave array measurement and compared with model predictions are encouraging, and demonstrate the feasibility of this unique technique to estimate ocean wave spectra even in a complex oceonographic region. For further discussion, see Chapter VIII. D.

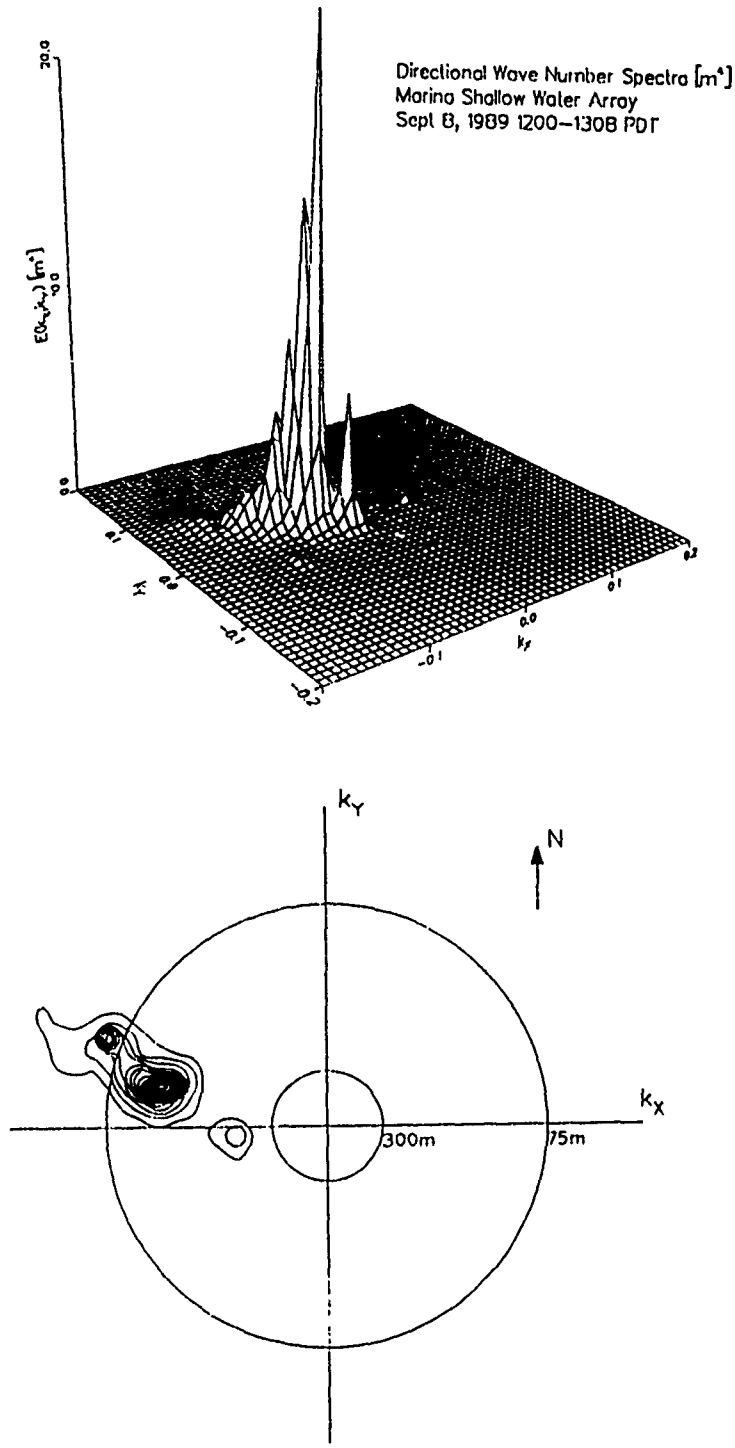

Figure 7.11: *In situ* directional wave spectrum taken at Marina Beach for the same time interval as Figure 7.8; *Top*: 3D representation; *Bottom*: contour presentation.

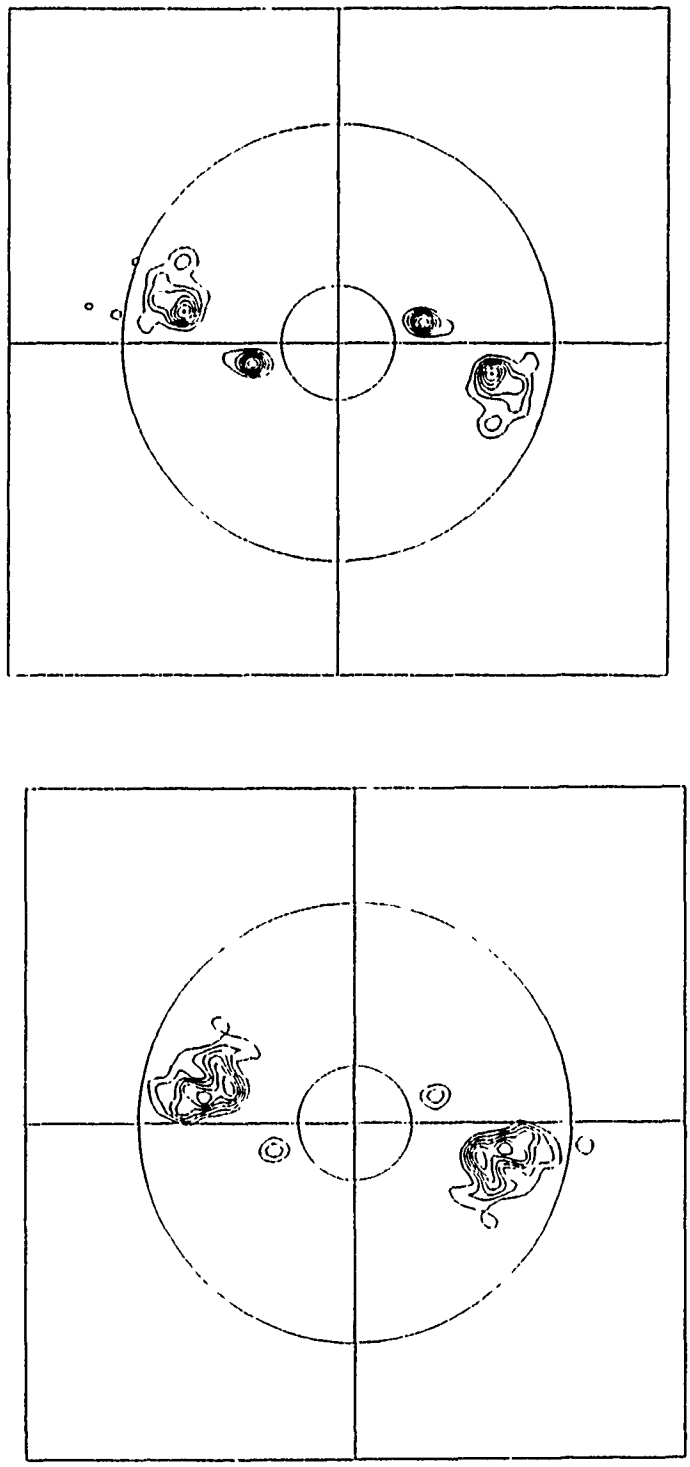

Figure 7.12: *Top*: Shallow and *Bottom*: deeper water INSAR image wavenumber spectra of sub-area A1, A2 indicated in Figure 7.8. The circles represent wavelengths as depicted in Figure 7.11.

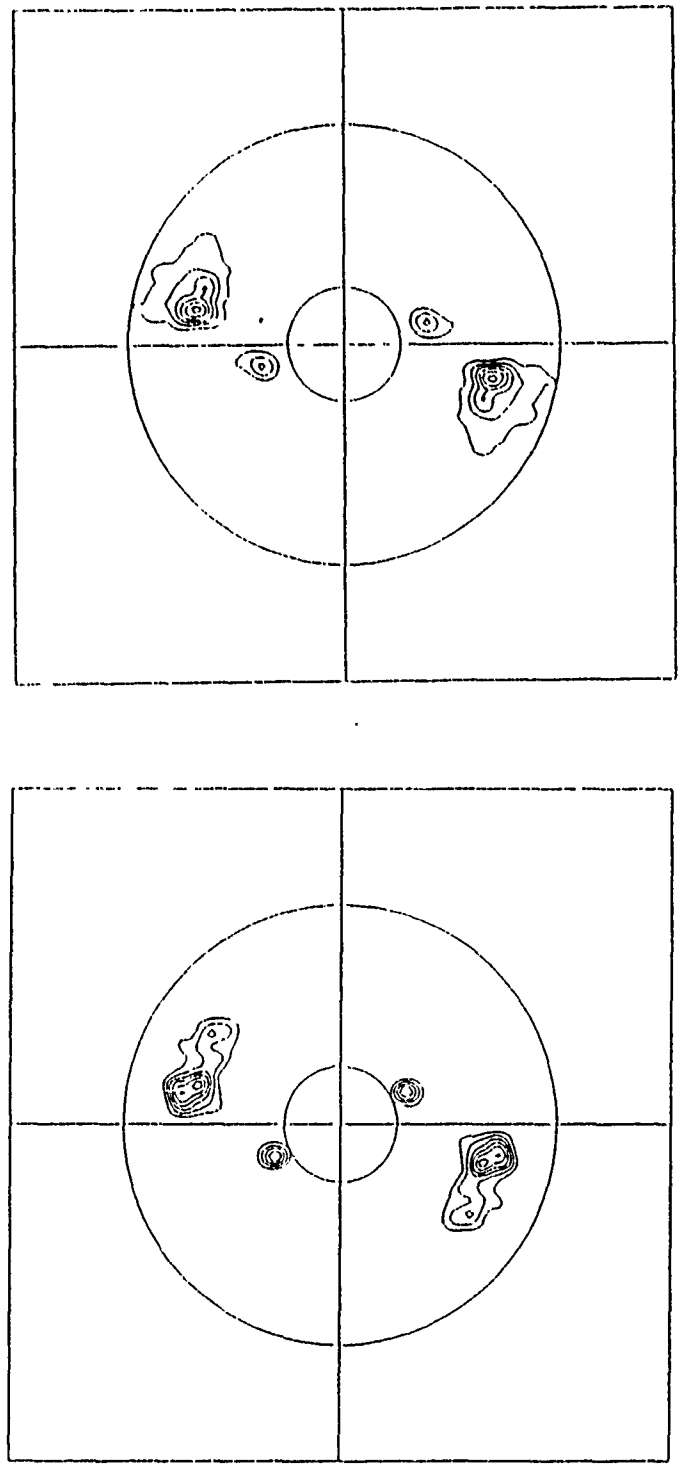

Figure 7.13: Same as Figure 7.12, but for sub-area B1, B2.

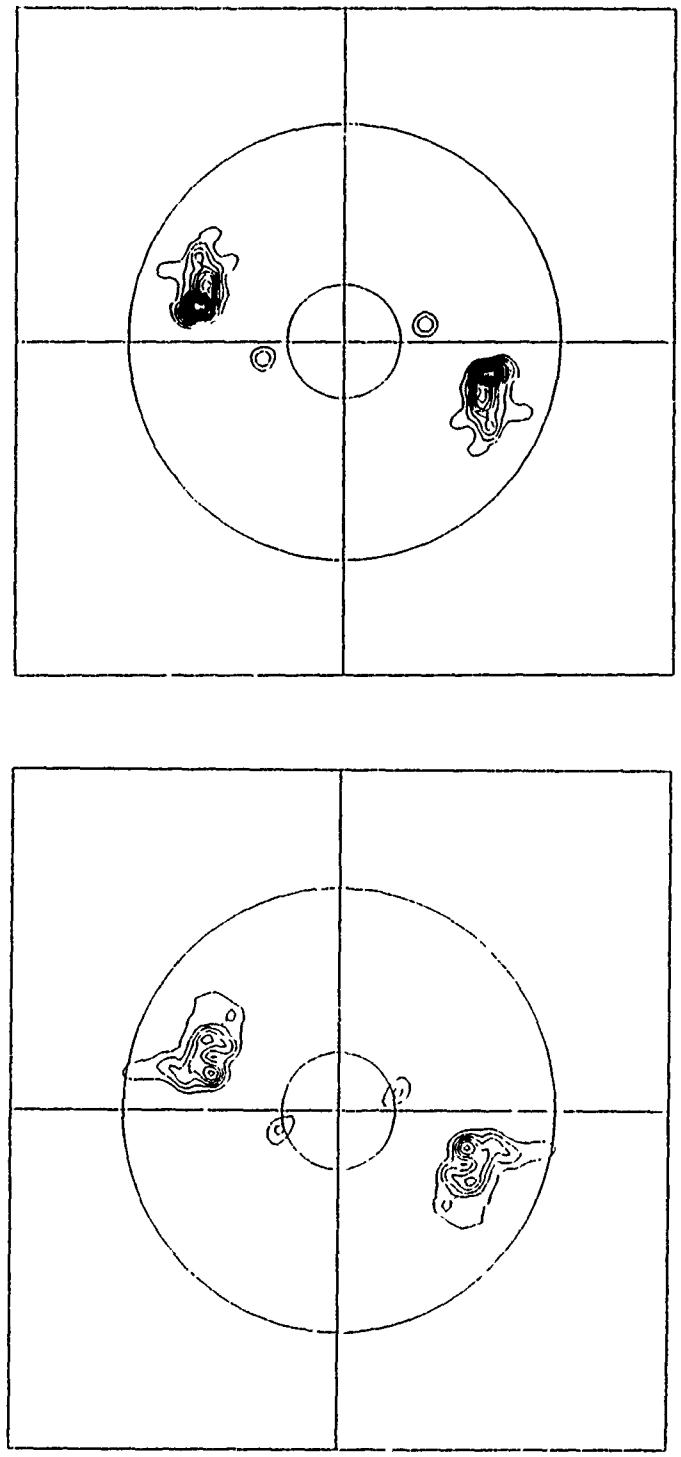

Figure 7.14: Same as Figure 7.13, but for sub-area C1, C2. The top image spectra is obtained from a sub-area close to the Marina shallow water array.

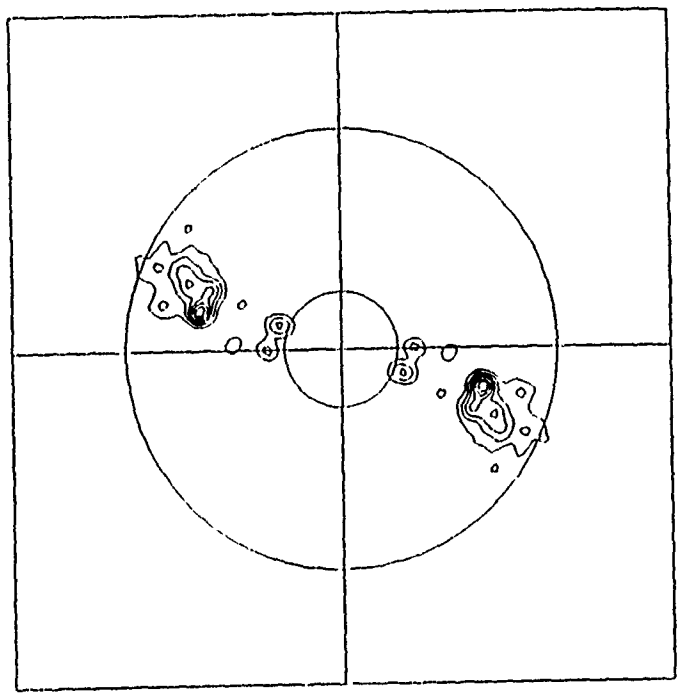

Figure 7.15: INSAR image spectra of sub-area D indicated in Figure 7.8. The excessive refraction of the long crested swell in this region smears the spectra.

VIII. RESULTS AND DISCUSSION

A. INTRODUCTION

The aim of the experimental part of this study has been to verify the capabilities of INSAR to image near surface ocean dynamics. The method was to compare ocean wave spectra and surface current measurement obtained remotely by INSAR with conventional *in situ* observations.

A discussion of the processed results from Chapter VII is presented in this chapter. It is shown that the interferometric technique appears to offer considerably improved imagery of ocean surface waves as compared to conventional SAR. The additional capability relative to SAR, in imaging ocean surface currents, seems to be reliable for oceanographic studies.

B. TEMPORAL RADAR COHERENCY OF THE OCEAN SURFACE

The fluctuations in the short wave reflectivity of the ocean surface during a given observation time causes the temporal correlation function of its reflectivity to have a width τ_c. The azimuth resolution ρ_{az} is degraded as compared to that of a stationary scene (see Equation 3.2) to

$$\rho_{az} = \frac{\lambda}{2\beta}\left[1 + \left(\frac{\beta R}{V\tau_c}\right)^2\right]^{1/2} . \tag{8.1}$$

In addition to the degradation in azimuthal resolution due to finite scene coherence time, the SAR (and hence INSAR) azimuthal resolution is smeared also by dominant wave motions. The azimuthal wave pattern translation and the range component of the wave acceleration during the integration time primarily degrades the azimuthal resolution. For an imaged swell, the wave pattern translation smearing

can be corrected by focus adjustment of the processing matched filter (Raney, 1980) and therefore will not be discussed further. As was noted in Chapter IV. C, the finite scene coherence time determines the effective integration time and hence the azimuthal resolution. The L-band radar scene coherence time estimation from image intensities (Chapter VII. E, Table 7.2) is of the order of $O(10^2)$ msec.

The range component of acceleration of a deep water gravity wave is given by

$$a(\mathbf{x},t) = 2H\left(\frac{\pi}{T'}\right)^2 \exp\left[\frac{2\pi z}{L}\right] \sin(\mathbf{k}\cdot\mathbf{x} - \omega t)\ \cos\gamma \tag{8.2}$$

where H is the wave height, T' is the wave period, and z is the water depth. At the surface $z = 0$. The degradation in azimuth resolution due to wave acceleration is taken to be (Alpers and Bruening, 1986)

$$\rho_{az} = \frac{\pi}{2}\frac{R}{V}\, a_{\mathbf{r}}(\mathbf{x},t)T = \frac{\pi}{2}\frac{R}{V}\, 2H\left(\frac{\pi}{T'}\right)^2 \sin(\mathbf{k}\cdot\mathbf{x} - \omega t)\ T\ \cos\gamma \tag{8.3}$$

For typical JPL/DC-8 parameters, wave height of 0.7 m, wavelength of 100 m, effective integration time of 0.1 sec. and incidence angle of 30°, $\rho_{az} \cong 0.7$ m. Therefore, the degradation in azimuth resolution due to long wave acceleration is neglected.

It is important to note once again that the loss in azimuthal resolution due to finite scene coherence time associated with the random motion of scattering elements within the resolution cell, results in a consistent azimuth image smear and not defocus, and is therefore not recoverable by focus adjustment or integration time settings (Lyzenga and Schuchman, 1983). Therefore, the estimation of scene coherence time remains a key parameter in determining the azimuthal cutoff wavelength of SAR and INSAR azimuthal resolution. If the coherence time τ_c is much smaller than the post processing integration time T, the azimuthal resolution can

be approximated (Lyzenga and Shuchman, 1983) to be:

$$\rho_{az} \approx \frac{\lambda R}{2V\tau_c} \tag{8.4}$$

Based on the results depicted in Table 7.2 and Equation (8.4), the degradation in azimuth resolution due to finite scene coherence time for the three flight path images in the Marina experiment is illustrated in Figure 8.1.

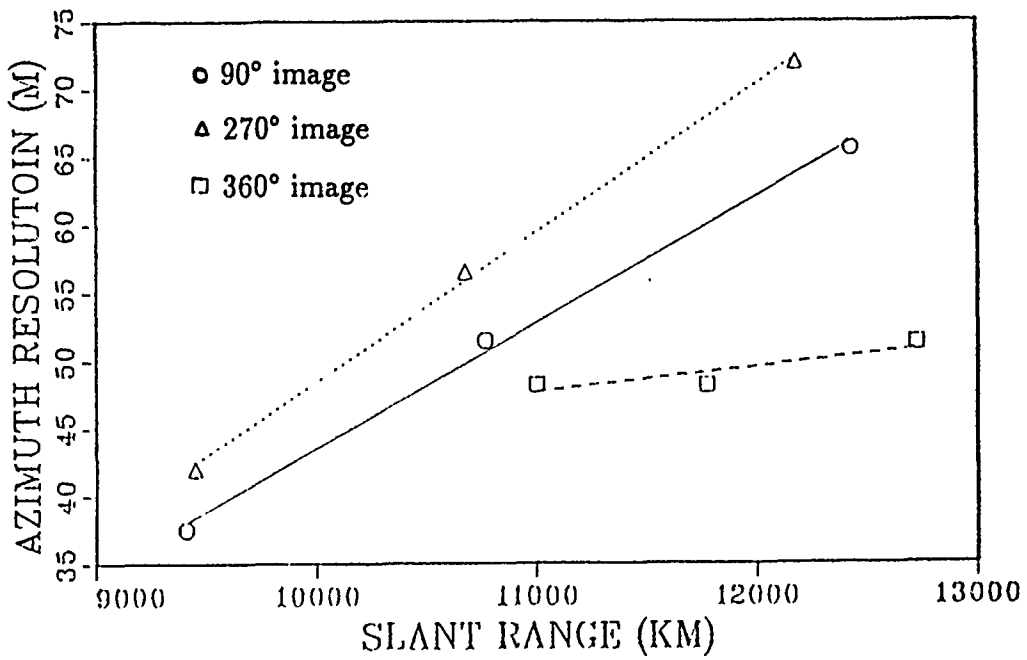

Figure 8.1: Degradation in azimuth resolution for the NASA/JPL DC-8 L-band SAR for the three flight path images in the Marina experiment, September 8, 1989.

These estimates of L-band scene coherence times are consistent with conventional radar observations (100 msec) during the TOWARD experiment (Plant and Keller, 1984). The theoretical estimates of the scene coherence time using the Pierson-Moskowitz spectrum (Table 4.1) gives larger estimates (3–4 times) compared with the more realistic direct observation estimates. The estimates of the ratio K/K_0 in Equation (4.61) for all three flight path images were close to 0.9 and

larger. This result suggests that for the estimation of the scene coherence time *only*, the measurement sensitivity can be increased by increasing the effective baseline separation (9.9 m) between the antennas. Variation of the effective baseline separation will allow to investigate the distribution of the temporal correlation function which was assumed to be Gaussian in the present study.

For rougher sea state, it is expected that the observed scene coherence time will be shorter. This is because the waves become steeper with higher orbital velocities resulting in a larger velocity spread of the scattering elements. When breaking occurs, the backscattering mechanism is specular in nature (not Bragg). The backscattering slopes are propagating at the dominant wave phase velocity (Lyzenga et al., 1983). The transformation of the advecting velocity of the backscattering surfaces, from orbital to phase velocity when breaking occurs, further reduces the scene coherence time. A cusped region is the surf zone, the estimated scene coherence time from this region is 30% less relative to estimates from nearby sea surface regions with similar incidence angle.

The difference in azimuth resolution between three flight path images is not fully understood at the moment and is probably determined by the speckle and random noise and look direction (upwind crosswind). Based on the estimates of azimuth resolution (40–70 m) in Figure 8.1, the largest unresolvable azimuth waves are of wavelength between 80–140 m (increasing with incidence angle). The orbital velocity of these waves modulating the fundamental scattering elements mainly determine the finite scene coherence time (see Chapter IV. C).

The degradation in azimuth resolution is one of the major reasons for the less pronounced wave patterns in the INSAR images obtained from flight paths 270° and 90°. The azimuthal orientation of the dominant swells makes them less resolvable with increasing range as the azimuthal resolution decreases (Figure 8.1 and Chapter

VIII. D. 2c). The wave patterns in the 90° and 270° SAR images were more affected by velocity bunching compared to the 360° SAR image. This might contribute to additional azimuthal degradation of the INSAR image.

In shallow water shoaling and refraction probably also play a role in determining the scene coherence time. Due to refraction, waves tend to propagate perpendicular to the bathymetric contours (refraction) which are mainly aligned alongshore, while shoaling results in increased wave amplitude and elliptic particle orbits. The change in the radar observed orbital velocity due to shoaling is believed to be small. The more pronounced effect is probably the refraction effect in which wave crests tend to align with the bathymetric contours in shallow water before breaking occurs. In deeper water, the wave length and direction are less affected by the bathymetry and the direction of wave propagation might be affected by local winds. In the Marina experiment the mild wind (< 2 m/sec) had no influence on the direction of propagation of the larger unresolved waves (80–140 m) which are of our interest since these waves determine the azimuth resolution. Therefore, the direction of the larger unresolved waves in deeper water was unknown. For flight path 360°, the refraction effect caused waves to be range oriented near the shore (smaller incidence angles) and hence the full magnitude of the orbital velocity should be observed by the radar, resulting in a faster decorrelation time of the surface. An indication of this effect can be noticed through the results depicted in Table 7.2 for the 360° image. Additional evidence using the present technique and *in situ* observations is needed to get a better understanding of the determination of scene coherence time in shallow water.

An important application of the knowledge of the scene coherence time is in defining the optimum physical baseline separation between the two antennas which determines the sensitivity of interferometric measurements of ocean surface velocity

fields. For a mean estimate of 0.1 sec. of the scene coherence time, it is required that the platform travel time through the effective baseline separation (9.9 m) will be less than 50 msec. Using the expression for the time delay for interferometric measurement $\Delta t = \tau_c/2$ and L-band NASA/DC-8 parameters yields a maximum baseline separation of:

$$B_{\max} = \Delta t \cdot 2V = 21.4 \text{ m} \tag{8.5}$$

This result shows that the actual baseline separation (19.8 m) used in the Marina experiment was almost optimal for the given environmental conditions. For rougher sea state and/or higher radar frequencies, the scene coherence time will be shorter and hence the baseline separation between the antennas should be reduced. The requirement for $\Delta t = \tau_c/2$ probably could be more flexible allowing $\Delta t \leq \tau_c$ and hence $B_{\max}$ could be increased resulting in an improved sensitivity in the INSAR phase measurement (given $\tau_c \geq 0.1$ sec.). The effects of increasing of the antenna baseline separation should be inferred in future experiments.

C. INTERFEROMETRIC SAR REMOTE SENSING OF OCEAN SURFACE CURRENTS

A primary objective of the present study is the verification of the feasibility of INSAR to estimate reliably ocean surface currents with high resolution over large regions. The Marina experiment demonstrates this feasibility by comparing INSAR estimates with almost simultaneous *in situ* Lagrangian drifter estimates (see Chapter VII. G). A scatter diagram of current magnitude estimates derived from the two sensors is illustrated in Figure 8.2. Simple statistical analysis shows a significant degree of linear correlation (R = 0.94), with a small consistent bias of 2.5 cm/sec. However, due to the relatively small number of compared estimates the statistical significance is rather low.

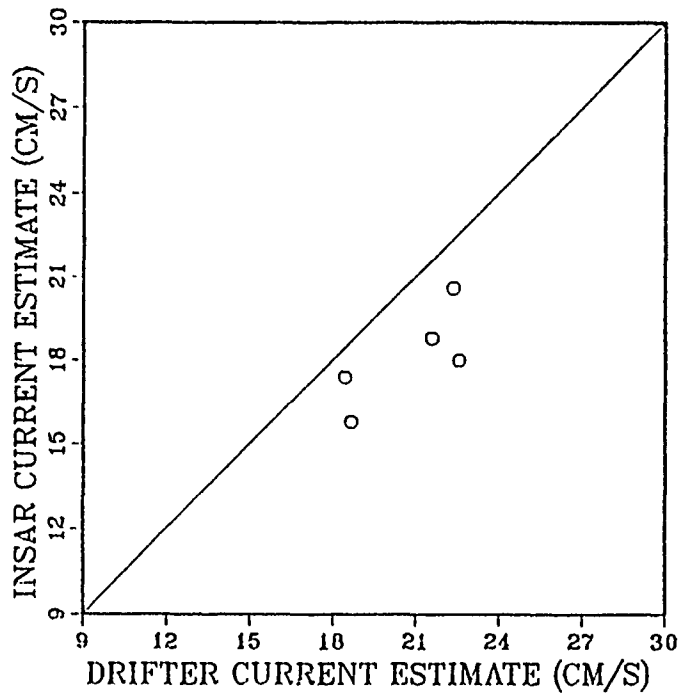

Figure 8.2: Lagrangian drifter versus INSAR surface currents estimates.

1. Limitations of Measurement Methods

In the eastward (90°) flight path image (from which the meridional current component was estimated) the radar was looking crosswinds. The estimation of the ambiguous phase velocity associated with the Bragg waves was derived from the western (270°) flight path image (see Chapter VII. C, G), which included the Salinas River. Unfortunately, the less noisy 90° phase image did not include a nearby calm region like the Salinas River to estimate the phase velocity bias. The 270° image was not selected for computation of meridional current estimates because it was the most noisy image obtained in the Marina experiment (see Chapter VII. D). Therefore, the substruction of the velocity bias introduced by the Bragg wave phase velocity for the meridional component was not straightforward, resulting in a less accurate estimation of this component.

Another difficulty that was addressed in estimating current components from INSAR phase images was the presence of slicks, which are clearly seen in the amplitude SAR images (see Figures 7.1, 7.2). These slicks are believed to be observed due to local dampening (straining) of the wind generated surface ripples which are responsible for the essential Bragg radar backscatter. Ocean surface straining can be introduced by various oceanographic phenomenas, one probable driving force to create slicks is that the surface signature is related to the convergence of surface particle velocities associated with internal waves. The internal waves might be generated by tidal flow variabilities over topographic features causing fluctuations in the thermocline. The local convergence zones introduce concentration of surface organics which dampen the surface ripples due to increased surface tension. Another mechanism creating regions of surface convergence are Langmuir cells in which the slicks are oriented in the direction of the wind. Because some of the slicks are aligned along the bathymetric contours and the wind was weak, it is believed that they are related to internal waves rather than Langmuir cells.

Mean temporal Lagrangian estimates are physically different in character from the synoptic instantaneous spatial observation of the surface currents, which could be described as a grid of Eulerian snapshots. The Lagrangian drifter trajectory would not necessarily follow the spatial current pattern measured instantaneously by INSAR, which is evident in Figure 8.2. Averaging of imaged subareas make the two different current estimates more comparable. This difference might be one of the reasons for the better agreement in the computed current magnitude estimates rather than current direction (see Table 7.4).

2. Current Measurement Conclusions

The results of the experiment in estimating surface currents with INSAR shown in Table 7.4, Figures 7.7, and 8.2, together with the discussion above, suggest

a number of conclusions which are basically consistent with those pointed out by Goldstein et al., 1989.

- The method seems to be most reliable when the radar observation is along the direction of the strongest current component (flight path 360°).
- The magnitude, rather than the direction of current estimates, is more consistent with conventional observation, probably because of the fundamental difference between the two measurement techniques.
- The interferometric technique seems to be more accurate when the radar is looking upwind (and probably also downwind). In these cases, the Bragg waves phase velocity responsible for the radar signal are less ambiguous, and the returned amplitude signal is strongest resulting in a better signal over noise.
- The estimates of the bias phase velocity (when looking upwind) are consistent with those expected theoretically.
- The interferogram contains numerous additional features in the ocean flow field which were neglected in the present study. Spatial nearshore current patterns is one phenomena which should be further analyzed.

D. OCEAN WAVE SPECTRA

The results of INSAR image spectral analysis tested against conventional wave array spectra estimates and refraction model predictions (Chapter VII. H) demonstrate that interferometric SAR under certain geometric orientations appears to offer considerably improved (relative to conventional SAR) imaging of waves also in complex nearshore regions.

1. Results Comparison

The predicted (Dobson's model) ray traces expressing the relationship between the water depth h and wavelength L and between the depth and direction of arrival α (Figures 8.3, 8.4) are such that the refraction model becomes insensitive to changes in h when

$$h > 0.4L_0, \tag{8.6}$$

where L_0 is the deep water wavelength. For the two observed swells in the Marina experiment this requirement results in a depth of 54 m for the shorter swell (9.1 sec) and 163 m for the longer swell. The western edges of the Northern flight path (360°) INSAR image which was mainly subjected to spectral analysis (Figure 7.8) represents a mean depth of 53 m. This indicates that both waves experience shoaling and refraction through the entire imaged scene.

The constructed wave refraction diagram (Figure 7.9) is consistent with the INSAR derived orthogonals. As mentioned previously, wave propagation angles can be sensitive to other oceanographic phenomena such as tides and coastal currents. Wavelengths are also subject to these effects but to a much lesser extent (Shuchman and Kasischke, 1981, Hayes, 1980). These effects were not considered in our refraction model. The observed weak currents (Chapter VII. G) and the consistent INSAR spectral results consistent with model predictions, indicate that these effects were minor during our experiment.

Figure 8.5 presents a plot of wave directions α_1, α_2 determined from INSAR 2D FFT versus α_1, α_2 calculated from Dobson's refraction model. The plot shows a significant degree of linear correlation (0.88) for the long crested swell which experience more significant refraction compared to the shorter observed swell

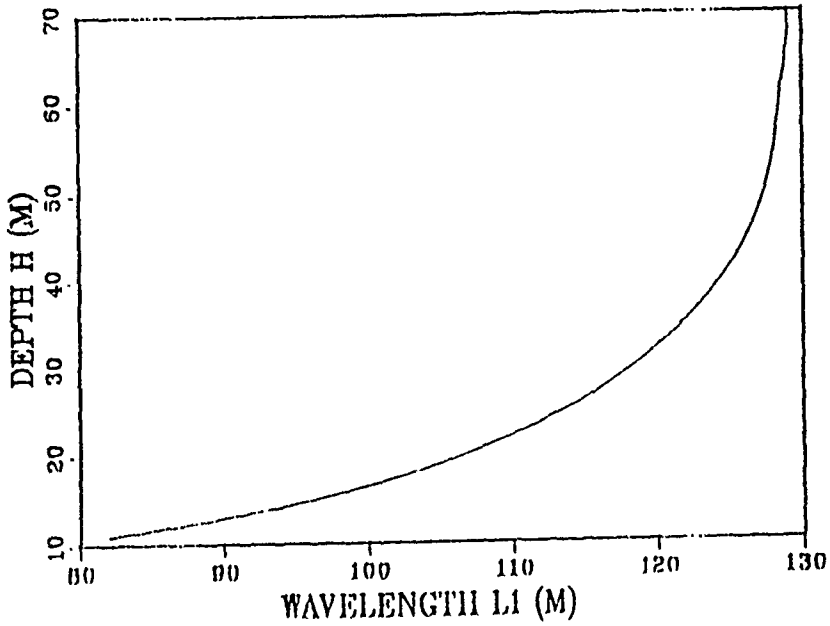

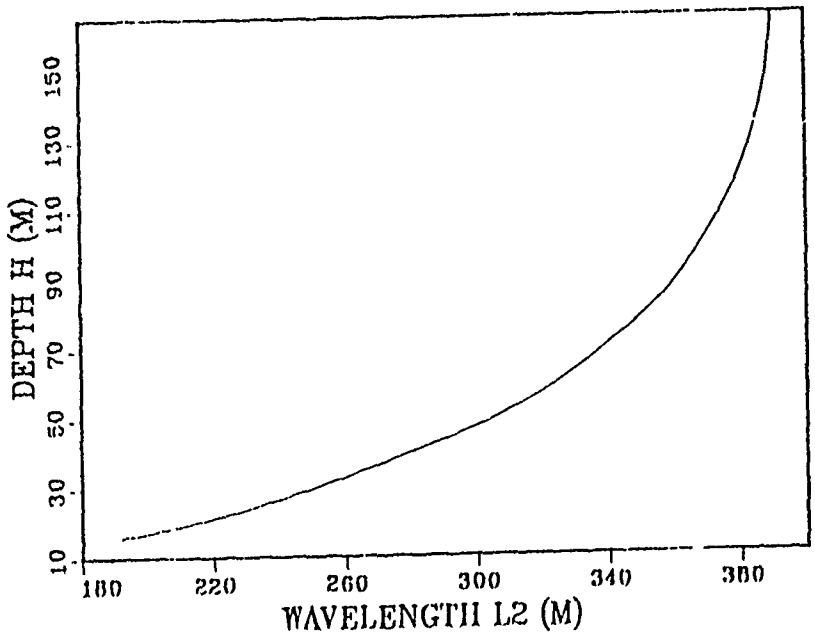

Figure 8.3: Relationship between water depth h and predicted wavelength in Monterey Bay based on Dobson's refraction model: *Top*: for the shorter observed swell $L_0 = 129$ m; *Bottom*: for the long crested swell $L_0 = 395$ m.

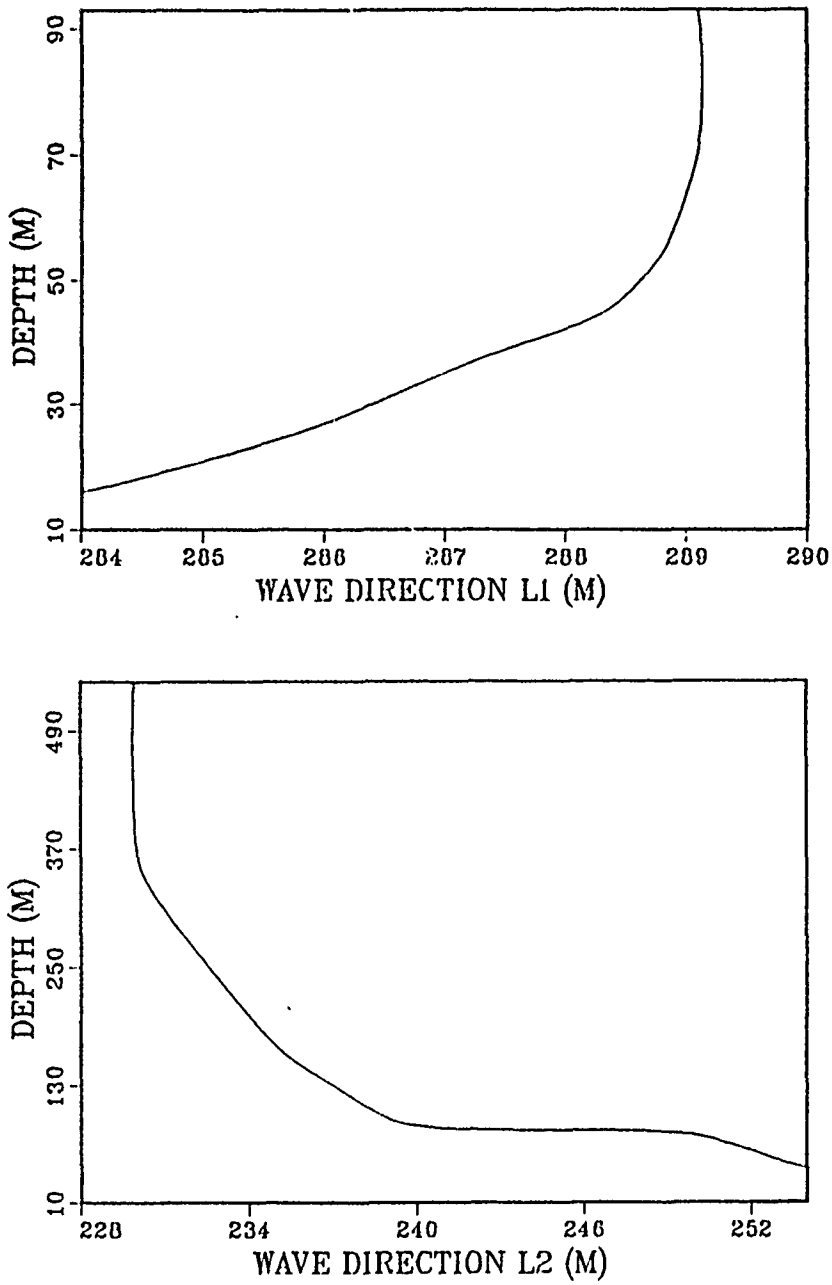

Figure 8.4: Relationship between water depth h and predicted direction of wave arrival α in Monterey Bay based on Dobson's refraction model: *Top*: for the shorter swell $L_0 = 129$ m; *Bottom*: for the longer swell $L_0 = 395$ m.

(correlations of 0.43). The reason for the better agreement of the narrow band long crested swell is probably because this swell is more monochromatic in character relative to the shorter swell and hence more comparable to the theoretical model, which is based on the analysis of monochromatic waves as input

The results for INSAR observed wavelengths compared with model predictions are depicted in Figure 8.6. The linear correlation is better than 0.9 for both swells. This is mainly because shoaling is less sensitive than refraction to oceanographic constrains and remote sensing imaging geometry. The measured *wavelength* from INSAR's image spectra compared with the *in situ* wave array wavelength estimates and model predictions, is in better agreement than *wave direction* (see Table 8.1).

It is felt that more advanced spectral analysis techniques like maximum entropy might improve the data analysis results in shallow water. This and other techniques offer the potential of reducing the number of wavelengths required in a sub-area which is subjected to spectral analysis (Schuchman and Kasischke, 1981). Together with more accurate bathymetric information the potential of improving the analysis of refraction and shoaling in shallow water can be obtained.

TABLE 8.1: Deviation of INSAR Image Spectra Wavelength and Direction from Wave Array and Model Prediction Output

	Wave Direction		Wavelength	
	T = 9.1 sec.	T = 15.9 sec.	T = 9.1 sec.	T = 15.9 sec.
Correlation	0.43	0.88	0.96	0.99
rms error	6.2°	6.4°	3.9 m	4.7 m

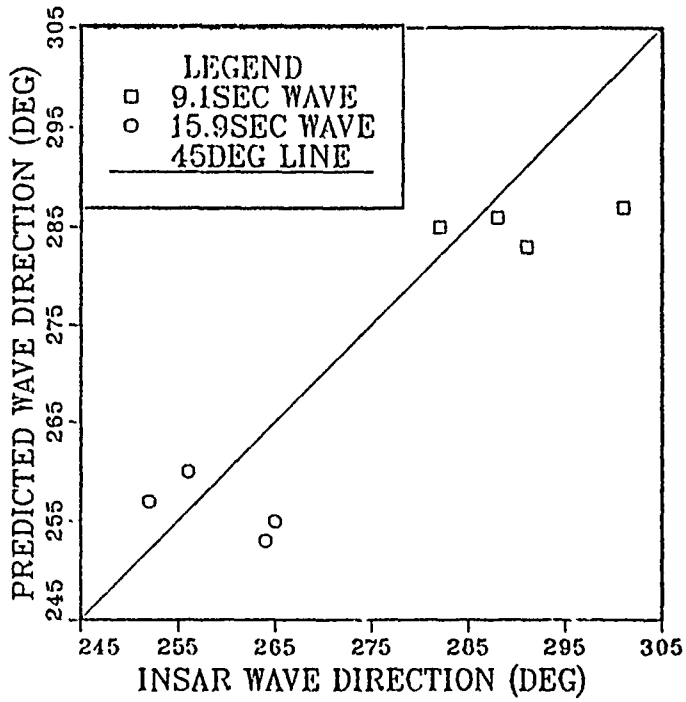

Figure 8.5: Predicted refraction versus INSAR 2D wavenumber spectra angles for the two observed swells (9.1 sec., 15.9 sec.).

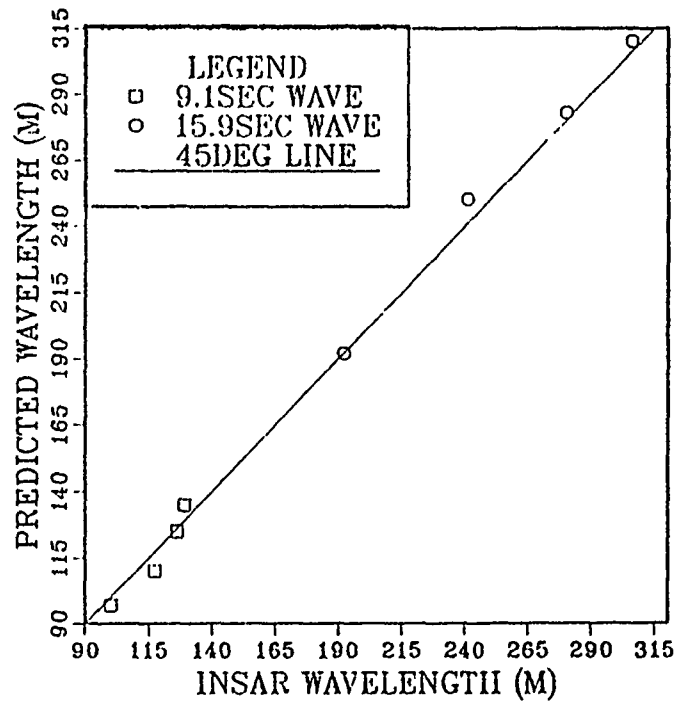

Figure 8.6: Predicted shoaling versus INSAR 2D wavenumber spectra angles for the wave array *in situ* observed swells (9.1 sec., 15.9 sec.).

2. Effects of Airborne SAR System on the Study of Ocean Surface Waves

Since the INSAR technique is based on SAR imagery, some key fundamental shortcomings of SAR in imaging ocean surface waves were described in Chapter III. D. Through examples from the acquired remote sensing data the effect of these shortcomings on INSAR wave imagery is discussed in this section. The known SAR coherent motion effects include velocity bunching, acceleration defocus and scene coherence time limitation. The noncoherent scene motion effects, which are only important for relatively slow scanning platforms like aircraft, include scanning distortion and smearing (look misregistration for multi-look processing).

a. *Scanning Distortion*

Scanning distortion arises due to the relative motion between the projected translation of the mean pattern of image reflectivity by the wave phase velocity C, and the imaging radar platform velocity V. Therefore, this relative velocity effects during the observation time is in general proportional to the ratio C/V.

The image patterns should be corrected if the projected azimuthal component of the phase velocity is significant compared to the platform velocity. In this case the image contrast can be improved by adjusting the processor focus by $C/2$. The spectral energies have to be corrected in the azimuthal direction by kC/V. Using this method suggested by Vachon et al. (1988), the inherent 180° ambiguity (for all imaging radars) in the wave peak directions can be resolved. Artifact spectral contours obtained from opposing flight directions will diverge after this correction, while the actual contours will converge. Using Equation (3.16) and the computed INSAR wavelength and direction from spectral analysis (see Table 7.5), the scanning distortion effect is estimated. Longer waves with higher phase velocity are relatively

more distorted. Therefore, the longest swell (310 m) computed from station 4 (360° image, Table 7.5) was selected to demonstrate the scanning distortion effect. The calculated wavelength distortion is of the order of 2% and 5° in direction. For shorter waves observed in 360° image where the waves were mainly range oriented, the scanning distortion for both swells is practically negligible. Figure 8.7 illustrates INSAR image spectra computed from sub-areas in the wave array and in deeper water centered 2000 m west from the wave array zone for the eastern 90° flight path. Shoaling and refraction effects are observed for the shorter swell only (peak P1) since the long crested swell is less, much less energetic in deeper water and was not observed. In shallow water the long crested swell becomes more energetic due to shoaling and a relatively weak peak with a wavelength of 212 m and direction of 74°, 14° norther from the computed (direction 260°) wave array directional spectra, was measured. Due to the azimuthal orientation of the swells in the 90° flight path the wavelengths are distorted by almost 6–7%, which is relatively a large effect compared with the corresponding 360° flight path image in which these swells had a range orientation. Correction for scanning distortion will make these swells more comparable to the wave array wavelength estimated (192 m, Table 7.5).

In deeper water a relatively large rotation of the shorter swell towards range direction is observed. This additional rotation (also of the long swell in shallow water) is not well understood at the moment. The noncoherent scene motion effects are negligible for spacecraft since the ratio C/V is small.

b. *Velocity Bunching*

For azimuthaly oriented waves, the velocity bunching imaging mechanism is significant. Though the INSAR image formation is not based on this mechanism it is formed from complex SAR images, which might be distorted due to

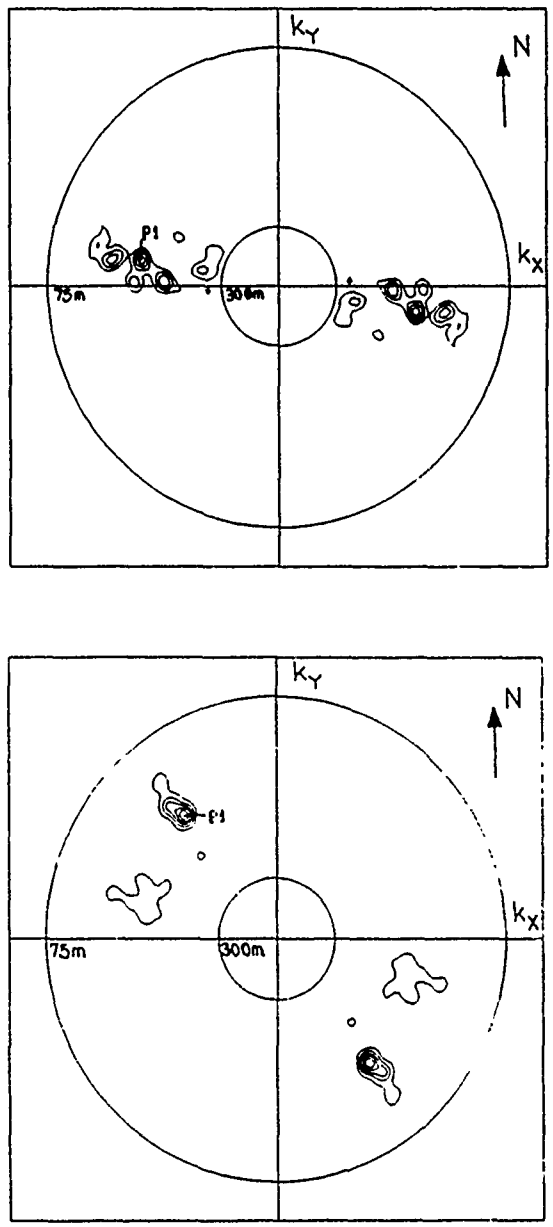

Figure 8.7: INSAR Eastern 90° flight path image spectra computed from: *Top*: Shallow water sub-area close to the Marina wave array; *Bottom*: Deeper sub-area centered 2000 m west from the shallow sub-area.

bunching effects. For INSAR imagery it is felt that velocity bunching might contaminate the image formation. This imaging mechanism becomes less significant as the wave direction become more range oriented, the wavelength increases and/or the wave height decreases. Based on the theory described in Chapter III. D and INSAR orbital velocity estimates, the velocity bunching effect is evaluated.

The fractional amplitude of the azimuthal image shift is estimated using Equation 3.13. The wave amplitude is computed from the INSAR image data, using linear wave theory and simple geometry considerations. The mean estimated orbital velocity obtained from 360° INSAR image for the 9.1 sec. swell varies between 20–23 cm/sec. This velocity is consistent with the rough estimate of U_{OB} using Equation (7.13). The shorter swell was selected for a test case since it has a relatively larger orbital velocity and hence experience a stronger bunching effect. The imaged area is considered as intermediate water depth, therefore the orbital wave particle velocity pattern is elliptic rather than circular. The equation of this pattern is given by:

$$\frac{U^2}{A'^2} + \frac{W^2}{A'^2 tgh^2 kh} = 1 \tag{8.7}$$

where $A' = AgT'/L$, and U, and W are the horizontal and vertical velocity components. Transforming Equation (8.7) into polar coordinates after simple manipulation the wave amplitude is obtained

$$A = \frac{Lr}{gT'} \left(\frac{\sin^2 \gamma}{tgh^2 kh} + \cos^2 \gamma \right)^{1/2} \tag{8.8}$$

with

$$r = \frac{U_{OB}}{(\sin^2 \gamma \sin^2 \phi + \cos^2 \phi)^{1/2}} \tag{8.9}$$

where γ is the incidence angle and ϕ is the angle between the wave direction and the radar platform attitude. For both swells estimated from INSAR image spectra

close to the Marina wave array, C'_{cr}, and C' are computed using Equations (8.8), (8.9), (3.13), and (3.14). Table 8.1 shows that both swells are far from being critical. The shorter swell is more influenced by velocity bunching. The highest ratio of $C'/C'_{cr} = 0.3$ is obtained for the eastward 90° flight path due to an increased azimuthal orientation of the imaged swell. This might be one of the reasons for the more smeared INSAR image obtained from the eastward flight path relative to the northward 360° flight path image. The results depicted in Table 8.1 mainly show that the imaged scattering elements redistribution is one to one resulting in single unambiguous brightness patterns in the SAR imagery representing the actual ocean waves.

TABLE 8.2: Actual Velocity Bunching Parameters (C, C_{cr}) Estimates Obtained from INSAR Imagery (Northern Flight Path 360°)

Wave Period T' (sec)	Flight Path	γ	ϕ	h (m)	L (m)	U_{OB} (cm/sec)	A (m)	C'_{cr}	C'
9.1	360°	40°	69°	16	97	23	0.3	43	10
15.9	360°	40°	84°	16	192	15	0.2	292	0.4
9.1	90°	45°	12°	16	120	16	0.23	19	6

c. *Coherent Motion Effect*

The degradation in azimuthal resolution due to finite scene coherence time has a low pass filter effect on the SAR image. It shifts the azimuthal wave number to lower values. An example of this effect is inferred by comparing the wave array spectra (Figure 7.11, *Bottom*) and the corresponding INSAR image derived

spectra (Figure 8.7, *Top*). The *in situ* wave array spectrum clearly shows another peak with a wavelength of almost 70 m and direction of 300°. For flight path 90° this relatively short swell is basically azimuthally oriented and is not seen in the INSAR image spectra. It is concluded that the wave patterns in the INSAR images obtained from flight paths 90° and 270° are less pronounced mostly due to the azimuthal smear caused by the finite scene coherence time limitation. An evidence of this conclusion can also be observed in Figure 7.4. At low incidence angles where the degradation in azimuth resolution is relatively small waves are clearly observed in the INSAR image. At higher incidence angles where the degradation is larger, wave patterns are hardly seen. This evidence illustrates the importance of the finite scene coherence time in determining the SAR and INSAR capability to image ocean surface waves.

3. INSAR Derived Spectra Conclusions

- The experimental results show how interferometric SAR may be used to image ocean surface waves. Given the problems associated with imaging waves using conventional SAR, this unique technique represents a significant advance. The agreement between INSAR image spectra and *in situ* derived spectra (Figures 7.11, 7.14) is encouraging. In spite of this potential, this section illustrated some of the problems that might arise with an airborne INSAR in imaging ocean surface waves.

- Noncoherent scene motion effects are dependent upon C/V. For a relatively slow airborne SAR (and INSAR) platform , noncoherent motion effects might lead to wave imaging complications that include scanning smear and distortion, which might result in ambiguous image wave patterns. This effect is neglibile for a fast moving platforms like spacecraft. Focusing adjustment and

scanning distortion correction methods are not reliable for multimodal wave fields, which is usually the actual situation of the ocean surface (Vachon et al., 1988).

- The finite scene coherence time degrades the azimuth resolution which is proportional to R/V and was shown to have an important role for ocean wave imaging for aircraft and spacecraft. Another coherent motion effect is the velocity bunching. The observed wave field (flight path 360°) contained mainly range-oriented waves. This orientation is favorable for radar imagery since it minimizes image distortion due to azimuth image shift (velocity bunching). The imaged waves in the Marina experiment did not experience significant coherent azimuth image shift (Table 8.2).

- Several effects degrade the INSAR image wave patterns (see Figure 7.4). The dominant effects are believed to be: the degradation in azimuth resolution due to finite scene coherence time, looking crosswinds rather than upwind and speckle and random noise. The lesser effects for the Marina experiment conditions were scanning distortion and probably velocity bunching.

- In shoaling waters the area of the image being subjected to spectral analysis should be reduced to allow the waves to be represented locally without refraction and shoaling effects.

E. SOURCE OF SWELLS

The Global Spectral Ocean Wave Model (GSOWM) outputs for August 31 and September 8, 1989 clearly illustrate the possible sources and directions of dominant wave propagation (see Figures 6.8–6.11). A GSOWM 2D spectrum taken at a grid point about 60 miles southwest off Monterey Bay (Figure 8.8) indicates a

9.5 second northwesterly wave system together with a narrow-band southerly swell (16 sec.). The propagation of the long crested southerly swell into Monterey Bay is consistent with the increasing importance of refractive features with decreasing wave frequencies in the southern edge of Monterey Bay.

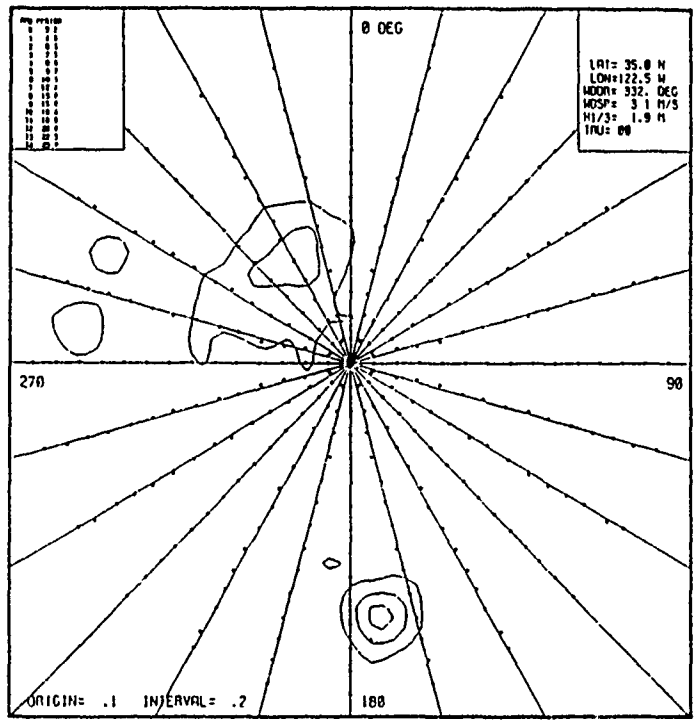

Figure 8.8: GSOWM directional frequency spectrum obtained from a grid point at 35° N Lat and 122.5° W Long on September 8, 1989. A southerly 16 sec. swell and a 9.5 sec. northwest wave system are observed.

The characteristics of southerly swells in the northern hemisphere are not well understood. Munk et al., in a series of papers, established the source as high latitude storms in the South Pacific and Indian Oceans. These swells are usually less energetic (smaller amplitude after traveling 10,000 km) and longer in period than swells originating in the North Pacific (Guza, 1986 and Semdin, 1986). Based on the

global models of pressure fields, winds and spectral analysis, it is assumed that the south-southwest long crested swell observed in the Marina experiment, September 8, 1989, was generated by a high latitude southern hemisphere storm and that the west-northwest shorter period swell was generated by a northwest Pacific storm.

IX. CONCLUSIONS

The present study reveals the considerable ability of this novel technique to provide reliable quantative spatial information about dynamic processes at the ocean surface. Realization of the potential of Interferometric SAR with spacecraft might make it possible to monitor global ocean wave spectra and surface currents.

The mean estimate of the L-band scene coherence time O (100 msec) obtained from INSAR and SAR imagery during the Marina experiment, on September 8, 1989, is consistent with the sparse known observational estimates obtained under similar moderate sea state and ambient conditions. This parameter is shown to be the dominant limiting factor in determining the SAR and INSAR azimuth resolution and hence the azimuthal cutoff wavenumber for imaging ocean surface dominant waves. Waves with azimuthal component shorter than O (100 m) could not be observed. The azimuth image shift (velocity bunching) caused by the coherently sensed radial component of the orbital velocity of the long waves might disturb the INSAR phase measurement. It is shown that the noncoherent scanning distortion effect is important if the projected phase velocity of the imaged wave is significant relative to the platform velocity. This effect is negligible for fast scanning platforms like spacecraft. It is concluded that range oriented waves are favorable for INSAR (and SAR) where the undesired motion effects like the temporal decorrelation of the ocean surface and velocity bunching do not distort the image. Also, range waves project a larger radial component of orbital velocity (which is sensed by INSAR), compared with azimuthal waves. Additional theoretical and experimental studies are required to quantify and to provide better understanding of these issues in terms of INSAR performance to image ocean surface wave fields.

The results of this experiment in estimating ocean surface currents, together with earlier work by Goldstein et al. (1989), and for the first time ocean wavenumber spectra suggest some additional conclusions:

- The method is shown to be most reliable when the radar observation is along the direction of the strongest current component.
- The interferometric technique appears to be more accurate when the radar is looking upwind (and probably downwind). In these cases, the phase velocity bias from the Bragg waves responsible for the radar signal is less ambiguous, and the returned amplitude signal is strongest.
- Shoaling and refraction effects are clearly observed in the INSAR phase images. In shoaling waters, the area of the image being interpreted via spectral analysis should be reduced to insure homogeneous waves.
- The interferograms contain numerous additional ocean surface features which were not pursued in the present study, such as convergence, divergence, and vorticity fields and internal and other long waves.

APPENDIX A

INTERFEROGRAM PROCESSING

The recorded SAR data from each antenna consists of a set of four files. Each file consists of 1024 azimuth by 750 range pixels. P_{mij} and Q_{mij} are the corresponding complex compressed pixel values in the imaging map as processed from the recordred data received from each of the two antennas. The subscripts m, i, j are the file number, row, and column of a pixel, respectively. I_{ij} is the complex image value of a pixel in the interferogram. A_{ij}, Φ_{ij} is the magnitude and phase of I_{ij}.

Processed Imaging Files from each Antenna

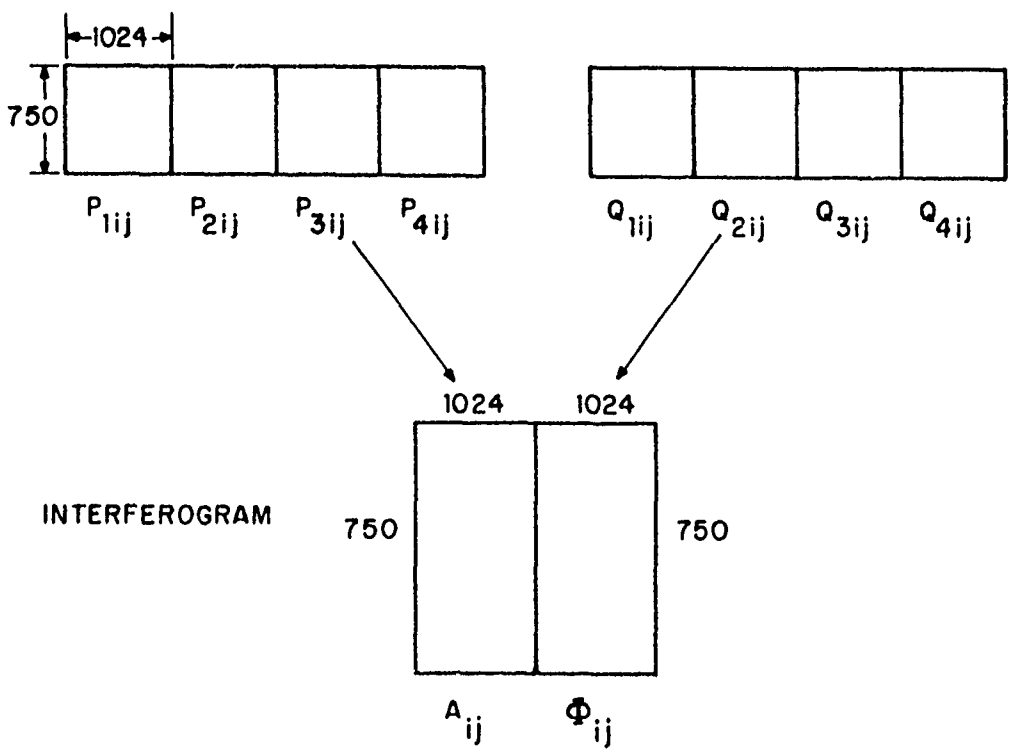

I_{ij} is derived by taking the complex conjugate product of the sum of the four corresponding original complex image pixels obtained from each antenna.

$$I_{ij} = \sum_{m=1}^{4} P_{mij} Q^*_{mij} \tag{A.1}$$

or

$$I_{ij} = A_{ij} \ \exp[i\Phi_{ij}] \tag{A.2}$$

The interferogram file as received from JPL is processed to a 2048 azimuth by 750 range pixels. The first 1024 azimuth pixels are magnitudes of the complex reflectivity (A_{ij}) and the other 1024 pixels are phases which consists of information of surface velocity.

The pixel averaging in Equation A.1 is in expanse of azimuth resolution. The pixel size is the resulting interferogram is 12.1 m is azimuth and 6.6 m in the viewing direction.

APPENDIX B

ESTIMATION OF RANDOM ERROR IN LAGRANGIAN DRIFTER VELOCITY

A. THEORETICAL BACKGROUND

Drifter velocity is a simple function of distance traveled divided by time, where distance is found by differencing positions. Thus, random errors in the positions do propogate into the velocity.

The velocity, $\mathbf{V}$, is a function of the starting and ending position, $\mathbf{X}_1$ and $\mathbf{X}_2$, and the time difference $\Delta T = T_2 - T_1$

$$\mathbf{V} = F(\mathbf{X}_1, \mathbf{X}_2, \Delta T) \tag{B.1}$$

where $\mathbf{V}$, $\mathbf{X}_1$ and $\mathbf{X}_2$ are all vector quantities with east and north components given by:

$$\mathbf{V} = (u, v) \qquad \mathbf{X}_1 = (x_1, y_1) \qquad \mathbf{X}_2 = (x_2, y_2) \tag{B.2}$$

Specifically,

$$u = (x_2 - x_1)/\Delta T \qquad v = (y_2 - y_1)/\Delta T \tag{B.3}$$

The error propagation equation can be set up with $\Sigma(\mathbf{V})$ being the 2×2 variance-covariance matrix of the velocity components

$$\Sigma(\mathbf{V}) = G\ \Sigma(\mathbf{X}_1, \mathbf{X}_2)\ G^T = \begin{bmatrix} \sigma_u^2 & \sigma_{uv} \\ \sigma_{vu} & \sigma_v^2 \end{bmatrix} \tag{B.4}$$

where G is the 2×4 Jacobian of partial derivatives and is defined as

$$G_{i,j} = \frac{\partial F_i(u,v)}{\partial S_j(\mathbf{X}_1, \mathbf{X}_2)} \qquad \begin{array}{l} i = 1,2 \\ j = 1,2,3,4 \end{array} \tag{B.5}$$

or simply in our case

$$G = \begin{bmatrix} 1 & 0 & -1 & 0 \\ 0 & 1 & 0 & -1 \end{bmatrix} \frac{1}{\Delta T} \tag{B.6}$$

and Σ_x is the 4×4 combination of variance-covariance matrix for the variable positions and is taken to be

$$\Sigma(\mathbf{X}_1, \mathbf{X}_2) = \begin{bmatrix} \sigma_{x_2}^2 & \sigma_{x_2 y_2} & 0 & 0 \\ \sigma_{x_2} & \sigma_{y_2}^2 & 0 & 0 \\ 0 & 0 & \sigma_{x_1}^2 & \sigma_{x_1 y_1} \\ 0 & 0 & \sigma_{x_1 y_1} & \sigma_{y_2}^2 \end{bmatrix} \tag{B.7}$$

B. OBSERVATION ERROR ESTIMATES

Using Equations (B.1) through (B.7), the velocity error estimates are computed:

1. Group I: Between observation 2 and 1

$$\begin{aligned}
T_1 &= 11,49,30 \text{ (hours, minutes, seconds) PDT} \\
T_2 &= 13,15,44 \text{ PDT} \\
\Delta T &= 86.2 \text{ min} \\
\Sigma(\mathbf{X}_1) &= \begin{bmatrix} 20.07 & 2.69 \\ 2.69 & 8.24 \end{bmatrix} \text{m}^2 \\
\Sigma(\mathbf{X}_2) &= \begin{bmatrix} 22.76 & 2.69 \\ 2.69 & 8.03 \end{bmatrix} \text{m}^2 \\
\Sigma(\mathbf{V}) &= \begin{bmatrix} 1.6 \cdot 10^{-2} & 2 \cdot 10^{-3} \\ 2 \cdot 10^{-3} & 6 \cdot 10^{-3} \end{bmatrix} \text{cm}^2\text{sec}^{-2} \\
\sigma_u &= 0.13 \text{ cm/sec} \\
\sigma_v &= 8 \cdot 10^{-2} \text{ cm/sec}
\end{aligned}$$

2. Group I: Between observations 3 and 2

$$T_3 = 14,16,12 \text{ PDT}$$

$$T_2 = 13,15,44 \text{ PDT}$$

$$\Delta T = 60.5 \text{ min}$$

$$\Sigma(\mathbf{X}_1) = \begin{bmatrix} 25.59 & 2.7 \\ 2.7 & 7.88 \end{bmatrix} \text{m}^2$$

$$\Sigma(\mathbf{X}_2) = \begin{bmatrix} 22.76 & 2.69 \\ 2.69 & 8.03 \end{bmatrix} \text{m}^2$$

$$\Sigma(\mathbf{V}) = \begin{bmatrix} 3.7 \cdot 10^{-3} & 4 \cdot 10^{-3} \\ 4 \cdot 10^{-3} & 1.2 \cdot 10^{-3} \end{bmatrix} \text{cm}^2\text{sec}^{-2}$$

$$\sigma_u = 0.19 \text{ cm/sec}$$

$$\sigma_v = 0.11 \text{ cm/sec}$$

3. Group II: Between observations 2 and 1

$$T_1 = 12,05,28 \text{ PDT}$$

$$T_2 = 13,36,08 \text{ PDT}$$

$$\Delta T = 90.7 \text{ min}$$

$$\Sigma(\mathbf{X}_1) = \begin{bmatrix} 27.2 & 2.13 \\ 2.13 & 7.67 \end{bmatrix} \text{m}^2$$

$$\Sigma(\mathbf{X}_2) = \begin{bmatrix} 32.26 & 1.49 \\ 1.49 & 7.44 \end{bmatrix} \text{m}^2$$

$$\Sigma(\mathbf{V}) = \begin{bmatrix} 2 \cdot 10^{-2} & 10^{-3} \\ 10^{-3} & 5 \cdot 10^{-3} \end{bmatrix} \text{cm}^2\text{sec}^{-2}$$

$$\sigma_u = 0.14 \text{ cm/sec}$$

$$\sigma_v = 7.10^{-2} \text{ cm/sec}$$

4. Group II: Between observations 3 and 2

$$T_3 = 14,42,39 \text{ PDT}$$

$$T_2 = 13,36,08 \text{ PDT}$$

$$\Delta T = 6.65 \text{ min}$$

$$\Sigma(\mathbf{X}_1) = \begin{bmatrix} 33.78 & 0.24 \\ 0.24 & 7.33 \end{bmatrix} \text{m}^2$$

$$\Sigma(\mathbf{X}_2) = \begin{bmatrix} 32.26 & 1.49 \\ 1.49 & 7.44 \end{bmatrix} \text{m}^2$$

$$\Sigma(\mathbf{V}) = \begin{bmatrix} 4.1 \cdot 10^{-2} & 10^{-3} \\ 10^{-3} & 9 \cdot 10^{-3} \end{bmatrix} \text{cm}^2\text{sec}^{-2}$$

$$\sigma_u = 0.2 \text{ cm/sec}$$

$$\sigma_v = 0.1 \text{ cm/sec}$$

APPENDIX C

IMAGE COORDINATES GROUND TRUTHING USING GPS DATA

A. IMAGE ADJUSTMENT PREPARATION

A modified Transverse Mercator projection was used to convert the latitude and longitude ground coordinates to a plane coordinate grid of eastings and northings, (E, N) coordinate system (Floyd, 1985). The projection was centered in the image area in order to minimize grid distortions. GRS 80 ellipsoid values were used which are essentially the same as for the WGS 84 geometric ellipsoid. The projection parameters are:

Ellipsoid Semi-Major Axis, an Inverse Flattening, 1/f	6378137.0 meters 298.257222101
Central meridian (longitude) False latitude False easting Scale factor, central meridian	W 121° 47.0' N 36° 40.0' 3000 meters 1.00000

The range pixel number (y) of the image control points needed a small correction for elevation distortion (Ulaby, 1982). The corrected range pixels, y_c, were computed as follows:

$$y_c = 1/k_y \left(\sqrt{k_y(y-1) + r_o)^2 + 2Hz - z^2} - r_o \right) + 1 \qquad \text{(C.1)}$$

where

TABLE C.1: Ground and Image Coordinate Data

Point ID	Type	Latitude (d m s)[1] Longitude (d m s) Elevation (m)	Plane Coordinates (m) Easting Northing	Image Coordinates (pixels) x y A90	A270	A360
1	Bridge abuttment	N 36 43 58.34 W 121 46 51.77 6.1	3204.3 7347.1		313 139	197 69
3	Road intersection	N 36 43 15.46 W 121 47 14.89 15.2	2630.4 6025.0	146 484	295 222	245 104
4	Fence corner	N 36 42 47.87 W 121 46 12.88 30.5	4169.5 5174.9	82 434	360 280	
5	Fence corner	N 36 42 37.74 W 121 46 33.99 33.5	3645.5 4862.4	104 415	339 305	296 24
7	Fence corner	N 36 42 12.89 W 121 46 16.03 42.7	4091.3 4096.4	86 364		
10	Road intersection	N 36 41 15.95 W 121 47 57.65 3.0	1568.8 2341.3	190 261	250 493	397 182
	IMAGE PARAMETERS (*a priori* values)	Azimuth Scale, k_x (meters/pixel)		24.20	24.20	24.20
		Range Scale, k_y (meters/pixel)		16.14	14.54	12.34
		Flight azimuth, α (degrees)		90°	270°	000°
	IMAGE CONSTANTS	Flying height, H (meters)		8285	8273	8178
		Ground range to 1st pixel, r_o from nadir (meters)		2601	2918	4015

[1] d m s = deg min sec

y = range pixel number (uncorrected)

k_y = *a priori* range scale (meters/pixel)

r_o = ground range from nadir to $y = 1$ pixel (meters)

h = flight altitude (meters)

z = elevation of ground point (meters)

The magnitude of these corrections was small, generally less than 2 pixels. However, for a few points at elevations of 30 meters or more near the flight line, the corrections ranged from 3 to 5 pixels. The correction always increased the pixel number, moving the point further from the flight line. Only the control points needed this correction, the imaged water surface assumed to be at zero elevation were not subjected to elevation distortion.

B. IMAGE ADJUSTMENT COMPUTATION

The adjustment can be viewed as solving for the best mathematical mapping between the image and ground coordinate systems, between (x, y) and (E, N), subject to assumptions about the underlying form of the mathematical transformation.

The adjustment used a least-squares technique in which the observed data are weighted inversely proportional to their variances, as described in most surveying or photogrammetry texts. This weighting strategy results in a minimum variance solution, which is generally considered the best solution when using data of unequal precision. The specific form applied here is called the "combined observation and condition equation" method (Uotila, 1986).

The assumed transformation was a simple scaling, rotation, and translation between the (x, y) and (E, N) coordinates systems, with the addition of separate

scales in the x and y directions (i.e., the pixels were assumed to be rectangular, not square). The assumed form of the transformation equations was:

$$E_i - E_o + x_i k_x \sin\alpha + y_i k_y \cos\alpha = 0 \tag{C.2}$$

$$N_i - N_o + x_i k_x \cos\alpha - y_i k_y \sin\alpha = 0 \tag{C.3}$$

where

$$\begin{aligned}
E_i, N_i &= \text{ground coordinates of } i\text{th control point,} \\
x_i, y_i &= \text{image coordinates of } i\text{th control point,} \\
k_x, k_y &= \text{scales (meters/pixel) in } x \text{ and } y \text{ directions,} \\
\alpha &= \text{azimuth of the flight line and rotation between} \\
&\quad\ \text{coordinate systems}(\alpha = 0 \text{ points to north}), \\
E_o, N_o &= \text{ground coordinates of image origin, } (x, y) = (0, 0).
\end{aligned}$$

Note that the x-axis points are opposite to the flight line direction because of the way the image processing hardware loaded the image data. This accounted for the unusual appearance of the signs in these equations (C.2, C.3). Also note that α is measured clockwise from north, which causes the role of the sine and cosine factors to be reversed in comparison with some other presentations.

In the adjustment terminology, the quantities k_x, k_y, α, E_o, and N_o are parameters to be solved for. Hence there were 5 parameters in each image. For each control point, one pair of condition equations (C.2 and C.3) were formed. As long as the number of condition equations exceeded the number of parameters, the least squares solution was possible.

Three addition condition equations were used, reflecting the *a priori* estimates of the parameters k_x, k_y, and α:

$$k_x - k_{xo} = 0 \tag{C.4}$$

$$k_y - k_{yo} = 0 \tag{C.5}$$

$$\alpha - \alpha_o = 0 \tag{C.6}$$

where k_{xo}, k_{yo}, and α_o were the *a priori* values of the respective parameters.

Five control points were used on images A90 and A270, and four control points on image A360. Hence, 13 condition equations were used for A090 and R270, and 11 for A360; more than enough for the least squares adjustment. Weighting required estimation of the standard errors (precision) on each observation. The estimated values were as follows:

$$\begin{aligned}
\sigma_E = \sigma_N &= 30 \text{ meters} \\
\sigma_x = \sigma_y &= 3 \text{ pixels} \\
\sigma_{\alpha o} &= 1 \text{ degree} \\
\sigma_{k_{xo}} &= 0.1 \text{ meters/pixel} \\
\sigma_{k_{yo}} &= 0.2 \text{ meters/pixel}
\end{aligned}$$

The adjust proceeded as follows. Define the set of condition equations as $F(L_a, X_a) = 0$, where the vector L_a represents the adjusted values of the observables (E_i, N_i, x_i, y_i, k_{xo}, k_{yo}, α_o) and the vector X_a represents the adjusted values of the parameters (k_x, k_y, α, E_o, N_o). The set of condition equations $F(L_a, X_a)$ has the form of Equations (C.2) through (C.6).

With,

$$\begin{aligned}
N &= \text{number of control points on the image} \\
R &= \text{number of condition equations} \\
U &= \text{number of parameters} = 5
\end{aligned}$$

then,

$$R = 2N + 3 \tag{C.7}$$

which is the number of condition equations in the set $F(L_a, X_a)$. The length of L is $4N + 3$. The degrees of freedom in the adjustment is $R - U$,

$$dof = 2N + 3 - 5 = 2N - 2 = 2(N - 1) \tag{C.8}$$

Because the set $F(L_o, X_o) \neq 0$ when L_o is the raw observations and X_o is the approximate values of the parameters, define a non-zero vector W, length R,

$$W = F(L_o, X_o).$$

The adjusted parameters are found by iterating the following matrix equation until the X_a vector converges,

$$X_a = X_o + dX \tag{C.9}$$

$$dX = -(A^t M^{-1} A)^{-1} A^t M^{-1} W \tag{C.10}$$

where matrix $A = dF/dX$ (R rows by U columns), matrix $M = BCB^t$ (R by R), matrix $B = dF/dL$ (R by L), and matrix C = covariance matrix of observables (L by L).

In this case, C was a simple diagonal matrix of estimated variances of each observed quantity, and provides the relative weighting of the observations in the adjustment. The traditional weight matrix is called P, where $P = C^{-1}$.

For analysis of the quality of the adjustment, *residuals* on the observed quantities were computed, as a vector

$$V = L_a - L_o = -C\,B^t M^{-1}(AdX_a + W) \tag{C.11}$$

and the "*variance of unit weight*" was computed as the scaler

$$\sigma_o^2 = (V^t P\, V)/dof. \tag{C.12}$$

The adjustment also computed precisions for the derived values of the parameters, expressed as a *covariance matrix of the parameters*, C_x,

$$C_x = (A^t M^{-1} A)^{-1} \tag{C.13}$$

Each of these adjustment results, Equations (C.9) through (C.13), were computed for each image. The results are summarized in Table C.2.

C. POST-ADJUSTMENT IMAGE SHIFT

Normally, an adjustment process like that described would be sufficient to accurately align an image with ground coordinates. In this case, however, the adjusted results might have been degraded by the lack of available control points. In typical image adjustment problems the control points are selected to span the entire image area. Because most of each image was over water, the control points were concentrated in a relatively small land portion. Hence, the danger the results might not be reliable in the water area. Essentially, the danger was one of using extrapolation rather than interpolation.

Examination showed that the adjusted scale and azimuth values agreed reasonably well with their *a priori* values — but not exactly (most within 1 standard deviation). But because these three parameters determined the overall size and orientation of the image, it was decided to accept the *a priori* values rather than the adjusted values. The *a priori* values were derived from flight navigation data and known characteristics of the SAR instrument. Consequently, it was felt they better represented the true values for the entire image area.

This left the adjustment to determine the location of the images. The image origin coordinates (E_o, N_o) solved for in the adjustment reflected the adjusted

TABLE C.2: Image Adjustment Results

Image	Parameter	k_x (m/pix)	k_y (m/pix)	α (deg)	E_o (m)	N_o (m)
A90	Initial	24.20	16.14	90.0	–	–
	Adjusted	24.20	16.20	89.9	6173	−1864
	σ	(0.04)	(0.07)	(0.3)	(35)	(33)
	Post adjustment origin shift				−8	5
	Final origin coordinates				6165	−1859
	Variance of unit weight		0.14			
	Latitude limits N 36-39-00 to N 36-43-28					
	Longitude Limits W 121-44-54 to W 121-53-12					
A360	Initial	24.20	12.34	000.0	–	–
	Adjusted	24.23	12.51	001.3	4129	11988
	σ	(0.12)	(0.22)	(0.8)	(91)	(60)
	Post adjustment origin shift				−384	68
	Final origin coordinates				3745	12056
	Variance of unit weight		1.76			
	Latitude limits N 36-39-49 to N 36-46-30					
	Longitude limits W 121-46-30 to W 121-50-44					

TABLE C.2: Continued

Image	Parameter	k_x (m/pix)	k_y (m/pix)	α (deg)	E_o (m)	N_o (m)
A270	Initial	24.20	14.54	270.0	–	–
	Adjusted	24.19	14.34	271.0	−4416	9437
	σ	(0.09)	(0.14)	(0.7)	(68)	(105)
	Post Adjustment origin shift				−69	−58
	Final Origin coordinates				−4485	9379
	Variance of unit weight		1.39			
	Latitude limits N 36-41-03 to N 36-41-03					
	Longitude limits W 121-43-42 to W 121-52-01					

rather than *a priori* image size and orientation. The further the origin point from the actual control points used, the less precise its ground coordinates were determined. To compensate for this effect, ground coordinates of the four image corners were computed in two ways, using (1) the adjusted and then (2) the *a priori* parameter values. The origin coordinates were then shifted to align the centers of the two versions. In other words, any systematic errors were forced to the edges of the image and minimized near the center.

The amount of this post-adjustment origin shift was barely significant on images A90 and A270, in comparison with the standard error of the adjusted coordinate values (see Table C.2).

On image A360, however, this shift was large, about 180 meters westward, which was twice the estimated standard error. No obvious explanation for this discrepancy was found, and subsequent comparisons of the predicted wave gage position with the distance from the shoreline in the image indicated that an additional

200 meter westward shift was needed; for a total shift of about 380 meters west of the adjustment derived position. Whatever the error, it did not appear to affect the north-south direction.

LIST OF REFERENCES

1. Abreu, M. P., "Kinematics Under Wind Waves," Master's thesis, Naval Postgraduate School, Monterey, CA, 1989.

2. Alpers, W. R., "Monte Carlo Simulations for Studying the Relationship Between Ocean Wave and Synthetic Aperture Radar Image Spectra," *J. Geophys. Res.*, Vol. 88, No. C3, pp. 1745–1759, 1983.

3. Alpers, W. R., and Bruening, C., "On the Relative Importance of Motion-Related Contributions to the SAR Imagery Mechanism of Ocean Surface Waves," *IEEE Trans. Geos. and Remote Sensing*, Vol. 66–24, No. 6, pp. 873–885, 1986.

4. Alpers, W. R., Ross, D. B., and Rufenach, C. L., "On the Detectibility of Ocean Surface Waves by Real and Synthetic Aperture Radars," J. Geophys. Res., Vol. 86, No. C7, pp. 6481–6498, 1981.

5. Alpers, W. R., and Rufenach, C. L., "The Effect of Orbital Motion on Synthetic Aperture Radar Imagery of Ocean Waves," *IEEE Trans. Antennas Propogat.*, Vol. AP-27, No. 5, pp. 685–690, 1979.

6. Alpers, W. R., and Rufenach, C. L., "On the Detectability of Ocean Surface Waves by Real and Synthetic Aperature Radar," *J. Geophys. Res.*, Vol. 86, pp. 6481–6498, 20 July 1981.

7. Barrick, D. E., "Rough Surface Scattering Based on Specular Point Theory," *IEEE Trans. Antennas Propagation*, Vol. AP-16, pp. 449–454, 1968.

8. Barrick, D. E., "First Order Theory and Analysis of MF/HF/VHF Scatter from the Sea," *IEEE Trans. Antennas Propagation*, Vol. AP-20, pp. 2–10, 1972.

9. Bass, F. G., Fuks, I. M., Kalmykov, A. E., Ostromky, I. E., and Rosenberg, A. D., "Very High Frequency Radiowave Scattering by a Distributed Sea Surface", *IEEE Trans. Antennas Propagation*, Vol. AP-16, pp. 554–568, 1968.

10. Beckman, P., and Spizzichino, A., *The Scattering of Electromagnetic Waves from Rough Surface*, Macmillan Company, 1963.

11. Brown, W. E., Jr., Elachi, C., and Thomson, T. W., "Radar Imagery of Ocean Surface Patterns," *J. Geophys. Res.*, Vol. 81, No. 15, pp. 2651–2667, 1976.

12. Daley, J. C., "Wind Dependence on Radar Sea Return," *J. Geophys. Res.*, Vol. 78, pp. 7823–7833, 1973.

13. Dobson, R. S., "Some Application of a Digital Computer to Hydraulic Engineering Problems," Stanford University Technical Report 80, 1967.

14. Elachi, C., and Brown, Jr., W. E., "Models of Radar Imaging of the Ocean Surface Waves," *IEEE Trans. Ocean Eng.*, Vol. OE-2, No. 1, pp. 84–95, 1977.

15. Floyd, R. P., "Coordinate Conversion for Hydrographic Surveying," NOAA Technical Report NOS 114, *Charting and Geodetic Services Series* CGS 7, 1985.

16. Goda, Y., *Random Seas and Design of Maritime Structures*, Univ. of Tokyo Press, pp. 41–68, 1985.

17. Goldstein, R. M., private communication, JPL, Pasadena, 1989.

18. Goldstein, R. M., Barnett, T. P., and Zebker, H. A., "Remote Sensing of Ocean Currents," *Science*, Vol. 246, p. 1282, 1989.

19. Goldstein, R. M., and Zebker, H. A., "Interferometric Radar Measurement of Ocean Surface Currents," *Nature*, Vol. 328, No. 6132, pp. 707–709, 1987.

20. Goldstein, R. M., Zebker, H. A., and Werner, C. L., "Satellite Radar Interferometry: Two Dimensional Phase Unwrapping," *Radio Science*, Vol. 23, No. 4, pp. 713–720, 1988.

21. Guza, R. T., "Surface Gravity Wave Measurements," Jet Propulsion Laboratory Publication, *TOWARD 84/86*, Vol. II, pp. I1–I5, 1986.

22. Hagfors, T., "Backscattering from an Undulating Surface with Applications to Radar Returns from the Moon," *Geophys. Res.*, Vol. 69, No. 10, pp. 3779–3786, 1964.

23. Harger, R. O., *Synthetic Aperature Radar Systems; Theory and Design*, Academic Press, New York, 1970.

24. Harger, R. O., "The SAR Image of Short Gravity Wane on a Long Gravity Wave," in *Wave Dynamics and Radio Probing of the Ocean Surface*, D. M. Phillips and K. Hasselmann, eds., Plenum, New York, 1986.

25. Hasselmann, K., "Feynman Diagrams and Interaction Rules of Wave Scattering Processes," *Rev. Geophys.*, Vol. 4, No. 1, pp. 1–32, 1966.

26. Hasselmann, K., Raney, R. K., Plant, H. J., Alpers, W., Schuchman, R. A., Lyzenga, D. R., Rufenach, C. L., and Tucker, M. J., "Theory of Synthetic Aperture Radar Ocean Imaging: A MARSEN View," *J. Geophys. Res.*, Vol. 90, No. C3, pp. 4659–4866, 1985.

27. Hayes, J., "Ocean Current — Wave Interaction," *J. Geophys. Res.*, Vol. 85, pp. 5025–5031, September 20, 1980.

28. Hayes, J., and Shuchman, R., "SEASAT SAR Ocean Surface Current Refraction and Shallow Water Wave Refraction," in *Oceanography from Space*, J. Gower, ed., Plenum Press, pp. 469–476, 1981.

29. Held, D. N., Brown, W. E., Freeman, A., Klein, J. D., Zebker, H., Sato, T., Miller, T., Nguyen, Q., and Lau, Y., "The NASA/JPL Multifrequency, Multipolarization Airborne SAR System," *Proc. IGARSS '89 Symp.*, Edinburgh, Scotland, September 13–16, 1988.

30. Hovanessian, S. A., *Introduction to Synthetic Array and Imaging Radars*, Artech House, Los Angeles, 1979.

31. Hovanessian, S. A., *Introduction to Synthetic Aperature Radar*, Artech House, Inc., pp. 5–36, 1980.

32. Jain, A., "Focusing Effects on Synthetic Aperture Radar Imaging of Ocean Waves," *Applied Phys.*, Vol. 15, pp. 323–333, 1978.

33. Jain, A., and Shemdin, O. H., "L Band SAR Ocean Wave Observations During Marsen," *J. Geophys. Res.*, Vol. 88, No. C14, pp. 9792–9808, 1983.

34. Jordan, A. K., and Lang, R. H., "Electromagnetic Scattering Patterns from Sinusoidal Surfaces," *Radio Science*, Vol. 14, No. 6, pp. 1077–1088, 1979.

35. Kalmykov, A. L., and Pustovoytenko, V. V., "On Polarization Features of Radio Signals Scattered from the Sea Surface at Small Grazing Angles," *J. Geophys. Res.*, Vol. 81, No. 12, 1975.

36. Kasilingam, D. P., and Shemdin, O. H., "Theory for Synthetic Aperture Radar Imaging of the Ocean Surface: With Application of the Tower Ocean Wave and Radar Dependence Experiment on Focus, Resolution, and Wave Height Spectra," *J. Geophys. Res.*, Vol. 93, No. C11, pp. 13837–13848, 1988.

37. Kerr, D. E., *Propagation of Short Radio Waves*, McGraw-Hill, Inc., New York, 1951.

38. Khalid, M. A., "Comparison of Measured and Transformed Directional Wave Spectra Using Linear Refraction Model," Master's thesis, Naval Postgraduate School, Monterey, CA, 1989.

39. Kirshen, K. "Correlation of Radar Backscatter Cross Section with Ocean Wave Height and Wind Velocity," *J. Geophys. Res.*, Vol. 76, pp. 6528–6539, 1971.

40. Klein, J. D., and Freeman, A., "Design Considerations for an Advanced Multi-Polarization SAR," *Proc. IGARSS '88 Symp.*, Edinburgh, Scotland, September 13–16, 1988.

41. Longuet-Higgins, M. S., Cartwright, D. E., and Smith, N. D., "Observations of the Directional Spectrum of Sea Waves Using the Motions of a Floating Buoy," *Ocean Wave Spectra*, Prentice-Hall, Englewood Cliffs, NJ, pp. 111–136, 1963.

42. Lyzenga, D. R., "Numerical Simulation of Synthetic Aperture Radar Image Spectra for Ocean Waves," *IEEE Trans. Geoscience Rem. Sens.*, Vol. GE-24, No. 6, pp. 863–872, 1986.

43. Lyzenga, D. R., and Shuchman, R. A., "Analysis of Scatterer Motion Effects in Marsen X Band SAR Imagery," *J. Geophys. Res.*, Vol. 88, No. C14, pp. 9769–9775, 1983.

44. Monaldo, F. M., and Lyzenga, D. R., "On the Estimation of Wave Slope- and Height-Variance Spectra from SAR Imagery," *IEEE Trans. Geoscience Rem. Sens.*, Vol. GE-24, No. 4, pp. 543–551, 1986.

45. Marom, M., Goldstein, R. M., Thornton, E. B., and Shemer, L., "Interferometric Synthetic Aperture Radar Imaging of Nearshore Wavefield in Monterey Bay," *Proc. IGARSS '90 Symp.*, Maryland, p. 2037, May 20–24, 1990.

46. Marom, M., Goldstein, R. M., Thornton, E. B., and Shemer, L., "Remote Sensing of Ocean Wave Spectra by Interferometric Synthetic Aperture Radar," in press *Nature*, 1990.

47. Plant, W. J., and Keller, W. C., "The Two Scale Radar Wave Probe and SAR Imagery of the Ocean," *J. Geophys. Res.*, Vol. 88, pp. 9776–9784, 1983.

48. Raney, K. R., "Synthetic Aperture Radar Imaging and Moving Targets," *IEEE Trans. Aeros. and Elec. Sys.*, Vol. AES-7, No. 3, pp. 449–505, 1971.

49. Raney, K. R., "SAR Response to Partially Coherent Phenomena," *IEEE Trans. Antennas Propagation*, Vol. AP-28, No. 6, pp. 777–787, 1980.

50. Raney, K. R., and Lowry, R. T., "Oceanic Wave Imagery and Wave Spectra Distortions by Synthetic Aperture Radar Imagery," *12th Int. Symp. Remote Sensing of Environment*, Manila, Phillipines, pp. 683–702, April 20–29, 1978.

51. Rice, S. O., "Reflection of Electromagnetic Waves from Slightly Rough Surfaces," *Commun. Pure Applied Math.*, Vol. 4, pp. 35–378, 1951.

52. Robinson, I. S., *Satellite Oceanography*, Halstead Press, Ellis Horwood, Chichester, 1985.

53. Seymour, R. J., and Higgins, A. L., "A Slope Array for Estimating Wave Direction," Nearshore sediment transport study workshop on instrumentation for nearshore processes, *Sea Grant*, Pub. No. 62, pp. 133–142.

54. Shemdin, O. H., "Tower Ocean Wave and Radar Dependence Equipment: An Overview," *JGR*, Vol. 23, C11, pp. 13829–13836, November 1988.

55. Shmelev, A. B., "Wave Scattering by Statistically Uneven Surface," *Usp. Fiz. Nauk*, No. 106, pp. 459–480, 1972.

56. Shuchman, R. A., and Kasischke, E. S., "Refraction of Coastal Ocean Waves," in *Spaceborne Synthetic Aperture Radar for Oceanography*, The Johns Hopkins University Press, Baltimore, pp. 128–134, 1981.

57. Skolnik, M. L., *Introduction to Radar Systems*, 2nd ed., McGraw-Hill Book Company, Inc., 1980.

58. Stewart, H. S., *Methods of Satellite Oceanography*, University of California Press, Berkeley and Los Angeles, 1985.

59. Stewart, R. H., and Jay, J. W., "HF Radio Measurements of Surface Currents," *Deep-Sea Research*, Vol. 21 (12), pp. 1039–1149, 1974.

60. Swift, C. F., and Wilson, L. R., "Synthetic Aperture Radar Imaging of Moving Ocean Waves," *IEEE Trans. Antennas Propagation*, AP-27, pp. 725–729, 1979.

61. Terada, K., and Hanzawa, M., "Climate of the North Pacific Ocean," in *Climate of the Oceans*, H. Van Laon, ed., Elsevier Science Publishers, pp. 431–438, 1984.

62. Thompson, D. R., "Calculation of Microwave Doppler Spectra from the Ocean Surface with a Time-Dependent Composite Model," *Radar Scattering from Modulated Wind Waves*, Kluwer Academic, pp. 27–40, 1989.

63. Thornton, E. G., "Maximum Wave Forces on Proposed Monterey Bay Regional Sewage Outfall Due to 50 Years Storm Waves," prepared for *Engineering Science, Inc.*, 1978.

64. Thornton, E. G., "Wave Design Criteria and Related Environmental Impacts," unpublished report for the Monterey Bay Aquarium, 1980.

65. Tidal Current Tables 1978: Pacific Coast of North and South America, U.S. Department of Commerce, pp. 13, 203, and 204, 1977.

66. Tidal Current Tables 1978: West Coast of North America and South America, U.S. Department of Commerce, pp. 74 and 164, 1977.

67. Tucker, M. J., *The Effect ofa Moving Sea Surface on SAR Imagery in Satellite Microwave Remote Sensing*, T. D. Alan, ed., Ellis Horwood, Chechester, England, pp. 146–154, 1983.

68. Tucker, M. J., "The Imaging of Waves by Satelliteborne Synthetic Aperture Radar: The Effects of Sea-Surface Motion," *Int. J. Rem. Sens.*, Vol. 6, No. 7, pp. 1059–1074, 1985a.

69. Tucker, M. J., "The Decorrelation Time of Microwave Radar Echoes from the Sea Surface," *Int. Remote Sensing*, Vol. 6, pp. 1075–1089, 1985b.

70. Ulaby, F. T., Moore, R. K., and Fung, A. K., *Microwave Remote Sensing*, Vol. II, Addison Wesley Publishing Company, pp. 612–617, 1982.

71. Uotila, U. A., "Notes on Adjustment Computations," Part I, Department of Geodetic Science & Surveying, The Ohio State University, 1986.

72. Valenzuela, G. R., "Scattering of Electromagnetic Waves from the Ocean," *Surveillance of Environmental Pollution and Resources by Electromagnetic Waves*, pp. 199–226, 1978.

73. Vachon, P. W., "Synthetic Aperture Radar Imaging of the Ocean Surface: Theoretical Considerations, and Experiments with Simulated and Actual SAR Imagery," PhD thesis, The University of British Columbia, 1987.

74. Vachon, P. W., Olser R. B., Livingstone, C. E., and Freeman, G., "Airborne SAR Imagery of Ocean Surface Waves Obtained During LEWEX: Some Initial Results, *IEEE Trans. Geoscience and Remote Sensing*, Vol. 26, No. 5, 1988.

75. Valenzuela, G. R., "An Asymptotic Formulation for SAR Image of the Dynamical Ocean Surface," *Radar Science*, Vol. 15, pp. 105-114, 1980.

76. Valenzuela, G. R., "SAR Imaging of Ocean Waves in the Presence of Variable Currents (1988)," *Radar Scattering from Modulated Wind Waves*, G. J. Komen, W. A. Ooast, eds., Kluwer Academic, pp. 141–153, 1989.

77. Valenzuela, G. R., and J. W. Wright, "The Growth of Waves by Modulated Wind Stress," *J. Geophys. Res.*, Vol. 81, No. 33, pp. 5795–5796, 1976.

78. Wright, J. H., "Backscattering from Capillary Waves with Application to Sea Clutter," *IEEE Trans. Antennas and Propagation*, AP-14, No. 3, pp. 749–754, 1966.

79. Yaplee, B. S., Shapiro, A., Hammond, D. L., Au, B. D., and Uliana, E. A., "Nanosecond Rader Observations of the Ocean Surface from a Stable Platform," *IEEE Trans. Geoscience Electronics*, Vol. GE-9, pp. 171–174, 1971.

INITIAL DISTRIBUTION LIST

1.	Defense Technical Information Center Cameron Station Alexandria, VA 22304-6145	2
2.	Library, Code 0142 Naval Postgraduate School Monterey, CA 93943-5002	2
3.	Chairman (Code OC/CO) Department of Oceanography Naval Postgraduate School Monterey, CA 93943	1
4.	Professor Edward B. Thornton (Code OC/TM) Department of Oceanography Naval Postgraduate School Monterey, CA 93943	2
5.	Professor Pecheng Chu (Code OC/CU) Department of Oceanography Naval Postgraduate School Monterey, CA 93943	1
6.	Professor Jeffrey A. Nystuen (Code OC/NY) Department of Oceanography Naval Postgraduate School Monterey, CA 93943	1
7.	Professor Kenneth L. Davidson (Code MR/DS) Department of Meteorology Naval Postgraduate School Monterey, CA 93943	1
8.	Professor Robert Haney (Code MR/HY) Department of Meteorology Naval Postgraduate School Monterey, CA 93943	1

9. Professor Gilbert T. Howard (Code 012) 1
Director of Research Administration
Naval Postgradate School
Monterey, CA 93943-5000

10. Professor Hung-Mou Lee (Code EC/LH) 1
Department of Electrical and Computer Engineering
Naval Postgraduate School
Monterey, CA 93943-5002

11. Professor Roberto Cristi (Code EC/CX) 1
Department of Electrical and Computer Engineering
Naval Postgraduate School
Monterey, CA 93943-5002

12. Dr. Gaspar Valenzuela 1
Naval Research Laboratory
Space Sensing Branch
Code 8312.4
4555 Overlook Avenue SW
Washington DC 20375-5000

13. Dr. Richard Goldstein 1
Jet Propulsion Laboratory
Code 300-227
4800 Oak Grove
Pasadena, CA 91109

14. Dr. David Castel 1
Scripps Institute of Oceanography
Center for Coastal Studies
La Jolla, CA 92903

15. Dr. Frank Herr 1
Office of Naval Research
800 N. Quincy Street
Arlington, VA 22217

16. Dr. Yuhsyen Shen 1
Jet Propulsion Laboratory
Code 300-241
4800 Oak Grove
Pasadena, CA 91109

17. Dr. Dayalan Kasilingam 1
Ocean Research and Engineering
255 S. Marengo Avenue
Pasadena, CA 91101

18. Commanding Officer 1
Fleet Numerical Oceanography Center
Monterey, CA 93943

19. Commanding Officer 1
Naval Environmental Prediction Research Facility
Monterey, CA 93943

20. Naval Ocean Research and Development Activity 1
NSTL Station
Bay St. Louis, MS 39522

21. Dr. David Sheres 1
University of Southern Mississippi
Center for Marine Science
John C. Stennis Space Center
Stennis Space Center, MS 39529

22. Commodore Arie Rona 1
C/O Naval Attaché
Embassy of Israel
3514 International Drive, NW
Washington DC 20008

23. Rear Admiral Micha Ram 1
C/O Naval Attaché
Embassy of Israel
3514 International Drive, NW
Washington DC 20008

24. Mr. Floyd York 1
Department of Oceanography
Naval Postgraduate School
Monterey, CA 93943

25. CDR Moshe Marom 8
C/O Defense and Armed Forces Attaché
Embassy of Israel
3514 International Drive, NW
Washington DC 20008